THEORY AND SIMULATIONS OF INTERACTING QUANTUM SYSTEMS

by

A. Barış Özgüler

A dissertation submitted in partial fulfillment of the requirements for the degree of

Doctor of Philosophy
(Physics)

at the

University of Wisconsin - Madison 2020

Defended on 17 June, 2020

Dissertation approved by the following members of the Final Oral Committee:

Maxim Vavilov \cdot Professor of Physics

Robert McDermott · Professor of Physics

Alex Levchenko · Professor of Physics

Jennifer Choy · Assistant Professor of Engineering Physics

Shimon Kolkowitz · Assistant Professor of Physics

© Copyright A. Barış Özgüler2020

Some rights reserved under the Creative Commons BY-NC-SA license. For more information, please refer to http://creativecommons.org/licenses/.

Abstract

In this thesis, we cover several topics from interacting quantum systems in the setting of quantum information algorithms and devices. The thesis is divided into two parts. In the first part, we study interacting spin-1/2 systems in the presence of uniform or disordered field. In the second part, we study novel multiterminal Josephson junctions.

We first analyze how a disordered spin system responds to a local drive. The response behavior of the system depends on the disorder strength. We show that one can obtain the phase of the system using the statistical measures of the response. We perform fidelity susceptibility and experimentally accessible spin variance calculations to identify whether the system is in the many-body localized or ergodic regime. We show that the results of these two approaches are correlated to each other and both can be used to find the phase of the system.

We further propose a steering method for the random spin systems to speed up the quantum adiabatic algorithm (QAA). We utilize counterdiabatic driving techniques to form 1-spin and cluster steering terms. We compare the efficiency of our steered QAA to the efficiencies of conventional QAA and classical optimization. We obtain a large parameter range in which steering provides speed-up.

Next, we study fluxonium qubit systems. Their strong anharmonicity, long coherence time and strong coupling ability makes them a good fit for spin-1/2 system simulations. We study quantum phase diagram of fluxonium qubit chains. We identify the phase transition boundary using the fidelity susceptibility techniques. We discuss some Ising spin chain simulations that can be performed using the fluxonium qubit chains.

Finally, we investigate multiterminal Josephson junctions. These devices work in high dimensional phase spaces due to phase contributions from extra terminals. Tuning the parameters of junctions with special geometries by gate voltage and magnetic field leads to multiterminal Josephson effect. The transition characteristics is measured by the shape and area of the multidimensional critical current contour. We explore the mechanisms behind this transition by using the scattering theory and microscopic computation of the wave

functions.

Acknowledgements

Everything that has a beginning has *probably* an end. My journey after the Mad City will continue with increased level of madness. One can consider the social arena as a strongly interacting system. I would like to thank everyone with whom I have interacted and benefited from. I am now very different in a positive manner, both academically and personally. I have learned a lot about myself during grad school. Some part of this thesis have been written under the extraordinary circumstances of COVID-19. These are challenging times with full of uncertainty but the process of finding myself has gained an acceleration.

First and foremost, I would like to thank my adviser Prof. Maxim Vavilov for his support and creating many opportunities for me to improve myself. Even though I only studied half of my grad school years under his supervision, the discussions with him have effectively helped me find my own way and the questions I have worked on, not all of them are addressed in this thesis, will continue shaping my future. He will stay as a valuable mentor for me.

I would also like to thank Prof. Bob Joynt for our discussions on how to steer random systems and for not so random other meaningful interactions. One very important scientific method trick I learned from him is the easy to say but difficult to do what I would summarize as "divide into simple steps and conquer". strategy¹ I will bring him more Turkish delights, especially for the Halloween.

My understanding of fluxonium qubit systems and multiterminal Josephson junctions have been built up thanks to many fruitful discussion with Prof. Vlad Manucharyan's group. I thank Hanho and Natalia for explaining the details of their multiterminal experimental setup and suggesting ways to improve my junction simulations.

I met with Dr. Jianxin Zhu at the CNLS 2019 conference in May, 2019. I would like to thank for his invitation to Los Alamos National Lab. (LANL) in Fall 2019 to collaborate on topological multiterminal junctions. It was great to explore new opportunities at LANL.

¹I should divide this sentence :)

I enjoyed the interactions I had during and after the Herb Seminars here at the physics department. Some of the Herb presenters with whom I benefited from our discussions include Mark Dykman, Peter Love, Aashish Clerk, Maxim Khodas, Ivar Martin, John King Gamble, Vlad Pribiag, Caglar Girit, written not in a particular order.

I sincerely appreciate the help provided by my thesis committee members including Profs. Robert McDermott, Alex Levchenko, Jennifer Choy, Shimon Kolkowitz and Maxim. The help of the physics staff including Renee, Michelle Holland, Jim Reardon have been crucial to create a nice atmosphere at the department.

I thank my friends for being with me and sharing memories during this journey. Thanks to the Garcia Family, Jenna, Mitch, Kostya, Ivan, Yinqi, Jonah, David, Vijesh and many more... It was fun to play tennis with David, Mike, Vijesh... Thanks to Jenna, David, Jonah and others for giving feedback about my piano improvisations. Also, many thanks to Kostya for his help during the times I was trying to find his nearest neighbor (Maxim):-) Moreover, the MFIS and BRIDGE friends have made my Madison journey more fun.

Last but not least, I would like to express my gratitude to my family. They make me feel like I have been with them even though they live thousands of miles away.

 $I\ dedicate\ this\ thesis\ to\ Munise,\ my\ |ket\rangle.$

Contents

	Abs	tract	i
	Ack	nowledgements	iii
C	onter	nts	vi
Li	st of	Figures	ix
Li	st of	Tables	xix
1	Intr	roduction	1
	1.1	Introduction to Quantum Computing	1
	1.2	Interacting quantum systems	3
		Spin systems	4
		Superconducting qubits	11
		Multiterminal Josephson junctions	13
	1.3	Computational workflow	16
	1.4	Outline of the thesis	18
	1.5	Publication List	20
Ι	Qua	antum Spin Models	22
2	Res	ponse of a quantum disordered spin system to a local periodic drive	23
	2.1	Introduction	23

	2.2	Fidelity susceptibility at weak drive	26
	2.3	Time evolution of the total spin	29
	2.4	Discussion and Conclusions	33
3	Pha	se Transitions and Edge States in Fluxonium Qubit Systems	38
	3.1	Introduction	38
	3.2	Mapping fluxonium chain onto transverse Ising chain in a longitudinal field	39
	3.3	Phase diagram	42
	3.4	Edge states	45
	3.5	Propagating Excitations	46
	3.6	Conclusions	48
4	Stee	ering random spin systems to speed up the quantum adiabatic algo-	
	rith	m	49
	4.1	Introduction	49
	4.2	Method	51
	4.3	Results	53
		Small Systems	54
		Comparison to Other Methods	54
		Distribution over Low-lying States	58
		Regime of Superiority of Steered QAA over Other Methods	59
		Cluster Steering	60
	4.4	Conclusion	60
II	Mu	ltiterminal Josephson Junctions	63
5	Stu	dies of multiterminal junctions via scattering theory	64
	5.1	3-terminal Josephson junctions with rectangular scattering region	64
		Model	68
		Derivation of Andreev energy levels and supercurrent	71

			viii
		Fraunhofer oscillations in multiterminal junctions	74
	5.2	Multiterminal Josephson junctions with more than three terminals \dots	85
	5.3	Conclusions	89
6	Stu	dies of finite multiterminal junctions	91
	6.1	Introduction	91
	6.2	Finite System Simulations	94
	6.3	Conclusions and Outlook	104
III Concluding Remarks and Bibliography 106		106	
7	Con	clusions and Outlook	107
Bi	Bibliography		111

List of Figures

1.1	Spin-1/2 chain system with quenched disorder $\{h_l\}$ in z-direction. $\{h_l\}$ is defined	
	by the uniform distribution within the interval $ h_l \leq W$. W is the disorder	
	strength and the interaction strength between the nearest neighbors are given	
	by the unitless parameters J_x , J_y , J_z . In Ising model, $J_x = J_y = 0$. In Heisenberg	
	model, $J_x = J_y = J_z = J$	Ę
1.2	The complete graph K_4 has four vertices and six edges. Similar diagrams can be	
	used to represent optimization problems. The weight J_{ij} is the cost of moving	
	from i to j . Each site has onsite cost h_i . Here, i and j are from 1 to number of	
	vertices.	7
1.3	$J=J_x=J_y$ hopping parameter, $J'=J_z$ interaction parameter. High en-	
	ergy barriers make the particle localized. When the disorder is weak, it is more	
	probable for a particle to discover different sites. In many-body localization, in-	
	teraction and hopping terms cannot hybridize the wave functions of the particles	
	in different sites	ć
1.4	The same initial product state is evolving under two Heisenberg Hamiltonians	
	${\cal H}$ with different disorder strengths. If the disorder strength is large, the evolved	
	state will be closer to its initial state even after long time. The measure of this	
	closeness can be given by the fidelity. In the thermalized phase, the memory is	
	lost quickly and the new state can be quite different than the initial state. $$	10

1.5	Fluxonium circuit consisting of capacitor, Josephson junction and superinductor.	
	The phase difference across the superinductor is ϕ and the external flux in the	
	loop formed by the Josephson junction and superinductor is Φ_{ext}	12
1.6	Andreev bound states formed by the electron-hole superpositions create Cooper	
	pairs in superconductors	14
1.7	Memory requirement for exact diagonalization of spin system Hamiltonians.	
	HTC stands for high-throughput computing. Column with the title "Without	
	HTC" represents the estimated amount of time that would be spent in personal	
	computers	17
2.1	(Color online) Heisenberg spin-1/2 chain system with quenched disorder $\{h_l\}$ in	
	the z-direction. $\{h_l\}$ is defined by the uniform distribution within the interval	
	$ h_l \leq W$. W is the disorder strength and the interaction strength between the	
	nearest neighbors is given by the unitless parameter $J=1.$ There is a local ac	
	drive with strength f on the spin labeled by $i=1$ in the x - y plane rotating with	
	drive frequency ω in the anticlockwise direction	25
2.2	(Color online) (a) Distribution of quantum displacement ε over $N=10^4$ real-	
	izations of the random magnetic field h_l for a system with $L=12$ spins. The	
	top panel shows the distribution of the displacement itself for $W/J=0.3$ (blue	
	long-dashed line), $W/J=3$ (green short-dashed line), and $W/J=30$ (red solid	
	line). Distributions for strong disorder have exponentially large tails. Rare	
	events appear for the strong disorder. (b) Logarithm of the distribution of ε for	
	the same three values of disorder as in (a). The dash-dotted line represents the	
	slope $\sim 10^{-1/2(\lg(\varepsilon))} = 1\sqrt{\epsilon}$. The drive amplitude $f = J/\sqrt{10}$ and $\omega = J$. lg	
	shows log_{10} throughout the text. We scaled the distribution curves for $W/J=3$	
	by factor two and for $W/J=30$ by factor six	28

2.3	(Color online) Average of the logarithm of quantum displacement, $\operatorname{lg}(\varepsilon)$, as a	
	function of disorder strength W for a spin system of size $L=8$ (circles), $L=10$	
	(squares) and $L=12$ (diamonds). The average is evaluated over $N=10^3$	
	disorder samples for $L=8,\ 10,\ 12.$ The drive amplitude $f=J/\sqrt{10}$ and $\omega=J.$	
	$\langle \langle \rangle \rangle$ shows the disorder average throughout the chapter	29
2.4	(Color online) (a) Average $\delta S_z^2(t)$ as a function of time for a spin system of size	
	L=14 (diamonds), $L=16$ (squares) and $L=18$ (circles). Curves for $W=1.25$	
	have filled and for $W=5$ have unfilled markers. The averages are performed	
	over 10^3 realizations of disorder for all system sizes and 10^3 product states for	
	L=14,150 product states for $L=16$ and 60 product states for $L=18$. The	
	overbar shows the product state average throughout the chapter. (b) Average	
	$\delta S_z^2(t)$ as a function of time for a spin system of size $L=14$ and $W=1.25$ or 5.	
	Results are compared for the initial product state with $S_z=\pm 1$ and 0 at $t=0$.	
	For all cases, 100 product states and 10^3 disorder averages are considered	31
2.5	(Color online) Average $\delta S_z^2(\tau)$ as a function of $\lg(W/J)$ for a spin system of	
	size $L=8$ (circles), $L=10$ (squares) and $L=12$ (diamonds). Time $=1$	
	period. $f = J/\sqrt{10}$ and $\omega = J$. The averages are performed over 10^4 disorder	
	realizations for $L=8,10^3$ disorder realizations for $L=10,L=12.$ All product	
	states are considered for all system sizes for product state averaging	32
2.6	(Color online) Distribution of $\lg(\overline{\delta S_z^2})$ over $N=10^3$ disorder realizations of the	
	random magnetic field h_l for a system with $L=12$ spins for $W/J=0.3$ (blue	
	long-dashed line) and $W/J=3$ (green short-dashed line), 30 (red solid line).	
	We scaled the distribution curve for $W/J=30$ by factor six. The averages are	
	performed over all product states of the system	34

2.7	(Color online) (a) Parameter plot of $\langle\langle\lg(\varepsilon)\rangle\rangle$ and $\langle\langle\lg(\overline{\delta S_z^2})\rangle\rangle$ for a spin system of	
	size $L=8$ (circles), $L=10$ (diamonds) and $L=12$ (squares). Data points from	
	Figs. 2.3 and 2.5 are used. Time = 1 period. The drive amplitude $f = J/\sqrt{10}$	
	and $\omega = J$. There is almost a linear dependence between the two quantities. (b,	
	c, d) Scatter plots of the data for the three of the results for $L=12$ from (a).	
	W=1 (red diamond), 3.16 (blue square) and 10 (green circle). Each scatter	
	plot includes 10^3 unfilled markers each of which corresponds to a single disorder	
	realization. Each average value in plots of (b, c, d) is in a big black square and	
	is shown by a filled marker of same type as the scattered data. \dots	35
3.1	(a) Fluxonium circuit. (b) Energy level diagram of a fluxonium qubit at the	
	sweet spot, $\phi_{ext} = \pi$. $V(\phi)$ is a double-well potential. Energy eigenstates are	
	also provided with numbers. They are in the order of increasing energy from	
	bottom to top. 0 corresponds to the ground state. $+$, $-$ signs represent the even	
	and odd functions, respectively.	39
3.2	Chain of two fluxonium atoms. Ising interaction is formed by the inductive	
	coupling between two superinductors	41
3.3	Open chain of 8 fluxonium atoms. Each fluxonium atom is numbered	42
3.4	Phase diagram for the antiferromagnetic open chain given in Fig. 3.3. Energy	
	gap between the first excited state and the ground state is plotted. Colorbar	
	unit is arbitrary. $J = 500 \text{MHz}.$	43
3.5	Phase diagram boundary estimated using fidelity susceptibility	44
3.6	(a) Fidelity susceptibility $\chi(h_x=0.56J)$ as a function of h_z for clean and disor-	
	dered fluxonium chain. 100 instances of disordered $\chi(h_x=0.56J)$ are plotted,	
	the distribution with more realizations are shown in (b). x-field consists of uni-	
	form and disordered terms. $J=500\mathrm{MHz}.$ (b) Distribution of h_z maximizing	
	$\chi(h_x=0.56J)$ for a sample of 10^4 disordered x-field	45

3.7	Magnetization as a function of site for a gapless point in Fig. 3.4. $h_x = h_z =$	
	0.56J. x-field has disorder. Results for clean (blue) and disordered (red) chains	
	are provided	46
3.8	Magnetization as a function of time for (a) clean, (b) disordered systems. i is	
	the qubit number. First qubit with $i=1$ is flipped initially. Both timing and	
	amplitudes could be used to quantify the differences between qubit responses.	
	Time unit is $1/J$	47
4.1	(Color online) Average ground-state probability as a function of the annealing	
	time t_a . The h_k are chosen uniformly from the interval $[-W, W]$, where $W = 1$.	
	All energy variables are measured in units of W , and time variables are measured	
	in units of \hbar/W throughout the chapter. (a) $L=1$. In the inset, the red	
	magnetic field vector rotates from x to z direction in the standard quantum	
	annealing process. The steering field applied in the $-y$ direction suppresses	
	transitions to the excited states. (b) $L=3,J=0.1.$ The green diamond curve	
	is the result of the application of Eq. (4.2), the exact Berry formula. The inset	
	shows the sketch of the open chain of 3 spins considered here	54
4.2	(Color online) (a) Average ground-state probability as a function of the annealing	
	time t_a . $L=8$ (square), $L=10$ (circle), $L=12$ (diamond) compared for J	
	= 0.1. (b) Average ground-state probability as a function of the interaction	
	parameter J for a short annealing time $t_a=1$. The red (upper), blue (middle)	
	and green (lower) dashed lines show the naive algorithm results for $L=8,10,12,$	
	respectively. (c) Average ground-state probability as a function of the interaction	
	parameter J for a longer annealing time $t_a = 100$.	56

4.3(Color online) Same markers are used in this figure as in Figs. 4.2(a) and (b) for the standard QAA and the steered QAA. For the naive algorithm, red (upper), blue (middle) and green (lower) "x" markers are used in the insets for L=8,10,12, respectively. In the insets, the naive algorithm is compared with the steered QAA. $t_a = 1$, J = 0.3. Several system sizes are shown. (a) The probability distribution over all final eigenstates $|n(t_a)\rangle$ as a function of the level index n, computed by comparing the results of the QAA to an exact calculation. $P_n = |\langle \psi(t_a) | n(t_a) \rangle|^2$. The effect of steering is to squeeze the width of the probability distribution by two orders of magnitude and in the direction of the ground state. (b) Cumulative probability distribution. $S_N = \sum_{n=1}^N \overline{P_n}$. With the steered algorithm, the chance to find one of the low-lying states is significantly 57 (Color online) Average infidelity as a function of 1/J and t_a . L=12. Plots for (a) the naive algorithm, (b) the standard QAA, and (c) the steered QAA. In the region covered by the white dashed lines, the steered QAA gives higher fidelity than the other two algorithms. (d) The colorbar shows the infidelity values. . . 58 (Color online) Average ground-state probability as a function of the interaction 4.5parameter J for the QAA without steering, with 1-spin steering, and with cluster steering. Cluster steering improves the results for $J \leq 0.2 \ t_a = 128, \ L = 12.$. . 61

5.1	System sketch of a tight-binding lattice which has scattering region of 21-by-	
	21 sites. Scattering sites are colored with blue and they are in between three	
	superconducting leads, which are semi-infinitely long and colored with red. The	
	superconducting leads are at the left, right and bottom of the scattering region.	
	Lattice constant $a=2nm$ throughout the chapter, $L,W=20a$ for this sketch.	
	L is the (horizontal) length and W is the (vertical) width of the junction. b is the	
	width of the bottom lead and $b=0$ limit is the two-terminal junction. b is varied	
	from 0 (two-terminal limit) to L . Magnetic field $\overrightarrow{B} = B\hat{z}$ with flux $\Phi = B.W.L$	
	is applied to the scattering region and it is perpendicular to the junction $(x-y)$	
	plane. Each terminal has a superconducting phase: $\theta_L = 0$, θ_R and θ_B . Currents	
	from each terminal entering the scattering region is represented by I_L , I_R and	
	I_B . L , R and B stand for left, right and bottom respectively. The lattices in	
	this thesis are produced via Kwant.	67
5.2	Energy as a function of momentum in the Brillouin zone. Tight-binding ap-	
	proximation and continuum results are compared. Tight-binding approximation	
	gives very close results comparing to the continuum model when energy levels	
	of the system are smaller than $t = \frac{\hbar^2}{2ma^2}$ (hopping parameter), where m is the	
	effective mass and a is the lattice constant. We choose $a=2nm,m=0.03m_e$	
	and therefore $t=318 \text{meV}$. We vary chemical potential, μ , around $E_F=120 \text{meV}$	
	and below t	71
5.3	ABS condition: $\Psi_{in} = \Psi_{out} = s_A(E) s_N(E) \Psi_{in} \dots \dots \dots \dots \dots$	73
5.4	(Color online) Critical currents at the right lead (I_R) and the bottom lead (I_B) as	
	a function of chemical potential (μ). Flux = 0. $L = W = b = 600nm$. Currents	
	have to be multiplied by $1/2$ due to electron-hole symmetry. The factor is not	
	considered in Eq. 5.14 while calculating energies. The factor has to be present	
	for the other unnormalized ground state energies and currents of this chapter	75
5.5	(Color online) (a) Area of CCC as a function of chemical potential (μ). Flux =	
	0. $L=W=b=600nm$. (b) Current scatter plots for $\mu=30,60,120$ meV	76

5.6	Critical current contour (CCC) scatter plots. Flux = 0, 0.5, 1 Φ_0 , where Φ_0 is	
	the flux quantum. $\mu=120 \mathrm{meV}, W=600 \mathrm{nm}, L=b=300 \mathrm{nm}.$	77
5.7	$\Delta E_{gs} = \max(E_{gs})$ - $\min(E_{gs})$ as a function of flux. Unit of flux is Φ_0	79
5.8	(a, b, c) CCC for flux 0, 1.2 Φ_0 and 1.5 Φ_0 , respectively. (d, e, f) GS energy	
	contours for the flux values in the same order. Phases corresponding to the	
	CCCs are given as differently colored clusters. Same colors and letters are used	
	for CCCs. (g, h, i) Hessian of the energy as a function of phases. Boundary	
	points satisfying Hessian close to zero are critical points which include CCC	
	points. CCC is the maximal envelope to the boundary Hessian points. $W=$	
	$L=b=60\mathrm{nm},\mu=20\mathrm{meV}.\ldots\ldots\ldots\ldots\ldots$	80
5.9	Normalized critical current as a function of flux for two-terminal junction ($b =$	
	0). $\mu = 120 meV \ W = 600 nm, \ L = 60 nm.$	82
5.10	Normalized CCC area as a function of flux for fixed narrow scattering region	
	$(W=600nm,L=60\mathrm{nm})$ and various width b of the bottom lead. $\mu=120meV.$	
	The arrow shows the color order of amplitude height	83
5.11	Normalized CCC area as a function of flux for fixed $L/b=5.\ W=600nm, L=$	
	60nm (red), 120nm (blue), 300nm (green). $\mu=120meV.$ The arrow shows the	
	color order of amplitude height.	84
5.12	System sketch of 4-terminal Josephson junction with rectangular scattering re-	
	gion. The parameters are similar to the ones in Fig. 5.1. Here, the terminal	
	widths have full widths. The top ("T") terminal has phase θ_T and the super-	
	current coming from it is I_T	86
5.13	The region with pale blue is the three-dimensional supercurrent points for the	
	leads with independent phases (T, R, B). Opposite terminals are paired up:	
	$I_T + I_B = 0$ and $I_L + I_R = 0$. The boundary of the region formed by the	
	intersection between the three-dimensional supercurrents and the plane $I_T + I_B =$	
	0 is the two-dimensional CCC	87

5.14	Scatter plots for the system in Fig. 5.12. μ unit is meV. $L=W=500 \mathrm{nm}$.	
	Supercurrent unit is arbitrary	87
5.15	(a) X junction with arm length L and width W . (b) Approximate 8-terminal	
	model for X junction.	88
5.16	Scatter plots for the system in Fig. 5.15(b). $W=2\mathrm{nm},\ L=18\mathrm{nm},\ \mathrm{lattice}$	
	constant $a=1$ nm. Chemical potential is uniform in the junction. μ unit is	
	meV. Supercurrent unit is arbitrary	89
6.1	ABS wave function localization in the scattering region. (a) Extended ABS	
	wave functions can be localized with equal probability in the arms and middle	
	region if the system geometry is finely tuned. The coupling between the opposite	
	junctions create rounded CCCs. (b) When the Fermi wavelength is small, the	
	arms are more dominant because the area of the arms are larger than the middle	
	region (because $L>W$). So, CCC becomes a rhombus due to lack of connection	
	of opposite junctions. The figure in (b) is given for a system where the middle	
	region localizations are neglected.	92
6.2	(a) Scattering region, (b) X finite system	93
6.3	(a) 2-terminal finite system. Long wide junction with width $W=500\mathrm{nm},L=$	
	40nm. L_{Lead} is chosen much longer than the coherence length. (b) Current I as	
	a function of phase ϕ (between 0 and 2π). (c) Critical current as a function of Δ .	
	Critical current is defined as the maximum positive or negative current. Super-	
	current units are arbitrary in this chapter (Coefficient $\frac{2e}{\hbar}$ should be multiplied	
	by the currents)	96
6.4	CCCs for $W=60\mathrm{nm}$. (a) $L=720\mathrm{nm}$ (b) 400nm, (c) 300nm. Flux is zero.	
	Chemical potential is the same over all junction. Top gate voltage is zero. μ	
	unit is meV throughout the chapter. Supercurrent unit is arbitrary throughout	
	the chapter	98

6.5	For $W = 60$ nm and $L = 300$ nm at zero flux, CCCs are rhombus and circle	
	for $\mu=0.4 \mathrm{meV}$ and $\mu=0.09 \mathrm{meV}$, respectively (see Fig. 6.4). (a) When flux is	
	varied, rhombus preserves its shape and current inversion symmetry, (b) whereas	
	the circle shape transforms into a shape with broken current inversion symmetry.	
	CCCs for zero flux are given in the left column for comparison.	99
6.6	CCCs for $L=720\mathrm{nm}$. (a) $W=140\mathrm{nm}$, (b) $W=220\mathrm{nm}$. Flux is zero. Chemical	
	potential is the same over all junction. Top gate voltage is zero.	100
6.7	Flux is varied for the rhombus CCCs of $W=220\mathrm{nm},L=720\mathrm{nm}.$ Rhombic	
	shape is preserved.	101
6.8	CCCs for $W=140\mathrm{nm}.\ L$ is varied. Top gate voltage is varied. (a) $W=140\mathrm{nm},$	
	$L=720 \mathrm{nm}$ for $\mu=0.09 \mathrm{meV}$. CCC shape is preserved for small μ (= small	
	number of channels). (b, c, d) Fix $W=140\mathrm{nm},$ and $\mu=3\mathrm{meV}.$ Vary $L.$ (b)	
	$L=840\mathrm{nm},$ (c) $L=720\mathrm{nm},$ (d) $L=600\mathrm{nm}.$ For larger $L,$ the arms of the	
	scattering region are more dominant. Therefore, CCCs are rhombus. As can	
	be seen in (d), the shape gets circular when the gate voltage is increased for	
	the right choice of L because the coupling between the opposite terminals gets	
	stronger due to extended ABS wave functions inside the scattering region	103

List of Tables

Chapter 1

Introduction

1.1 Introduction to Quantum Computing

Methods of computation have been discussed since ancient ages and have attracted attention of scholars from many fields [1, 2, 3]. The early examples of digital classical simulators are designed and built in the 19th and the first half of the 20th century. Charles Babbage designed the mechanical purpose-specific Difference Engine and general-purpose Analytical Engine [4]. After the invention of the vacuum tube, more practical and faster electronic computers have been invented. The scientific developments related to defense during WWII fired up the curiosity towards building computers that can solve numerical problems efficiently [5]. ENIAC became the first electronic universal classical computer [6]. The usage of transistors in integrated circuits made computers become denser and more powerful. This trend is summarized by Moore's Law as the fact that number of transistor counts per integrated circuit doubles up every two years [7]. Due to the increased ability of manipulation of atoms to build miniature devices, Feynman foresaw that "There is plenty of room at the bottom" [8]. Feynman would predict in two decades later that the room at the bottom could also be used for quantum computing, for which behavior of sub-atomic particles are exploited.

Quantum computing is relatively new in the history of computing. The first proposals

¹An engine duplicate is demonstrated at the Computer History Museum in Mountain View, CA.

about it started to appear in 1980s. Yuri Manin laid the mathematical foundation of quantum computing [9]. Shortly after, Richard Feynman proposed the idea of usage of quantum systems for simulating quantum physics in a famous speech of his [10]. Deutsch developed the idea of universal quantum computer which uses quantum gates in opposed to binary logic used in classical computers [11]. Quantum computers use the quantum analog of classical bits, called qubits. Qubits are two level systems that can be written as linear combinations of $|0\rangle$ and $|1\rangle$. Superposition and entanglement are the main two characteristics that makes quantum systems more powerful than their classical counterparts.

After these early developments in quantum computing, several quantum algorithms were discovered in a decade. Deutsch-Jozsa [12] and Simon's [13] algorithms are two of the first quantum algorithms that provide exponentially faster solutions than any available classical algorithms. Peter Shor achieved polynomial time factorization with the algorithm known with his name [14]. Lov Grover's quantum database search algorithm provided quadratic speed-up [15]. These achievements created excitement about the applications of quantum computing.

Quantum versions of already-existing classical heuristics and algorithms have also been discovered. A successful example is quantum annealing [16], which uses quantum tunneling instead of thermal jumps that are used in simulated annealing [17]. Quantum annealing is an approximate way to find global minimum and exploits dissipation and decoherence. It is shown to be more efficient than simulated annealing [18]. Applications of quantum computing was started to be commercialized before the start of 21st century.² Shortly after these developments, adiabatic quantum computing (AQC) was introduced [19, 20]. AQC is based on encoding an optimization problem in a physical system. The initial state is the ground state of an initial Hamiltonian. System evolves from the initial Hamiltonian to a final problem Hamiltonian. AQC is analog equivalence of the digital gate-based universal quantum computer. AQC with nonstoquastic Hamiltonians is equivalent to the gate-based universal quantum computing [21]. Due to its dissipative characteristics, quantum annealing

 $^{^2}$ A Canadian company established in 1999, D-Wave, commercialized the quantum annealing approach and became the first quantum computing company.

is a bridge between classical optimization and AQC in terms of its efficiency [22]. Quantum annealing has been explored as an approachable way towards the ultimate goal of building universal quantum computers.

There have been recent exciting developments in the gate-based, analog and topological³ quantum computing [23, 24, 25]. We are now in the era of Noisy Intermediate-Scale Quantum (NISQ) computers [26]. It is predicted that NISQ processors with 50-100 qubits can perform certain tasks faster than the fastest available classical processors. First foot-prints of quantum supremacy has been reported [27]. The ultimate goal is to build practical quantum computers with error corrections, which will need millions of qubits. The more reachable goal is to build midsize noisy quantum computers with 50-100 qubits and build hybrid algorithms which has classical and quantum counterparts such as QAOA and VQE [28, 29].

Qubits can be produced in various forms. Each system has its own advantages and disadvantages. The common property is the difficulty of building a quantum computer using any of the available qubits. Qubit quality has to be high in order to achieve a fully functional quantum computer.⁴ There is a steady increase in the power of quantum computers. This trend has been cited as the quantum version of the Moore's Law [30]. Number of qubits in D-Wave style analog quantum processors doubles up every two years, whereas doubles up every year in gate-based quantum processors.

1.2 Interacting quantum systems

Both closed and open interacting quantum systems are widely studied in condensed matter physics [31, 32] and they are useful tools in quantum computing [33]. Information can be encoded in the quantum systems. For example, cost function in optimization problems can be encoded as Ising Hamiltonian. Quantum systems are hard to tackle using classical computers. NISQ devices made from quantum hardware such as optical lattices [34], trapped

³Braiding is performed as the equivalence of gates.

⁴The measure of the qubit quality is given by the threshold theorem [1]

ions [35], Rydberg atoms [36], ultracold atoms [37], gmon system [38] and superconducting circuits [39] made simulating interacting quantum systems accessible.

This thesis covers theory and simulations of closed interacting quantum systems, namely disordered spin-1/2 systems and multiterminal Josephson junctions.⁵ For disordered spin-1/2 systems, Ising and Heisenberg models are considered. For multiterminal junctions, we simulate quantum transport using tight-binding models as approximations to continuum models. We will also discuss simulating transverse field Ising model by fluxonium qubit systems, a type of superconducting qubit hardware.

Spin systems

Hamiltonian for interacting spin-1/2 systems with nearest neighbor interaction and onsite random field can be written as:

$$H = \sum_{l=1}^{L} \left[J_x \, \sigma_x^{(l)} \sigma_x^{(l+1)} + J_y \, \sigma_y^{(l)} \sigma_y^{(l+1)} + J_z \, \sigma_z^{(l)} \sigma_z^{(l+1)} + h_l \sigma_z^{(l)} \right]. \tag{1.1}$$

Here, $\sigma_x^{(l)}$, $\sigma_y^{(l)}$ and $\sigma_z^{(l)}$ are Pauli matrices for spins at site l. We assume that chain satisfies the periodic boundary condition $\sigma^{(L+1)} = \sigma^{(1)}$, where $\sigma^{(l)}$ is the vector of Pauli matrices for spin at site l. The onsite fields h_l are independent random fields, uniformly distributed in the range [-W, W], where W is the disorder strength of the system. The isotropic case $J_x = J_y = J_z = J$ is the Heisenberg model and can be written using vector of Pauli matrices:

$$H_H = \sum_{l=1}^{L} \left[J \boldsymbol{\sigma}^{(l)} \boldsymbol{\sigma}^{(l+1)} + h_l \sigma_z^{(l)} \right]. \tag{1.2}$$

The random field Ising model (RFIM) Hamiltonian can be considered as the special form of Eq.(1.1) with $J_x = J_y = 0$:

$$H_{\rm I} = \sum_{l=1}^{L} \left[J \sigma_z^{(l)} \sigma_z^{(l+1)} + h_l \sigma_z^{(l)} \right]. \tag{1.3}$$

RFIM Hamiltonian $H_{\rm I}$ can be mapped onto its classical version. Addition of transverse field gives the quantum version of RFIM, which is the transverse field Ising model in a

⁵The latter also includes spin-1/2 particles such as electrons.

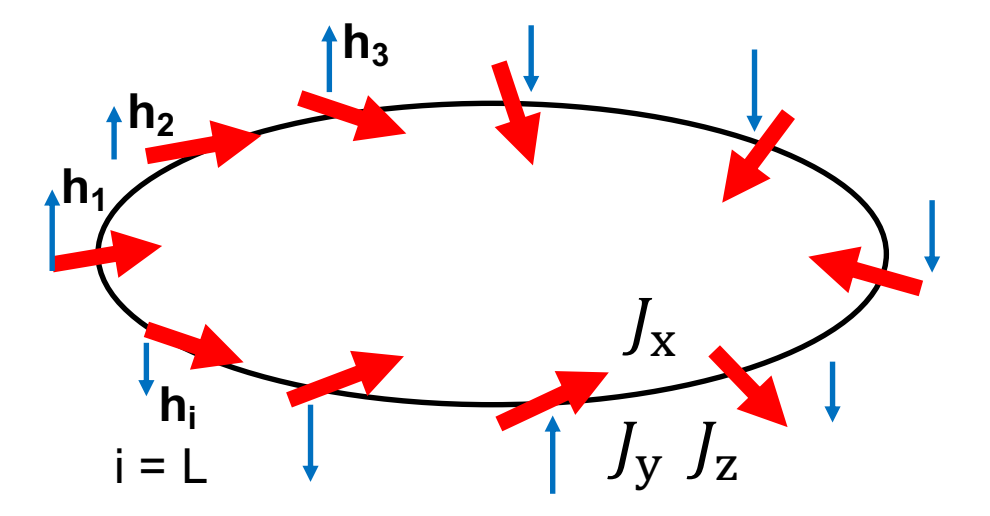


Figure 1.1: Spin-1/2 chain system with quenched disorder $\{h_l\}$ in z-direction. $\{h_l\}$ is defined by the uniform distribution within the interval $|h_l| \leq W$. W is the disorder strength and the interaction strength between the nearest neighbors are given by the unitless parameters J_x , J_y , J_z . In Ising model, $J_x = J_y = 0$. In Heisenberg model, $J_x = J_y = J_z = J$.

longitudinal field. Its Hamiltonian is another special form of the general interacting spin equation (Eq.(1.1)) with $J_y = J_z = 0$ and longitudinal field h_l^x at each site l:

$$H_T = J \sum_{l=1}^{L-1} \sigma_x^{(l)} \sigma_x^{(l+1)} + \sum_{l=1}^{L} h_l^x \sigma_x^{(l)} + \sum_{l=1}^{L} h_l^z \sigma_z^{(l)}.$$
 (1.4)

It is a common model for quantum phase transition studies [40]. We will show in Chapter 3 that fluxonium qubit systems can be mapped onto transverse field Ising model in a longitudinal field. Moreover, the standard QAA Hamiltonian is also written in terms of transverse field Ising model Hamiltonian. We will discuss speed-up mechanisms by adding steering terms in directions other than x-direction and also consider additional interaction terms.

Quantum adiabatic algorithm

Difficult optimization problems can be formulated as Ising Hamiltonian [41]. Optimization problems can be represented diagrammatically using vertices and edges as in Fig. 1.2. The

cost function of optimization problems can be defined as:

$$H_C = \sum_{ij} J_{ij} x^{(i)} x^{(j)} + \sum_{i} h_i x^{(i)}, \qquad (1.5)$$

where $x^{(i)}$ is a Boolean variable and $x^{(i)} \in \{0,1\}$, J_{ij} is the weight of the edges connecting site i to j, h_i is the onsite cost at the vertex i. The aim of the optimization problems is to minimize the cost functions to find the minimal cost and the corresponding optimal configuration of string of Boolean variables. Optimization problems can be mapped onto physical systems to be able to run the algorithms in physical simulators. One can switch from Boolean variables to spins using the transformation $\sigma_z^{(i)} = 1 - 2x^{(i)}$. Then $\sigma_z^{(i)} \in \{-1,1\}$. After this transformation, the cost function in Eq.(1.5) can be written as classical Ising Hamiltonian:

$$H = \sum_{ij} J_{ij} \,\sigma_z^{(i)} \sigma_z^{(j)} + \sum_i h_i \,\sigma_z^{(i)}, \tag{1.6}$$

where J_{ij} is the strength of the coupling between the spins at sites i and j and h_i is the onsite energy of site i. Ground state and ground state energy of Eq.(1.6) correspond the optimal configuration and minimal cost, respectively.

One of the leading candidates to solve difficult optimization problems is quantum adiabatic algorithm (QAA) [19, 20]. Optimization problems can be encoded as Hamiltonians of interacting systems. The ground state is the solution to the problem. AQC exploits the adiabatic theorem [42]. If the time evolution is slow and there is a gap between the ground state and rest of the Hamiltonian, the final state of the system gives the ground state (solution) of the final Hamiltonian. During the course of the computation, the ground state of an initial Hamiltonian is driven slowly to be able to find the ground state of a problem Hamiltonian.

In standard QAA approach, the ground state of the random field Ising Hamiltonian can be found starting from an initial state which is the ground state of an easy-to-prepare Hamiltonian. Such a Hamiltonian can be selected as the spin system under x magnetic field:

$$H_x = h_x \sum_{l=1}^{L} \sigma_x^{(l)}$$
 (1.7)

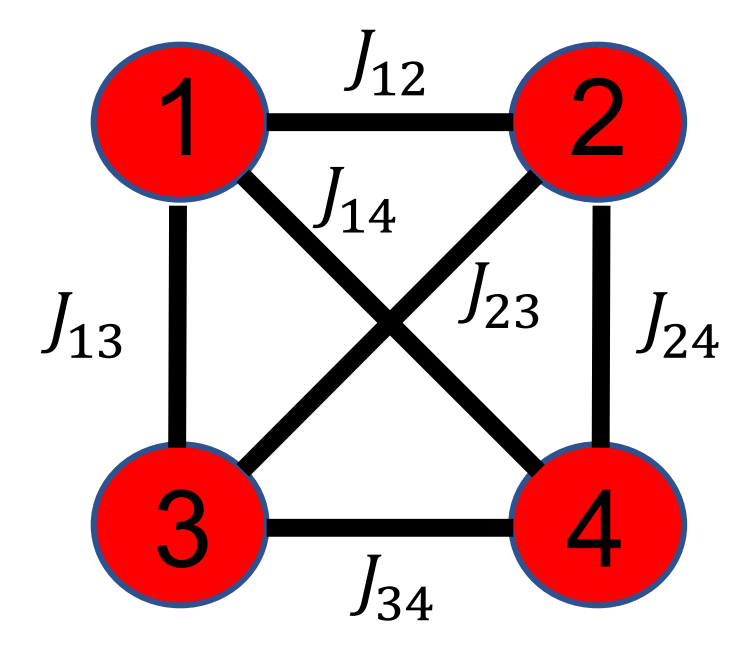


Figure 1.2: The complete graph K_4 has four vertices and six edges. Similar diagrams can be used to represent optimization problems. The weight J_{ij} is the cost of moving from i to j. Each site has onsite cost h_i . Here, i and j are from 1 to number of vertices.

The total Hamiltonian $f_I(t) H_I + f_x(t) H_x$ with time schedules $f_I(t)$ and $f_x(t)$ becomes transverse field Ising Hamiltonian. H_x and H_I does not commute and makes the optimization problem Hamiltonian quantum. H_x keeps the gap open and allows to search for different spin configurations. The ground state of the H_x is nondegenerate, which is another reason to start with H_x .

We search for algorithms that can provide more speed-up than QAA. An obstacle to a faster algorithm is the exponentially small gaps in the spectrum. The nature of the gaps can be understood via avoided level crossings in Landau-Zener problem. In addition to the avoided level crossings, the small gaps can also arise at the quantum phase transition points [43]. In this thesis, we show that the small gaps due to avoided crossings created by single-particles can be eliminated by adding a steering term to the standard QAA Hamiltonian.

Our inspiration comes from counterdiabatic driving, a shortcuts to adiabaticity [44] method. General time-dependent systems can be driven fast and without transitions if

a steering term is added [45], which will also be explained in Chapter 4. We propose the steered QAA to find the ground states of Ising spin systems with random field in a faster way. We explain how QAA can be improved by using local and cluster steering methods. Slowdown mechanisms were mitigated using extra terms added to the standard AQC Hamiltonian.

The steering term exploits directions other than the transverse field Ising Hamiltonian given by Eq.(1.4). It makes the total Hamiltonian a part of special class, called nonstoquastic Hamiltonians. Nonstoquastic Hamiltonians have positive or complex off diagonal elements in the computational basis. As we mentioned earlier, nonstoquastic Hamiltonians can provide the means for universal quantum computing [21]. There have been many recent studies about the effectiveness of nonstoquastic terms [46, 47, 48, 49, 50, 51, 52, 53]. With the advance of nonstoquastic simulators [54], AQC will gain a new look [55].

In the NISQ era, analog simulators are useful especially due to their less need for error correction. However, analog simulators are hard to control and gate-based quantum computers are expected to take analog computer's place completely in the future [26]. Currently, the number of qubits for error correction in gate-based computers are small, so analog quantum simulators will continue to be used and developed for near term applications.

Many-body localization

The spin model with $J_x = J_y$ and $J_z = 0$ given in Eq.(1.1) can be mapped onto noninteracting spinless fermions via Jordan-Wigner transformation [56]:

$$H_F = -\sum_{l} h_l c_l^{\dagger} c_l - t \sum_{kl} (c_l^{\dagger} c_k + c_k^{\dagger} c_l), \qquad (1.8)$$

where $t = -J_x/2$ is the hopping parameter, c_l and c_l^{\dagger} are the annihilation and creation operators at site l. Anderson showed that the wave function $\psi(x) \sim \exp(-x/\xi)$ can be localized in disordered systems [57, 58].⁶ Many-body localization (MBL) is the generalization of single-particle localization with the interaction turned on, i.e. $J_z \neq 0$. Random-field

 $^{^6\}xi$ is the localization length.

Heisenberg model given in Eq.(1.2) is the standard model for MBL in one-dimensional systems. Rigorous proof for the existence of MBL in one-dimensional quantum spin chains is given in Ref. [59].⁷

A sketch for the localization of spinless fermions is given in Fig. 1.3. Wave function of a particle is extended if the disorder barriers are low. The likelihood for a particle to discover different sites are higher than a localized particle which is stuck in a local energy well.

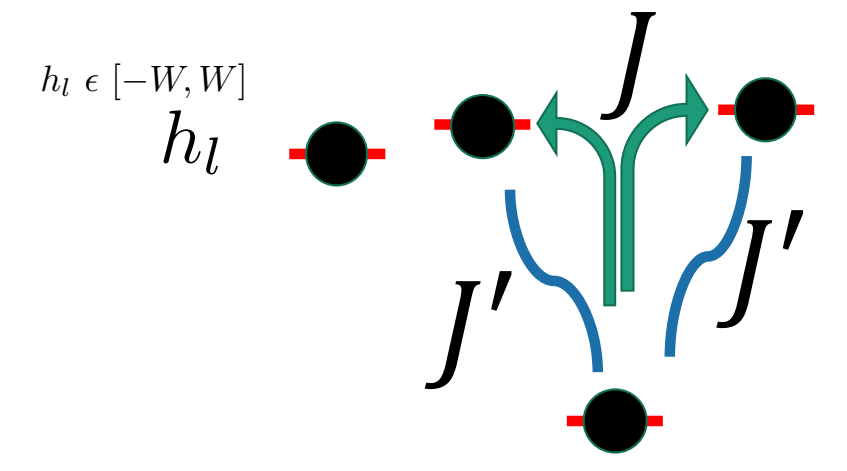


Figure 1.3: $J = J_x = J_y$ hopping parameter, $J' = J_z$ interaction parameter. High energy barriers make the particle localized. When the disorder is weak, it is more probable for a particle to discover different sites. In many-body localization, interaction and hopping terms cannot hybridize the wave functions of the particles in different sites.

The disorder strength defines the phase of the system: Ergodic or MBL. To distinguish between these two phases, one can start evolving two same initial states written as product states of spin up and down. When disorder is low, the overlap between the final state and the initial state will be small. However, larger disorder preserves the memory of the system. In that case, the overlap between the final state and the initial state will be higher. This process is visualized in Fig. 1.4.

It is important to understand localization properties of interacting systems for quantum computing purposes. A related example appears in QAA. Localization can cause the wave function to be stuck in a local minimum and prevent it from evolving into the ground state

⁷For larger dimensions, mathematical proof has not been available yet but computational results support its existence.

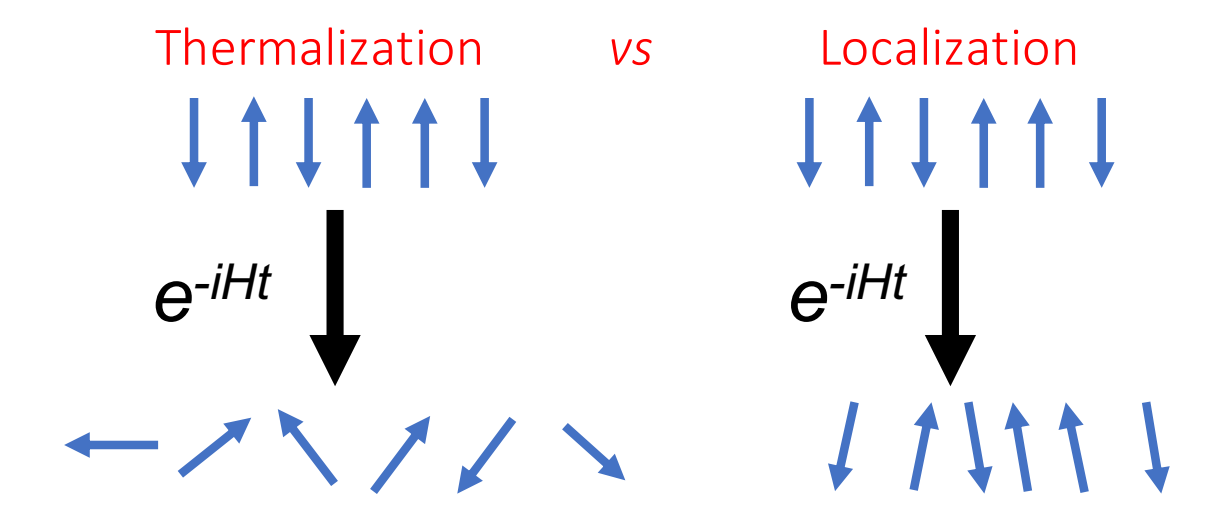


Figure 1.4: The same initial product state is evolving under two Heisenberg Hamiltonians H with different disorder strengths. If the disorder strength is large, the evolved state will be closer to its initial state even after long time. The measure of this closeness can be given by the fidelity. In the thermalized phase, the memory is lost quickly and the new state can be quite different than the initial state.

of the final Hamiltonian. Therefore, MBL is seen as a challenge against AQC [43]. On the other hand, MBL systems are valuable resources for information storage due to their high memory storage capacity [60, 61].

In Chapter 2, we explain how a disordered spin system with Heisenberg interaction responds to a local periodic drive. A weak local drive perturbs the systems in different amounts as a function of disorder strength. We consider a drive affecting one of the spins in Fig. 1.1. We calculate how much the final wave function is displaced with respect to the initial state wave function. The quantum displacement is proportional to fidelity susceptibility, a measure of how likely a wave function changes under a perturbation [62]. In MBL regime, the displacement is small and the distribution of it is narrow. As an another experimentally available approach, we calculate the spin accumulation as a function of time. The total spin in z-direction given by

$$S_z = \frac{1}{2} \sum_{l} \sigma_z^{(l)} \tag{1.9}$$

is conserved under the evolution of the static Hamiltonian Eq. (1.2). The local drive breaks

this conservation. We choose the initial state as the product state whose total spin in z-direction is zero. The spin accumulation will increase in different rates depending on the regime of the system. As shown in the sketch in Fig. 1.4, the total spin is close to its initial value when the system is in the MBL regime. We demonstrate that there is a positive linear correlation between diffusion coefficient and quantum displacement, and therefore spin accumulation measurements also give another way to distinguish between thermalized and MBL regimes.

Superconducting qubits

Superconducting qubit systems have been used for quantum simulations and are common tools for both gate-based and analog quantum computing [33, 39, 55]. Superconducting qubits are artifical atoms built using Josephson junctions and other electrical elements such as inductors and capacitors which shunt the superconducting electrodes. In the quantum harmonic oscillator formed by inductor and capacitor, energy levels are equally separated. Josephson junction creates anharmonicity and separates the ground state and first excited state from the rest of the spectrum. If the anharmonicity is high, then the ground and first excited states can be accurately used to build computational states $|0\rangle$ and $|1\rangle$. Another crucial factor that defines the quality of superconducting qubits is coherence time. The qubit keeps its quantumness during coherence time. Qubits with higher coherence times can be used longer in quantum computations.

As showed in Fig. 1.5, a fluxonium circuit has a capacitor, Josephson junction and a superinductor. The superinductor has a high inductance and is a series of more than 100 Josephson junctions. The high inductance creates large anharmonicity. It has been shown that the coherence time of fluxonium can be higher than 100 µs at its sweet spot [63]. Large anharmonicity and long coherence time make fluxonium a strong alternative to other available superconducting qubits [64]. Transmon has long coherence time but low anharmonicity. The Cooper pair box has high anharmonicity but short coherence time. Fluxonium has the desired sides of these two types of qubits.

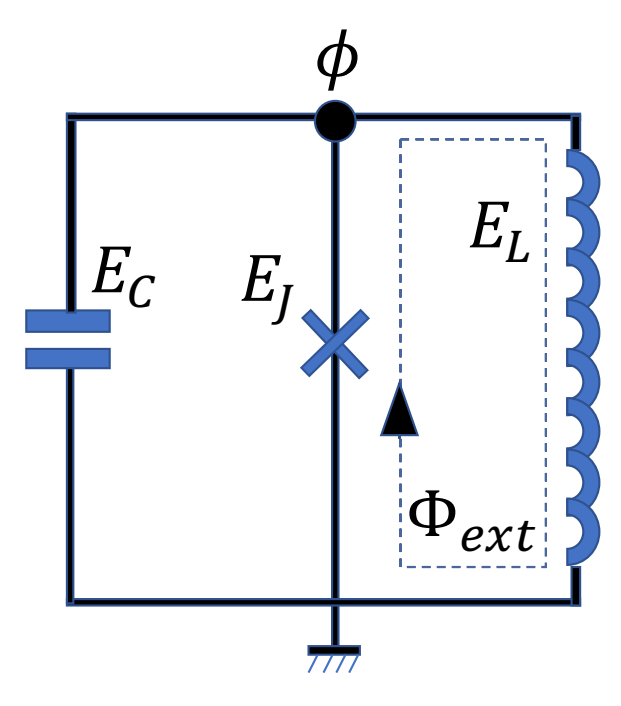


Figure 1.5: Fluxonium circuit consisting of capacitor, Josephson junction and superinductor. The phase difference across the superinductor is ϕ and the external flux in the loop formed by the Josephson junction and superinductor is Φ_{ext} .

In this thesis, we will discuss transverse field Ising model simulations that can be performed using fluxonium qubit systems. This type of simulation obeys analog quantum simulation, as summarized in the following. The quantum system to be simulated is mapped onto the fluxonium qubit systems. Initial state is prepared at t=0 and the system evolves under time. After a certain time $t=\tau$, the state of the system is measured. Fluxonium provides advantages in simulating transverse field Ising Hamiltonian because high anharmonicity keeps the computational states $|0\rangle$ and $|1\rangle$ distant from the rest of the spectrum. Moreover, inductive connection provides XX coupling. Even if there is detuning away from the sweet spot, the decrease in coherence time is not drastic and the qubit can still be used to simulate spin-1/2 systems accurately. It has been shown in Ref. [63] that the qubits with 5 µs coherence time can form a linear chain of 10 qubits.

Fluxonium can also be used in the search of Majorana fermions. As mentioned above for MBL, fidelity susceptibility is a useful tool to detect phase crossovers. We use fidelity susceptibility to study quantum phase transition of fluxonium qubit systems. Ground energy level of the Ising Hamiltonian given in Eq.(1.3) is degenerate and a transverse field increases the energy gap between the ground state and the first excited state. The energy gap vanishes in the topological regime. This property of the transverse field Ising model mimicks the Majorana nanowires [65]. Engineering Majorana nanowires using proximity effects are difficult to realize and so far there is no success of Majorana fermion observation even in simple systems based on s-wave superconductors [66]. Fluxonium qubit systems are more accessible and effective tools to discover Majorana physics in Ising-type Hamiltonians. It has been shown that even short Ising chains are useful to discover Majorana physics [67, 68, 65]. The already available fluxonium qubits can simulate such short Ising chains accurately thanks to its superior properties [63].

Multiterminal Josephson junctions

Multiterminal Josephson junctions are another solid state systems showing quantum behavior. As stated in the previous subsection, Josephson junctions are important ingredients of superconducting circuits. There are many other usages of Josephson junctions [69, 70, 71, 72]. In this thesis, we will focus on the novel phenomena observed in multiterminal Junctions [73, 74, 75, 76]. Here, we give an introduction to multiterminal Josephson junctions and Andreev reflection. In Chapter 5, we will discuss junctions with more than two terminals.

Andreev bound states (ABS) create supercurrents in Josephson junctions as shown in Fig. 1.6. Particles in normal regions which are squeezed between superconducting terminals are confined within superconducting potential barriers. Electron (hole) incoming from normal region to superconducting boundary with energy smaller than the superconducting pair potential bounces back as hole (electron) to the normal region with the same energy and approximately same momentum [77]. This process keeps happening after the particle reaches to the another NS boundary.⁸ Cooper pair flow in the superconducting region

⁸S and N stand for superconducting and normal regions, respectively

creates supercurrent.

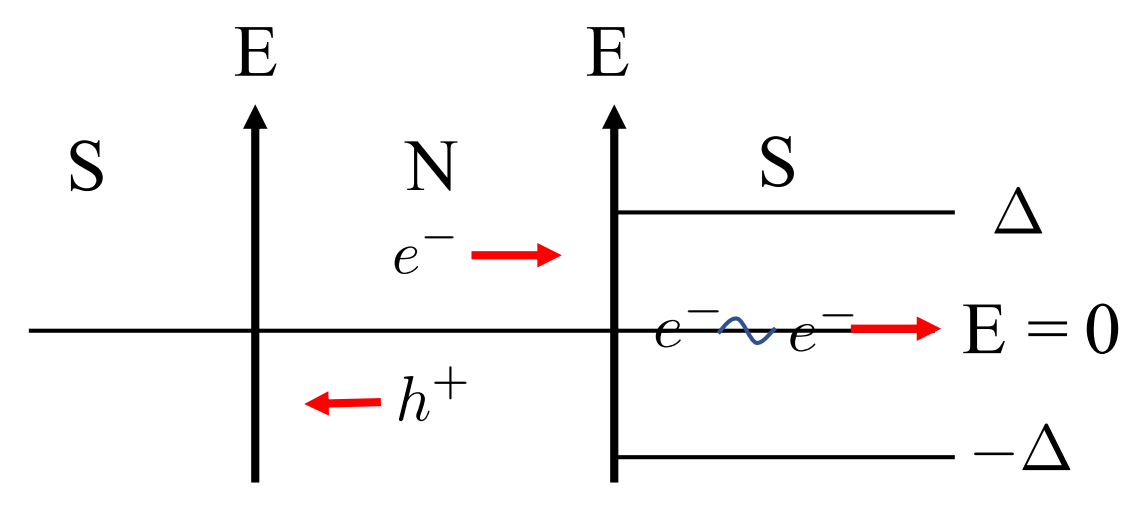


Figure 1.6: Andreev bound states formed by the electron-hole superpositions create Cooper pairs in superconductors.

We consider the scattering region as a ballistic normal metal with the Hamiltonian:

$$H = \frac{(\mathbf{p} - e\mathbf{A})^2}{2m} - \mu,\tag{1.10}$$

where \mathbf{p} is the momentum, e is the electron charge, m is the effective quasiparticle mass, \mathbf{A} is the vector potential, μ is the chemical potential. This continuum Hamiltonian can be written in the form of Eq.(1.8):

$$\sum_{\langle i,j\rangle} t_{ij} c_i^{\dagger} c_j - \mu \sum_i c_i^{\dagger} c_i \tag{1.11}$$

with $t_{ij} = t_0 e^{i\phi_{ij}}$, $t_0 = \hbar^2/(8ma^2)$, and $\phi_{ij} \propto B$ is the magnetic factor given by the Peierls substitution [78].

In our junction simulations, we follow two approaches. In the first one, we assume that the junction leads are semi-infinite and translationally invariant, which makes the lead wave functions superposition of plane waves. These plane waves are the eigenstates of the translation operator with eigenvalues given by $\lambda = e^{ik}$, where k is the momentum of the lead considered. λ can be identified by solving the Bloch equation $H(k)\phi = E\phi$, where

Bloch Hamiltonian is given by

$$H(k) = H + Ve^{-ik} + V^{\dagger}e^{ik}.$$
 (1.12)

H is the onsite potential and V is the hopping parameter. After identifying the propagating in, out and evanescense modes, we solve the Schrodinger equation through the scattering region and obtain S-matrix.

In the second approach, we assume that the system is closed with finite leads. The problem turns into an eigenvalue problem. We calculate subgap energies by diagonalizing the system Hamiltonian. The first approach is especially suitable for junctions with scattering regions having the same lattice type as the leads. We use the second approach for the junctions having scattering regions with arbitrary geometries. S-matrix calculations are faster than diagonalizing large matrices, so we also make approximations to junctions of arbitrary geometries by attaching more semi-infinite leads comparing to the real system geometry. We compare the results of the two approaches.

For the first approach, to find the ABS energies and study the spectra in short junctions (junctions with semi-infinite leads), we follow the scattering theory method and solve Beenakker's determinant equation [79]:

$$|I - \gamma X| = 0, (1.13)$$

where

$$X = RS^{\dagger}R^{\dagger}S \tag{1.14}$$

Here R represents the reflection matrix from the SN boundary and S represents the scattering matrix (S-matrix). We will give details of the calculations of Andreev energy levels and supercurrents in Chapter 5.

To find the scattering matrix S-matrix, one can use random matrix theory and generate random matrices within certain Altland-Zirnbauer symmetry classes [80]. In this thesis, we instead calculate S-matrix following the microscopic approach of Kwant package [81], as we explained above. By this way, we have more control over the system parameters. In the second approach, we calculate minimum energy levels of the system Hamiltonian and take

the ones which are smaller than the gap. These are Andreev bound states whose energies change as a function of phase. After identifying ground state energy E_g of the junction, supercurrent in the leads can be calculated using the following equation [82]:

$$I_j = \frac{2e}{\hbar} \frac{\partial E_g}{\partial \phi_j},\tag{1.15}$$

where ϕ_j is the superconducting phase of the lead j.

1.3 Computational workflow

I did my simulations in this thesis dedicated to quantum systems using classical computer clusters of the Center for High Throughput Computing (CHTC) Center and Open Science Grid [83, 84]. Classical computers are not very powerful to simulate quantum dynamics. There is a system size threshold to effectively simulate a quantum system by a classical computer. Number of quantum states grow exponentially with number of qubits. However, by dividing jobs into small parts, it is possible to get an immense speed-up comparing to simulations on personal computers. In Fig. 1.7, an example speed-up for exact diagonalization is provided. The task is performed for thousands of different parameter sets in our paper [50].

When I started doing high-throughput computing simulations in 2017 summer, I learned how to do large-scale simulations myself. I gave a talk about my computational approach during HTCondor Week 2018. I later learned many more details about large-scale computing during Open Science Grid School 2018. I am planning to increase system sizes of my simulations by incorporating techniques of high-performance computing into my research. Simulations of larger systems will help me test more ideas.

I built up an efficient scheme of high-throughput computing. I performed exact diagonalization and simulated time dynamics of systems of sizes up to eighteen spins. The statistics were taken over thousands of random disorder realizations, product states and

⁹This point was stated nicely by Feynman as: "... nature isn't classical, dammit, and if you want to make a simulation of nature, you'd better make it quantum mechanical." [10].

¹⁰Number of states of 300 qubits is more than the number of particles in the universe.

L (system size)	Memory	Time	
		Without HTC	With HTC
1	Up to 256MB	a few days	a few hours
3	Up to 256MB	~ week	half day
8	Up to 256MB	~ a few weeks	less than a day
10	Around 1000MB	~ months	~ a day
12	More than 1000MB	~ half PhD!	a few days

Figure 1.7: Memory requirement for exact diagonalization of spin system Hamiltonians. HTC stands for high-throughput computing. Column with the title "Without HTC" represents the estimated amount of time that would be spent in personal computers.

long evolutions. I divided the computation into smaller parts so that thousands of jobs with many input parameters and large output data can run in the computer clusters at the same time.¹¹

I divide big computational tasks into small parts by identifying the parts in the code which can run in parallel. Quantum toolboxes have been highly beneficial for data processing. In my spin system simulations, I use QuTiP [85, 86]. For Josephson junction simulations, I use quantum transport package Kwant [81]. The computational requirements for these packages may not be available in clusters. In order to have full control over the environment jobs running in, I use Docker images, which can be considered as virtual machines carrying the necessary toolboxes for the computation within themselves. For data analysis, I use Python libraries. I also use Veusz, which is a useful tool for scientific visualizations due to its simple GUI application. To share the Jupyter notebook results with my colleagues, I use noviewer. In the near future, I will take part in developing and using QuaC (Quantum in C) [87] for high-performance computing simulations.

 $^{^{11}\}mathrm{A}$ single file for an output data set could be larger than ${\sim}1\mathrm{GB}.$

1.4 Outline of the thesis

The outline of the thesis is given in this section. There are two main parts. First part covers theory and simulations of quantum spin systems. The second part covers multiterminal Josephson junction simulations.

In Chapter 2, we study fidelity susceptibility and time evolution of the total spin of disordered Heisenberg spin chains under local periodic drive. We evaluate the fidelity susceptibility, a measure of how a given state changes under a small perturbation, of states to a weak periodic drive. Fidelity susceptibility can be used to distinguish ergodic and many-body localized regimes. We also calculate spin accumulation of the systems with different disorder strengths. We show that the diffusion coefficient is correlated with the fidelity susceptibility and can also be used to distinguish the two phases.

In Chapter 3, we study quantum phase transitions of fluxonium qubit systems. A chain of fluxonium qubits provides the means for simulating quantum many-body phenomena in spin-1/2 magnets. The available controls allow us to map a qubit chain onto an Ising chain in a transverse magnetic field with variable parameters. The role of the transverse field is played by the tunnel-induced splitting between the lowest energy states at the half-flux sweet spot [88]. The interaction comes from the inductive qubit coupling between fluxoniums' superinductors and can exceed the level splitting [89, 63]. The magnetic flux detuning from the sweet spot plays the role of the longitudinal field for an Ising spin. We first introduce the transverse field Ising model, which is a common model for quantum phase transitions as mentioned above. We then discuss the phase diagram of the fluxonium chain. We demonstrate the quantum phase transition with the varying level splitting. We show that by using magnetization, one can study characteristics of edge states and propagating excitations.

In Chapter 4, we discuss the steered quantum adiabatic algorithm. A general timedependent quantum system can be driven fast from its initial ground state to its final ground state without generating transitions by adding a steering term to the Hamiltonian. We show how this technique can be modified to improve on the standard quantum adiabatic algorithm by making a single-particle and cluster approximation to the steering term. The method is applied to a one-dimensional Ising model in a random field. For the limit of strong disorder, the correction terms significantly enhance the probability for the whole system to remain in the ground state for the proposed non-stoquastic annealing protocol. We demonstrate that even when transitions occur for stronger interaction between qubits, the most probable quantum state is one of the lower-energy states of the final Hamiltonian. Since the method can be applied to any model, and more sophisticated approximations to the steering term are possible, the alternative technique opens up an avenue for the improvement of the quantum adiabatic algorithm.

The second part of this thesis is dedicated to multiterminal Josephson junctions. Junctions with three or more superconducting terminals gained broad interest as they provide means to study physics and topology in higher dimensions and to braid Majorana fermions for fault-tolerant quantum computation. We study effect of perpendicular magnetic field on Andreev energy levels and critical currents in a 3-terminal Josephson junction with conventional s-wave superconducting leads and a normal 2DEG scattering region. In a 3-terminal junction, currents through two terminals determine the DC Josephson effect which occurs when the two currents are limited by the boundary of the Critical Current Contour (CCC). We study the Fraunhofer diffraction patterns that manifest itself as oscillations in the diameter and area of the CCC. We show that the oscillations remain in 3-terminal devices but the additional terminal reduces the amplitude of the oscillations. We also show that magnetic field mixes with the superconducting phases in the leads and deforms the ground state energy landscape. We argue that a peculiar modulation of CCC with magnetic flux is the signature of coherent Josephson effect in multi-terminal Josephson junctions.

In addition to 3-terminal junctions with rectangular geometry, we also explore multiterminal junctions with arbitrary geometries. 4-terminal X model junction has been studied experimentally by the Manucharyan Group at the University of Maryland [75]. We simulate finite X model with leads longer than coherence length and other infinite systems as approximations to this X model and compare the results.

1.5 Publication List

The work in this thesis is presented in six chapters. The contents of Chapters 2 and 4 have appeared in two separate published works. The material of Chapters 3, 5 (Ref. [90]) and 6 (Ref. [91]) are currently being prepared for submission.

Chapter 2 is based on Ref.[92], titled Response of a quantum disordered spin system to a local periodic drive, and published in January 2020. This work was completed with Canran Xu and Maxim G. Vavilov. We thank D. Basko, M. Dykman, D. Huse, L. Ioffe, I. Martin, R. Nandkishore and V. Oganesyan for fruitful discussions. This work was supported by the U.S. Department of Energy, Office of Science, Office of Basic Energy Sciences, under Award Number DE-SC0019449. The simulations were performed using the computing resources of the UW-Madison Center For High Throughput Computing (CHTC) and resources provided by the Open Science Grid [83, 84], which is supported by the National Science Foundation award 1148698 and the U.S. Department of Energy's Office of Science. Numerical simulations were performed using QuTiP [86].

Chapter 3, titled Phase Transitions and Edge States in Fluxonium Qubit Systems, is based on the work being prepared for submission. This work has been done together with Vladimir Manucharyan, Mark Dykman and Maxim G. Vavilov. Support for this work was provided by ARO (Grant No. W911NF-18-1-0146).

Chapter 4 is based on Ref.[50], titled Steering random spin systems to speed up the quantum adiabatic algorithm, and published in December 2018. This work was completed with Robert J. Joynt and Maxim G. Vavilov. We are thankful to Sergey Knysh and Vadim Smelyanskiy for fruitful discussions. The simulations were performed using the computing resources and assistance of the UW-Madison Center For High Throughput Computing (CHTC). The work was supported by NSF EAGER Grant No. DMR-1743986.

Chapters 5 and 6 are titled as Studies of multiterminal junctions via scattering theory and Studies of finite multiterminal junctions, respectively. They are based on the work being prepared for submission as separate theory and experimental papers [90, 91] together with Maxim G. Vavilov, Vladimir Manucharyan and his group including Hanho Lee, Natalia

Pankratova and Roman Kuzmin. Fruitful discussions with Caglar Girit and Vlad Pribiag were helpful. The work was supported by ARO, LPS Grant No. W911NF-18-1-0115.

Part I Quantum Spin Models

Chapter 2

Response of a quantum disordered spin system to a local periodic drive

2.1 Introduction

Focus of MBL studies was to understand interacting many-body spin systems with random field. Interacting electrons and spin-1/2 chains are closely related models. The spinless electron system can be mapped onto XXZ chain via Jordan-Wigner transformation [93]. The onsite energy in the fermionic system corresponds to random z-field in the spin chain model.

Both fermionic systems and spin chains with disorder have been shown to exhibit MBL transition in Refs [94, 95, 96, 97, 98, 99, 100, 101]. This transition between localized and ergodic regimes can be characterized via entropy growth [102, 103], localization length [103], energy spectrum [104, 105], local integrals of motion [106, 107, 108, 109, 110] and entanglement [103, 102, 111, 112].

We present our results for the short time scales when the system may not have reached its saturation value yet. We consider a one-dimensional Heisenberg spin chain system with quenched disorder driven by a local ac field. The static Heisenberg Hamiltonian with the periodic boundary condition $\vec{\sigma}^{(L+1)} = \vec{\sigma}^{(1)}$ is given by

$$H_0 = \sum_{l=1}^{L} \left[J\boldsymbol{\sigma}^{(l)} \boldsymbol{\sigma}^{(l+1)} + h_l \sigma_z^{(l)} \right]. \tag{2.1}$$

Here, $\sigma^{(l)}$ is the vector of Pauli matrices for spin at site l. The onsite fields h_l are independent random fields, uniformly distributed in the range [-W, W], where W is the disorder strength of the system. We use J as a fundamental unit and set J = 1 throughout the rest of this chapter.

The system with Hamiltonian (2.1) conserves the total z-component of spin

$$S_z = \frac{1}{2} \sum_{l} \sigma_z^{(l)},\tag{2.2}$$

A transverse ac drive is applied to a single spin

$$V(t) = f[\cos(\omega t)\sigma_x^{(1)} + \sin(\omega t)\sigma_y^{(1)}], \qquad (2.3)$$

which breaks the conservation of S_z . Here, f denotes the strength of the drive, ω is the drive frequency and $\tau = 2\pi/\omega$ is the period of the drive. We investigate the time evolution of the system described by the time-dependent full Hamiltonian

$$H(t) = H_0 + V(t). (2.4)$$

We perform analysis of fidelity susceptibility [62] and change in system dynamics of total spin as the strength of disorder changes from weak to strong.

Fidelity susceptibility was previously used to study phase transition [113, 114, 115, 116, 117]. In this chapter, we study fidelity susceptibility as a measure of overlap between the two quantum states $|\langle \psi_{f=0} | \psi_{f\neq 0} \rangle|^2$ that evolve with or without drive from the same initial state $|\psi_i\rangle$, where $\overline{(...)}$ stands for the average over initial states $|\psi_i\rangle$. For weak drive, the quantum displacement is proportional to the fidelity susceptibility. Evolution of an initial state may follow different paths in the Hilbert space depending on the phase of many-body systems. An important factor that defines the quantum displacement between the two final

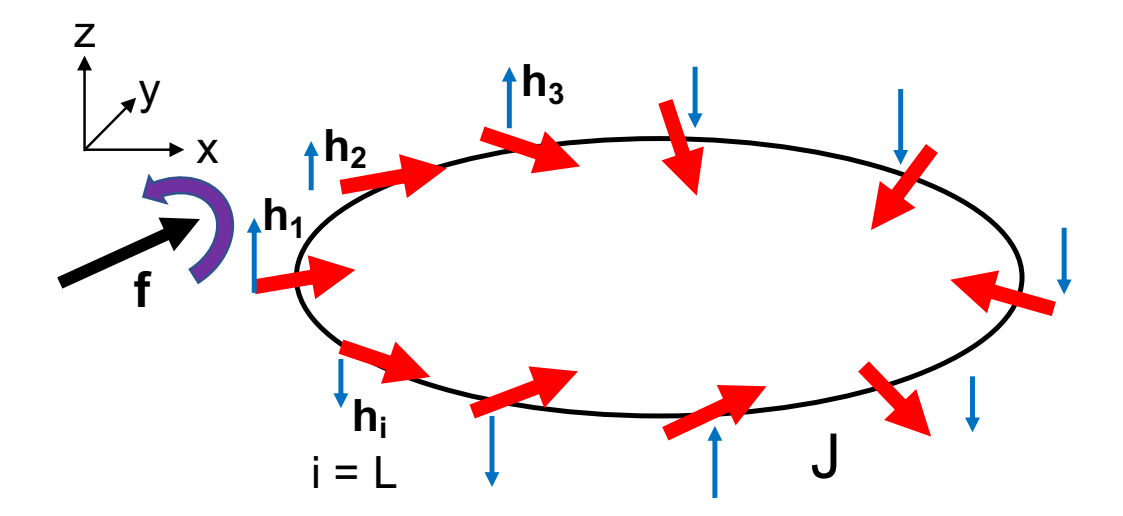


Figure 2.1: (Color online) Heisenberg spin-1/2 chain system with quenched disorder $\{h_l\}$ in the z-direction. $\{h_l\}$ is defined by the uniform distribution within the interval $|h_l| \leq W$. W is the disorder strength and the interaction strength between the nearest neighbors is given by the unitless parameter J=1. There is a local ac drive with strength f on the spin labeled by i=1 in the x-y plane rotating with drive frequency ω in the anticlockwise direction.

states is disorder. When the disorder is weak, the distance between the two final states is large. However, for strong disorder, localization occurs and the distance vanishes.

The local drive (2.3) breaks the S_z -conservation law. We show that spin accumulation in response to the drive could be a viable experimental method to distinguish between localized and ergodic regimes. The variance of operator S_z with respect to an arbitrary quantum state $|\psi(t)\rangle$ of the system at time t is

$$\delta S_z^2(t) = \langle S_z^2(t) \rangle - \langle S_z(t) \rangle^2, \tag{2.5}$$

where, $\langle A(t) \rangle$ is defined as $\langle A(t) \rangle \equiv \langle \psi(t) | A | \psi(t) \rangle$. We perform an analysis of the statistical properties of the spin accumulation $\delta S_z^2(t)$ over disorder realizations. We study the average of $\delta S_z^2(t)$ as a function of time $t=n\tau$, where n is the number of periods. The statistics of spin accumulation is significantly different for the ergodic and MBL regimes and the difference between the spin accumulation over time can be used to distinguish between the two regimes. The change in $\delta S_z^2(t)$ after one period can be identified as the total spin

diffusion coefficient. We compare the quantum displacement at one period with the diffusion coefficient $\delta S_z^2(\tau)$ and show that they have similar behavior. We analyze the distribution of the diffusion coefficient for different disorder strengths. The distributions are different for the MBL and ergodic regimes. The diffusion coefficient is large and the distribution is narrow for weak disorder, whereas the diffusion coefficient is small and the distribution is wide and has a long tail for the strong disorder.

2.2 Fidelity susceptibility at weak drive

The analysis of quantum displacement has been performed in Canran Xu's PhD thesis [118]. In this section, we provide improved figures for the quantum displacement for larger systems with more disorder realizations (Figs. 2.2 and 2.3) and relate quantum displacement to fidelity susceptibility. We further relate fidelity susceptibility to spin variance in the following sections and will study the correlation between the two.

System Hamiltonian given in Eq.(2.4) can be transformed into time-independent Hamiltonian under a unitary basis transformation:

$$\tilde{H} = \tilde{H}_0 + f\sigma_x^{(1)}, \quad \tilde{H}_0 = H_0 - \omega S_z.$$
 (2.6)

For a given initial state ψ_i , we consider evolution of it under the driven and undriven Hamiltonians. The Fubini-Study distance between the states after time τ is given by:

$$F_{\psi_i} = |\langle \psi_0(\tau) | \psi_f(\tau) \rangle|^2 = |\langle \psi_i | \mathcal{U} | \psi_i \rangle|^2, \qquad (2.7)$$

where $\psi_0(\tau)$ is the state evolved under the Hamiltonian without drive and $\psi_f(\tau)$ is the state evolved under the driven Hamiltonian. Here, \mathcal{U} is the operator giving the mismatch between these two states:

$$\mathcal{U} = U_0^{\dagger} U_f, \tag{2.8}$$

where $U_f = (-1)^L \exp(-i\tilde{H}\tau)$ and $U_0 = U_{f\to 0} = \exp(-iH_0\tau)$. L is the number of spins.

¹ "Dimensionless power", which is proportional to infidelity, was studied in Canran Xu's thesis. We use the phrase "quantum displacement" here and define it below.

Fubini-Study metric is known as quantum geometric tensor in the adiabatic limit. The imaginary part of the quantum geometric tensor gives the Berry curvature. Both real and imaginary parts of the quantum geometric tensor can be used as susceptibility to measure phase transitions [119]. Here, to identify phases, we use fidelity susceptibility for the weak drive, which is defined in the next section.

The average fidelity over all initial states is given by [120] (as cited in [118]):

$$F = \frac{M + |tr(\mathcal{U})|^2}{M(M+1)}.$$
 (2.9)

We define quantum displacement between the two final states after one period as in the following:

$$\varepsilon \equiv 1 - F. \tag{2.10}$$

The distribution of the quantum displacement is given in Fig. 2.2. The quantum displacement depends on the disorder strength as shown in Fig. 2.3. These figures are improved versions of the ones available in [118] with more disorder realizations and for larger systems.

In the weak drive limit, quantum displacement is proportional to the fidelity susceptibility. Here, we explain the relation between the two. Two initial same states are evolved under unperturbed and perturbed Hamiltonians for a period. We calculate the quantum displacement ε given by Eq.(2.10) between the two final states after a period, which is independent of the given initial state and depends only on the mismatch between the energy eigenstates of the unperturbed Hamiltonian and Floquet basis. When the drive strength f is small, we can write the Maclaurin series expansion for the fidelity in Eq. (2.7) around f = 0:

$$F = 1 - \frac{f^2}{2}\chi_F + \dots, (2.11)$$

and we neglect the higher order terms. Here χ_F is defined as the *fidelity susceptibility* and it is the second derivative of the fidelity with respect to the drive amplitude f [62]. In the small f limit, χ_F can be written in terms of fidelity F:

$$\chi_F = 2(1-F)/f^2 = 2\varepsilon/f^2.$$
 (2.12)

Note that χ_F is proportional to the quantum displacement ε given by Eq. (2.10).

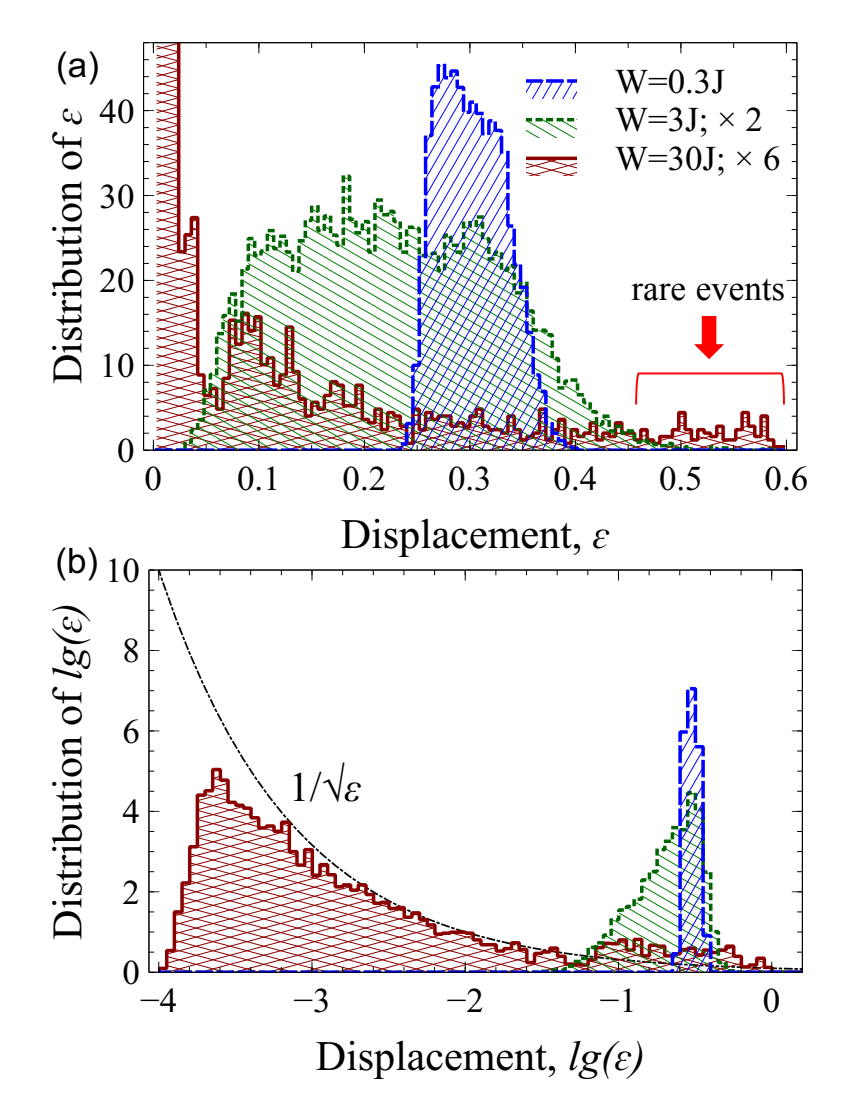


Figure 2.2: (Color online) (a) Distribution of quantum displacement ε over $N=10^4$ realizations of the random magnetic field h_l for a system with L=12 spins. The top panel shows the distribution of the displacement itself for W/J=0.3 (blue long-dashed line), W/J=3 (green short-dashed line), and W/J=30 (red solid line). Distributions for strong disorder have exponentially large tails. Rare events appear for the strong disorder. (b) Logarithm of the distribution of ε for the same three values of disorder as in (a). The dash-dotted line represents the slope $\sim 10^{-1/2(\lg(\varepsilon))} = 1\sqrt{\varepsilon}$. The drive amplitude $f=J/\sqrt{10}$ and $\omega=J$. Ig shows \log_{10} throughout the text. We scaled the distribution curves for W/J=3 by factor two and for W/J=30 by factor six.

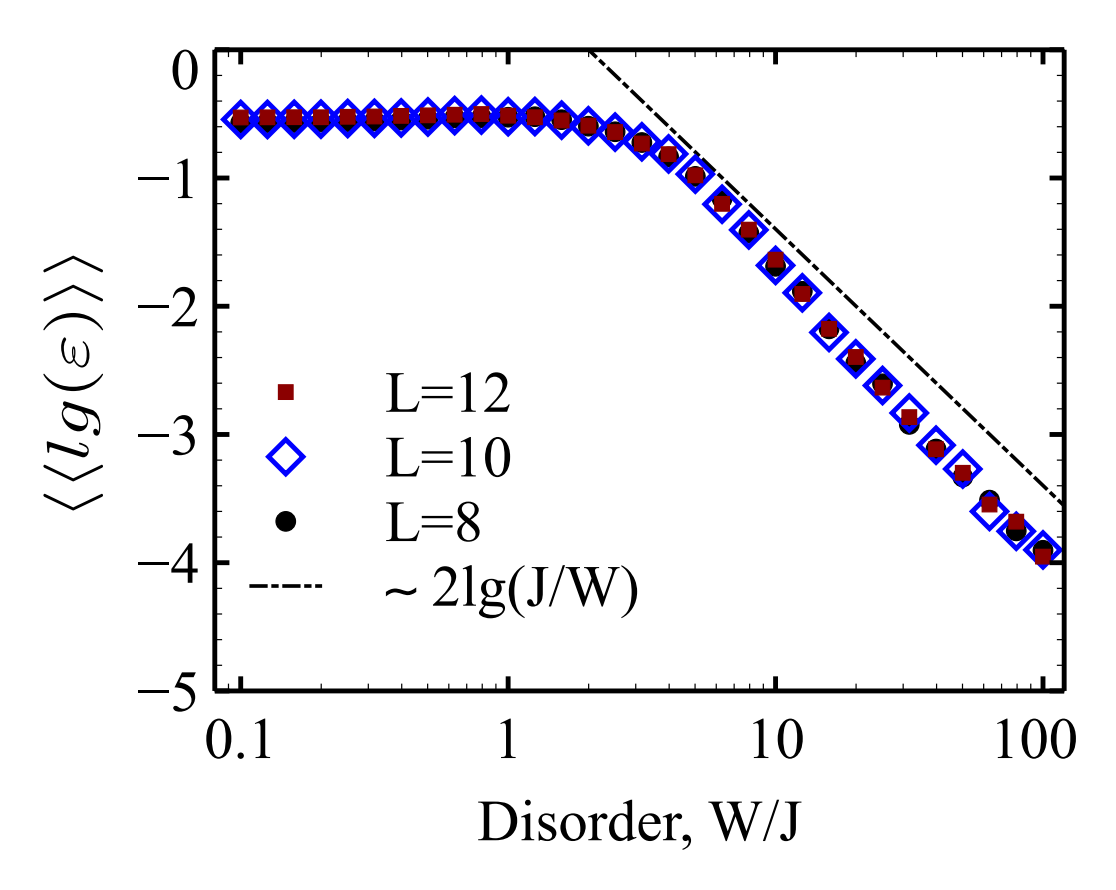


Figure 2.3: (Color online) Average of the logarithm of quantum displacement, $\lg(\varepsilon)$, as a function of disorder strength W for a spin system of size L=8 (circles), L=10 (squares) and L=12 (diamonds). The average is evaluated over $N=10^3$ disorder samples for $L=8,\ 10,\ 12$. The drive amplitude $f=J/\sqrt{10}$ and $\omega=J$. $\langle\langle\rangle\rangle$ shows the disorder average throughout the chapter.

2.3 Time evolution of the total spin

In this section, we describe a technique to distinguish between ergodic and MBL phases using the total spin projection in the z-direction S_z , given by Eq.(2.2). It has been shown that magnetization can be a probe to distinguish between ergodic and MBL phases [121]. Here, we study the variance of total spin in the z-direction that gives the measure of localization for a given state [122]. The total spin projection in the z-direction is a conserved quantum number of H_0 , Eq. (2.1). When there is a local periodic drive perpendicular to the z-direction, S_z is not conserved anymore. The value of S_z with respect to time depends on the strength of the random field W. For the variance of S_z given by Eq. (2.5), $\delta S_z^2(t)$,

we observe different statistics for the ergodic and MBL phases.

We choose the initial state as a product state with $S_z = 0$. Such product states can be shown as $|\psi\rangle = |\{\sigma_i\}\rangle$ with $\sigma_i = \pm 1$, $\sum_i \sigma_i = 0$, where +1 represents spin up and -1 represents spin down for even system size L. There are $L!/((L/2)!)^2$ product states with $S_z = 0$. For systems of size up to L = 12, it is computationally feasible to take the average $\overline{\delta S_z^2(t)}$ (product state average is shown by an overbar) over all product states along with disorder average. For the sizes beyond L = 12, we took the average over some group of randomly selected product states. Even a small group of samples can be useful to identify the phase of the system. By analyzing statistical dynamics of product states, we can study the ergodic and MBL phases. By using time dynamics, one can simulate larger systems compared to the spectral analysis because exact diagonalization is computationally more intensive.

Short time growth of $\delta S_z^2(t)$ can identify the phase of the system.² Fig. 2.4 shows how the average variance $\langle \langle \overline{\delta S_z^2(n\tau)} \rangle \rangle$ changes with respect to the number of periods, n.³ The average is taken over product states (shown by the overbar) and disorder (shown by double angle brackets). In the ergodic regime, the variance changes quickly for the initial periods and reaches a saturation point for longer times. For L=14, the saturation point is reached in less than one hundred cycles of drive. For larger systems, it takes more time to reach the saturation point. One can estimate based on the decreasing rate of change of the variance with time that it does not take exponentially long time to reach the saturation for systems with L=16 and 18 in the ergodic regime. However, in the MBL regime, the variance increases slowly and based on the monotonous increase rate one can estimate that it takes much more time to reach a saturation point compared to the ergodic case. In addition, the variance change in the MBL regime is less sensitive to the system size than in ergodic regime. In Fig. 2.4(b), we demonstrated for different initial conditions and product states

²Short time change of correlation functions have also been found useful to identify localization properties of the quantum many-body systems as discussed in [123].

³We also compared the spin accumulation for W=0 (zero disorder) with the ergodic (W=1.25) and MBL (W=5) cases. We observed that when there is no disorder, the behavior of variance is quite different than the evolution in the ergodic regime, so W=0 case cannot simply be studied by choosing $W\longrightarrow 0$ and deserves a separate analysis.

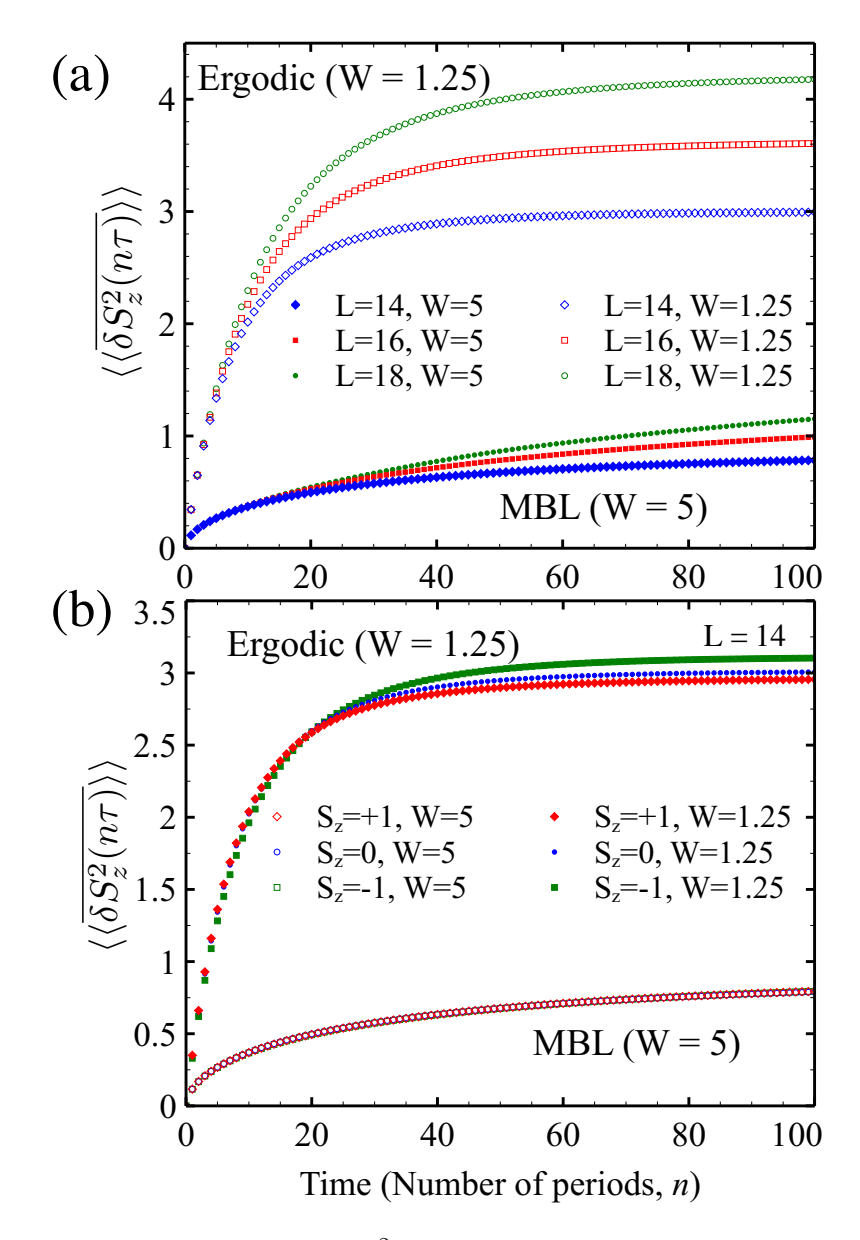


Figure 2.4: (Color online) (a) Average $\delta S_z^2(t)$ as a function of time for a spin system of size L=14 (diamonds), L=16 (squares) and L=18 (circles). Curves for W=1.25 have filled and for W=5 have unfilled markers. The averages are performed over 10^3 realizations of disorder for all system sizes and 10^3 product states for L=14, 150 product states for L=16 and 60 product states for L=18. The overbar shows the product state average throughout the chapter. (b) Average $\delta S_z^2(t)$ as a function of time for a spin system of size L=14 and W=1.25 or 5. Results are compared for the initial product state with $S_z=\pm 1$ and 0 at t=0. For all cases, 100 product states and 10^3 disorder averages are considered.

 $(S_z = 0 \text{ vs.} \pm 1)$ that one can still distinguish between ergodic and MBL regimes regardless of the initial S_z choices. In MBL regime (W = 5), the spin accumulation takes almost the same values and the curves are aligned with each other. In ergodic regime (W = 1.25), the spin accumulation for the three different initial S_z values slightly differ. The reason for this slight difference between $S_z = \pm 1$ is the sine term in Eq.(2.3), which is an odd function and breaks the symmetry with respect to the local field rotation direction.

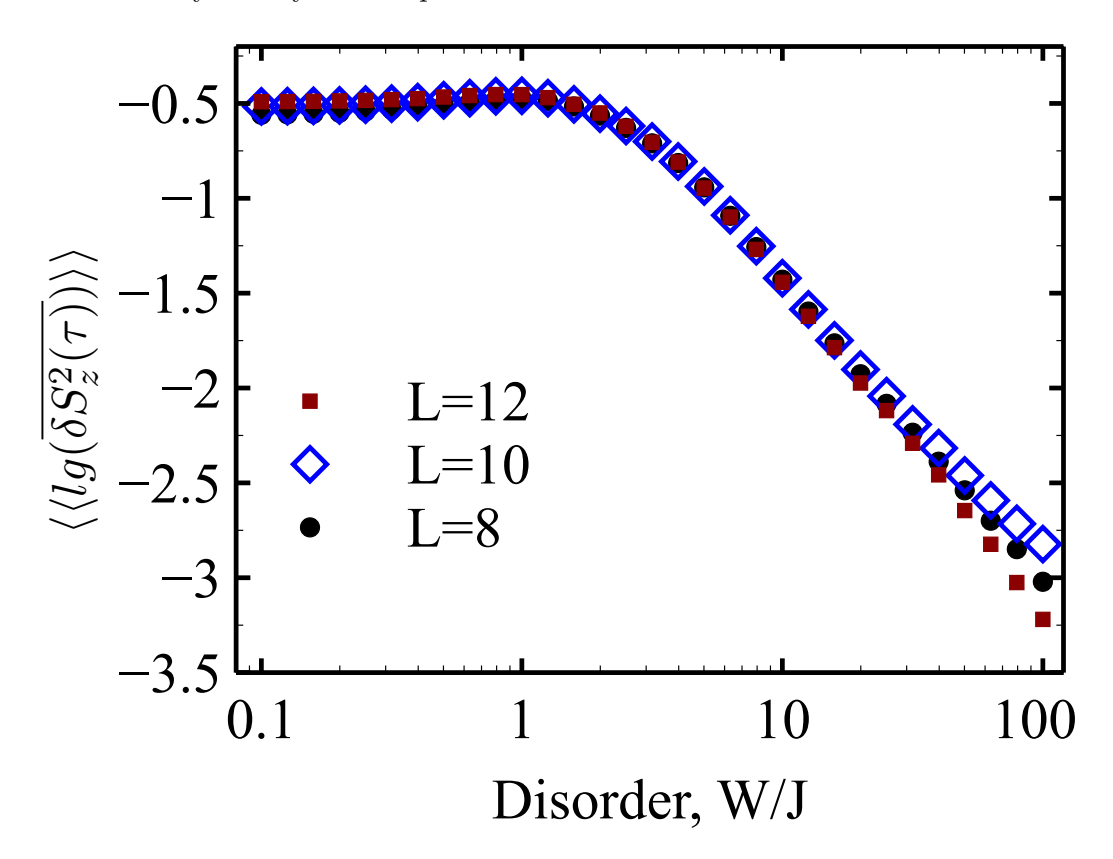


Figure 2.5: (Color online) Average $\delta S_z^2(\tau)$ as a function of $\lg(W/J)$ for a spin system of size L=8 (circles), L=10 (squares) and L=12 (diamonds). Time = 1 period. $f=J/\sqrt{10}$ and $\omega=J$. The averages are performed over 10^4 disorder realizations for L=8, 10^3 disorder realizations for L=10, L=12. All product states are considered for all system sizes for product state averaging.

In Fig. 2.5, we show how the average of logarithm of the variance, $\langle\langle \lg(\overline{\delta S_z^2(\tau)})\rangle\rangle\rangle$, changes with respect to the disorder strength W. Time is fixed at one period, τ . The variance curves in Fig. 2.5 shows similar properties as the quantum displacement curves in Fig. 2.3. $\delta S_z^2(t)$ changes weakly with disorder strength at weak disorder $(W \lesssim 3J)$, whereas it decreases

linearly with $\lg(W/J)$ at stronger disorder $(W \gtrsim 3J)$. Similar to the quantum displacement, $\delta S_z^2(t)$ also does not strongly depend on the system size L.

In Fig. 2.6, we show the probability distribution of $\lg(\overline{\delta S_z^2(\tau)})$. The distributions are narrow and the typical value of $\overline{\delta S_z^2(\tau)}$ is large at weak disorder, whereas the distributions broaden and the typical value of $\overline{\delta S_z^2(\tau)}$ is small at strong disorder. For the quantum displacement, we showed in the previous section that the distribution of $\lg(\varepsilon)$ is a Pareto distribution. $\lg(\overline{\delta S_z^2(\tau)})$ distributions for strong disorder have longer tails but not as long as the distributions of quantum displacement ε . However, it is still possible to distinguish between localized and ergodic phases based on $\lg(\overline{\delta S_z^2(\tau)})$ distributions for different disorder strengths even though rare events do not appear and distribution is spread out in a smaller range in the strong disorder.

We compare the typical values of the displacement ε with the spin diffusion coefficient $\overline{\delta S_z^2(\tau)}$. We demonstrate the correlation between $\langle\langle\lg(\varepsilon)\rangle\rangle$ and $\langle\langle\lg(\overline{\delta S_z^2(\tau)})\rangle\rangle$ by the parameter plot provided in Fig. 2.7(a). This behavior of $\langle\langle\lg(\varepsilon)\rangle\rangle$ and $\langle\langle\lg(\overline{\delta S_z^2(\tau)})\rangle\rangle$ supports our claim that the total spin measurement can also be used to identify the localization properties of the system. We also provide scatter plots in Figs. 2.7(b, c, d) for three of the disorder-unaveraged values from Fig. 2.7(a) with W=1 (ergodic regime), 3.16 (critical regime) and 10 (MBL regime). The distributions for both $\lg(\varepsilon)$ and $\lg(\delta S_z^2)$ are wide in the localized phase with large disorder strength and the typical values of ε and $\overline{\delta S_z^2}$ are small. For smaller W, the distributions get narrower and the typical values are bigger. We deduce from the shape of the clouds in the scatter plots in Figs. 2.7(b, c, d) that the correlation between $\lg(\varepsilon)$ and $\lg(\delta S_z^2)$ are small.⁴ However, as we pointed out, the average values of them are correlated as shown in the parameter plot in Fig. 2.7(a).

2.4 Discussion and Conclusions

We analyzed the overlap between the states started from the initial states $|\psi_i\rangle$ and evolved under the Heisenberg Hamiltonian with and without drive. We also studied the variance

⁴We used cross-correlation to calculate the correlation between $\lg(\epsilon)$ and $\lg(\overline{\delta S_z^2})$

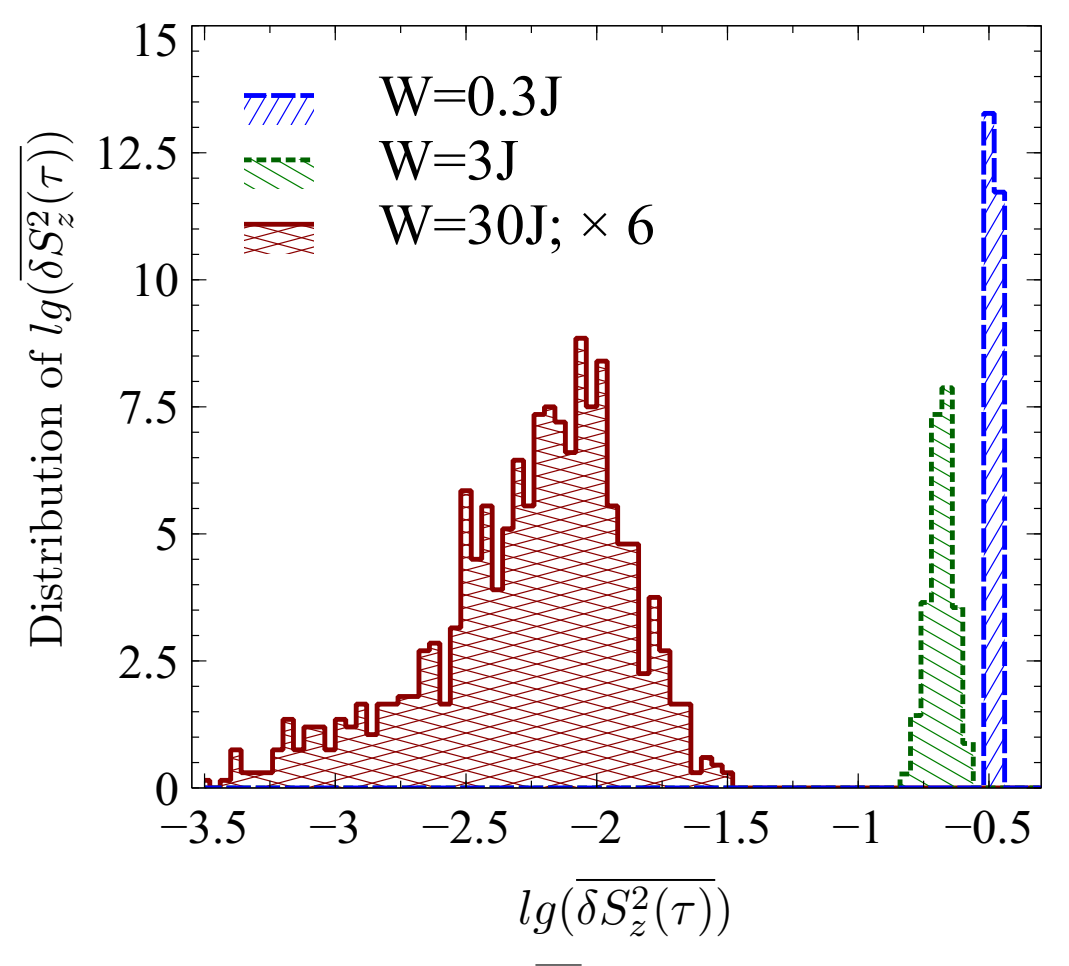


Figure 2.6: (Color online) Distribution of $\lg(\overline{\delta S_z^2})$ over $N=10^3$ disorder realizations of the random magnetic field h_l for a system with L=12 spins for W/J=0.3 (blue long-dashed line) and W/J=3 (green short-dashed line), 30 (red solid line). We scaled the distribution curve for W/J=30 by factor six. The averages are performed over all product states of the system.

of the operator for total spin in z-direction $\delta S_z^2(t)$, given by Eq.(2.5), for an initial state prepared as a product spin state with total spin projection equal to zero. Thus, $\delta S_z^2(t)$ is a measure of spin accumulation due to the drive and can be used to measure the speed of the thermalization in the ergodic and MBL regimes. Both initialization of this system as a product state of individual spins in z-direction and measurement of their net spin projection are basic requirements for quantum hardware and experimental studies of crossover from the ergodic to localized regimes through the spin polarization dynamics is feasible in available systems similar to those described in Refs. [34, 35, 37, 36, 38, 63].

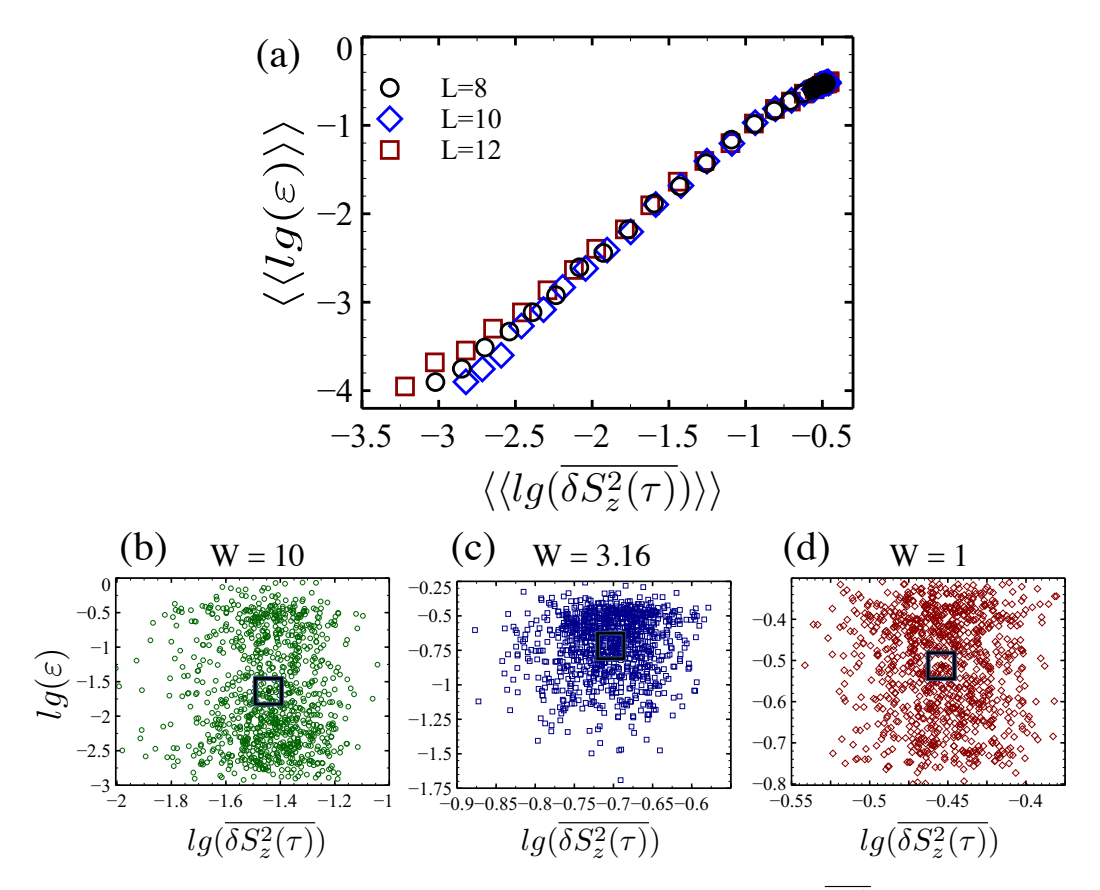


Figure 2.7: (Color online) (a) Parameter plot of $\langle\langle\lg(\varepsilon)\rangle\rangle$ and $\langle\langle\lg(\overline{\delta S_z^2})\rangle\rangle$ for a spin system of size L=8 (circles), L=10 (diamonds) and L=12 (squares). Data points from Figs. 2.3 and 2.5 are used. Time = 1 period. The drive amplitude $f=J/\sqrt{10}$ and $\omega=J$. There is almost a linear dependence between the two quantities. (b, c, d) Scatter plots of the data for the three of the results for L=12 from (a). W=1 (red diamond), 3.16 (blue square) and 10 (green circle). Each scatter plot includes 10^3 unfilled markers each of which corresponds to a single disorder realization. Each average value in plots of (b, c, d) is in a big black square and is shown by a filled marker of same type as the scattered data.

We calculated the spin accumulation in response to the drive over time t, the results are shown in Fig. 2.4. In the ergodic regime, the spin accumulation speed is large in the initial periods and total spin gets saturated rapidly. However, in the MBL regime, the spin accumulation is slower in the initial periods and the spins are still drifting in response to the drive in the longer time limit. The spin accumulation after one period gives the spin diffusion coefficient $\delta S_z^2(\tau)$. The behavior of the diffusion coefficient is very similar to the behavior of quantum displacement ε . As illustrated in Fig. 2.5, at weak disorder, diffusion coefficient is large and changes weakly with the disorder strength. However, at strong disorder, the diffusion coefficient decreases linearly with the logarithm of the disorder strength, lg(W/J), and eventually diffusion is broken. The system may show subdiffusive dynamics as recently pointed out in [124]. Furthermore, diffusion coefficient does not depend on the system size strongly similar to quantum displacement.

Probability distributions for the diffusion coefficient show different characteristics depending on the disorder strength as can be seen in Fig. 2.6. At weak disorder, the distribution is narrow and the typical value of the diffusion coefficient is large. At strong disorder, the distribution is wide and have long tail but unlike the distributions for the quantum displacement, the distribution for the diffusion coefficient does not have exponentially long tail and does not exhibit rare events. However, it is still possible to identify the phase of the system based on the diffusion coefficient distributions. The broad distribution of $\delta S_z^2(\tau)$ at strong disorder shows that this parameter cannot be seen as a one-fit-all parameter. In other words, there is a different dynamics at strong disorder.

In Fig. 2.7, we demonstrated that there is a positive correlation between the quantum displacement and spin accumulation. However, we note that flips of a spin have different effects on the quantum displacement and the spin accumulation. If a single spin flips, the original and new states, $|\psi\rangle$ and $|\psi'\rangle$ respectively, are orthogonal. That makes the displacement $1 - |\langle\psi|\psi'\rangle|^2$ between the states equal to 1. However, in the large system size $(L \gg 1)$ limit, one spin flip produces a small effect for the total spin $\sim L$ in the z-direction and therefore also for the spin accumulation $\delta S_z^2(t)$. Even though spin flips have

smaller effects on the spin accumulation, there is a clear difference between the speed of the thermalization for the two phases as explained above.

Our study was focused on a local harmonic drive with moderate drive frequency ($\omega \simeq J$). For this frequency, we observed that thermalization occurs regardless of whether the system is in the localized or ergodic regimes, which supports the results of [125, 126, 37], and the speed of thermalization is different for the two cases. On the other hand, one could also consider the cases where ω is much smaller or larger than J. In the limit of $\omega \ll J$, the time-independent Hamiltonian in the rotated frame will be similar (with difference of ωS_z) to the Hamiltonian with DC perturbation considered in [105]. If the drive frequency is larger than the depth of the local energy minima, different regimes such as prethermal states occur [127, 128]. Most closed many-body systems tend to heat up when they are driven. The situation is different for driven localized systems when many local deep minima appear in the energy spectrum and prevent thermalization. The system is prevented from heating up, which can be understood via quantum mechanics of energy levels. If the drive frequency is large, the system cannot absorb all the energy provided by the drive. Instead, the energy absorption requires many-body excitations and slows heating down exponentially [129, 130]. Under certain nonequilibrium conditions of prethermalization, the systems can exhibit topological phases protected by time-translation symmetry [131, 132, 133, 134] and time crystals where time-translation symmetry is spontaneously broken [135, 136, 137, 127, 138, 139, 140, 128, 141]. Exploring statistics of the system responses at high frequency periodic drive was not addressed here and is the topic of a separate study.

Chapter 3

Phase Transitions and Edge States in Fluxonium Qubit Systems

3.1 Introduction

A chain of inductively coupled fluxonium atoms tuned at or around their sweet spots can be used to simulate strongly interacting spin-1/2 chains thanks to their high coherence and anharmonicity. In Chapter 2, we used fidelity susceptibility to study phase crossover of disordered spin chains. In this chapter, we will study quantum phase transitions of fluxonium qubit systems using fidelity susceptibility. We first show how a fluxonium atom system can be mapped onto spin-1/2 Ising chain.¹ Then we will study phase diagram of antiferromagnetic transverse Ising chain in a longitudinal field in the parameter range of fluxonium atoms. The phase diagram shows the energy gap between the ground and first excited states, which determines the phase of the system. Since the coupling strength of a fluxonium atom can exceed the level splitting, we can explore topological regimes using fluxonium qubits. We use the mapping between transverse Ising model and Majorana nanowires to discuss edge states using the magnetization at each site. We will also discuss effects of disorder. Identifying whether the phase boundary is robust against disorder

¹For this chapter, we use transverse Ising model with XX interaction in a longitudinal field.

or not and discussions on Majorana nanowires are part of our ongoing studies. Using magnetization for another experimentally accessible purpose, we propose that the response of qubits to a spin flip can be studied using fluxonium chains.

3.2 Mapping fluxonium chain onto transverse Ising chain in a longitudinal field

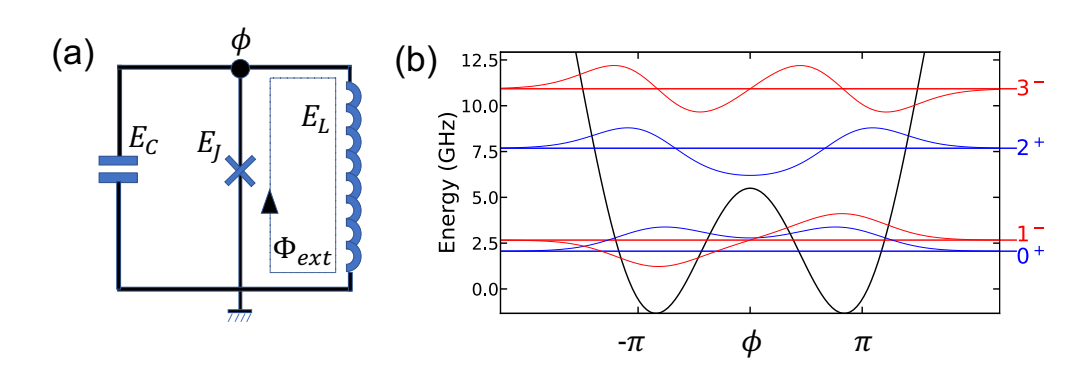


Figure 3.1: (a) Fluxonium circuit. (b) Energy level diagram of a fluxonium qubit at the sweet spot, $\phi_{ext} = \pi$. $V(\phi)$ is a double-well potential. Energy eigenstates are also provided with numbers. They are in the order of increasing energy from bottom to top. 0 corresponds to the ground state. +, - signs represent the even and odd functions, respectively.

The fluxonium circuit and its energy level diagram are given in Fig. 3.1. The capacitor, Josephson junction and the superinductor have energies shown by $E_C = e^2/2C$, E_J and $E_L = (\hbar/2e)^2/L$, respectively. Fluxonium works in the parameter regime where $E_J >> E_L$ and $1 \lesssim E_J/E_C \lesssim 10$. There is no need for large capacitance but a large inductance is needed. Large inductance is provided by the superinductor, which is a chain of around a hundred Josephson junctions [63].

The Hamiltonian for the fluxonium atom is given by [142, 143]

$$H = 4 E_C n^2 + V(\phi), \tag{3.1}$$

where n and ϕ are the charge and flux operators, respectively. ϕ is the flux across from the inductor. There is external magnetic flux Φ_{ext} through the loop formed by the Josephson

junction and the superinductor. The operators n and ϕ satisfy the commutation relation $[\phi, n] = i$. The potential energy is given by

$$V(\phi) = \frac{1}{2} E_L \phi^2 - E_J \cos(\phi - \phi_{ext}), \tag{3.2}$$

where ϕ_{ext} is the reduced magnetic flux and it is the unitless form of the external flux $\Phi_{ext} = (\hbar/2e)\phi_{ext}$.

Fluxonium systems operated at or around the half-flux sweet spot $\phi_{ext} = \pi$ have high coherence and anharmonicity and resilience against flux noise [64]. $V(\phi)$ is a double-well potential at the sweet spot as shown in Fig. 3.1(b). Energy levels and wave functions are also provided together with $V(\phi)$. We obtain the transverse field (in z-direction) via tunnel-induced splitting. One can write the Hamiltonian of the fluxonium atom in energy eigenstate basis as

$$H_{Energy} = \epsilon_0 |0\rangle\langle 0| + \epsilon_1 |1\rangle\langle 1| + ..., \tag{3.3}$$

where ϵ_0 and ϵ_1 are ground and first excited state energies, respectively. Since second excited level shown in Fig. 3.1(b) is much higher than the ground and first excited levels, we can truncate H_{Energy} into ground and first excited states

$$H_{Truncated} = \alpha \mathbb{1} + h^z \sigma_z, \tag{3.4}$$

where \mathbb{I} is the identity matrix, $\alpha = \frac{\epsilon_1 + \epsilon_0}{2}$ and $h^z = \frac{\epsilon_1 - \epsilon_0}{2}$ is the energy splitting between ground and first excited levels (less than 1GHz as shown in Fig. 3.1(b)). h^z has been shown to be proportional to $\exp(-8\sqrt{E_J/E_C})$ [144, 145]. For a high barrier between the two wells, ground and first excited states are localized in the two minima. To induce tunneling, E_J should not be too large.

The longitudinal field (in x-direction) can be obtained via the flux detuning away from the sweet spot [88, 63] . The potential energy change due to detuning (varying ϕ) is given by

$$\delta V = \sin(\phi) \,\delta\phi_{\rm ext}.\tag{3.5}$$

Sine is an odd operator. As can be seen in Fig. 3.1(b)), $|0\rangle$ and $|1\rangle$ are even and odd functions, respectively. Therefore, 00 and 11 matrix elements are integrals of odd function

(sine preserve its character) from minus infinity to plus infinity, so we get the matrix elements for the diagonal terms as

$$\langle 0|\sin(\phi)|0\rangle = \langle 1|\sin(\phi)|1\rangle = 0. \tag{3.6}$$

Due to a similar argument, 01 and 10 matrix elements are integrals of even functions. Therefore, the nondiagonal terms are nonzero:

$$\langle 0|\sin(\phi)|1\rangle = \langle 1|\sin(\phi)|0\rangle \neq 0.$$
 (3.7)

One can conclude that the operator $\sin(\phi)$ has the same structure as the Pauli x matrix in the computational basis.

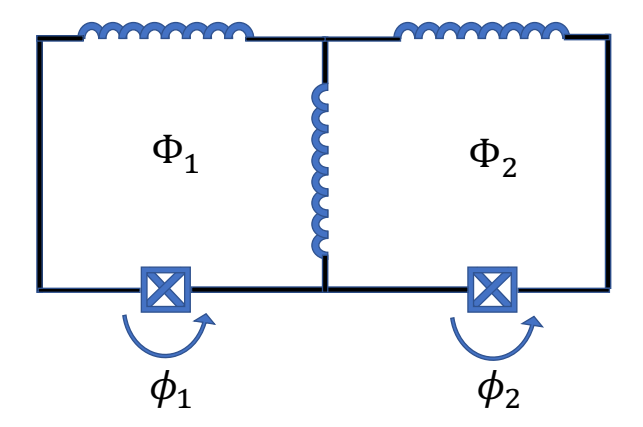


Figure 3.2: Chain of two fluxonium atoms. Ising interaction is formed by the inductive coupling between two superinductors.

Ising XX interaction can be obtained via the inductive coupling between superinductors as shown in Fig. 3.2, the "fluxonium molecule" [89]. The term $\propto E_L \phi_1 \phi_2$ is the interaction term in the fluxonium molecule Hamiltonian. The fluxes ϕ_1 and ϕ_2 are odd functions similar to sine. They also have the Pauli x matrix character in the computational basis. Therefore, $\phi_1 \phi_2$ interaction term can be mapped onto $\sigma_x^{(1)} \sigma_x^{(2)}$. E_L corresponds to the interaction parameter J in Ising Hamiltonian. The interaction can be stronger than the qubit energy. By inductively coupling fluxonium atoms similarly, one can obtain the Ising interaction term $J \sum_{l=1}^{L-1} \sigma_x^{(l)} \sigma_x^{(l+1)}$.

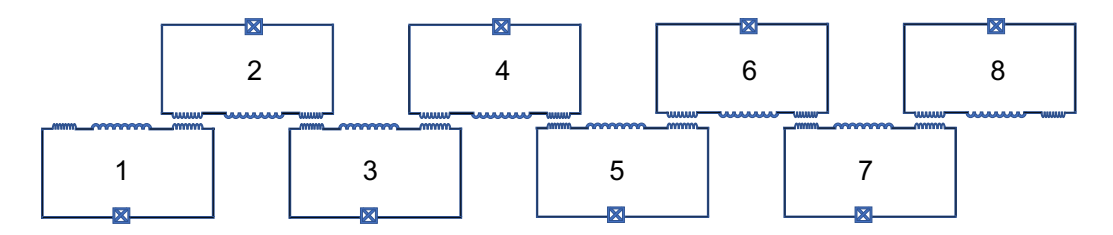


Figure 3.3: Open chain of 8 fluxonium atoms. Each fluxonium atom is numbered.

Using these mappings, we can build a chain of fluxonium qubits similar to the one provided in Fig. 3.3 giving the transverse Ising Hamiltonian in a longitudinal field:

$$H_T = J \sum_{l=1}^{L-1} \sigma_x^{(l)} \sigma_x^{(l+1)} - \sum_{l=1}^{L} h_l^x \sigma_x^{(l)} - \sum_{l=1}^{L} h_l^z \sigma_z^{(l)}.$$
 (3.8)

3.3 Phase diagram

In this section, we will study the phase diagram of this system in the range of fluxonium parameters. We choose J = 500 MHz and study the phase diagram within the range of $h_x, h_z < 1 \text{GHz}$, which is about the energy splitting between the first excited and ground states of a fluxonium atom. So, we are studying both the interaction parameter J is stronger or weaker than h_x, h_z .

The energy gap between the first excited and the ground states is given in Fig. 3.4. When h_x and h_z are small, the gap is small and the system is in the antiferromagnetic phase. When h_x and/or h_z get larger, the gap increases and there is a phase transition between the antiferromagnetic and paramagnetic phases. To estimate the phase transition boundary, we use the fidelity susceptibility approach that we used in Chapter 2. At the phase boundary, the fidelity susceptibility has its maximum. It means that there is a sharp qualitative change in the ground state.

To calculate the fidelity susceptibility, we use the following method described in [62, 113]. For a given magnetic field h (h_x or h_z), we find the overlap² between the ground state at that field and ground state of the perturbed Hamiltonian (new field is $h_x + \delta$ or $h_z + \delta$

²In Chapter 2, we use the overlap squared to calculate the fidelity susceptibility. Both can be used, fidelity susceptibility differs only by a factor of 2 due to binomial expansion.

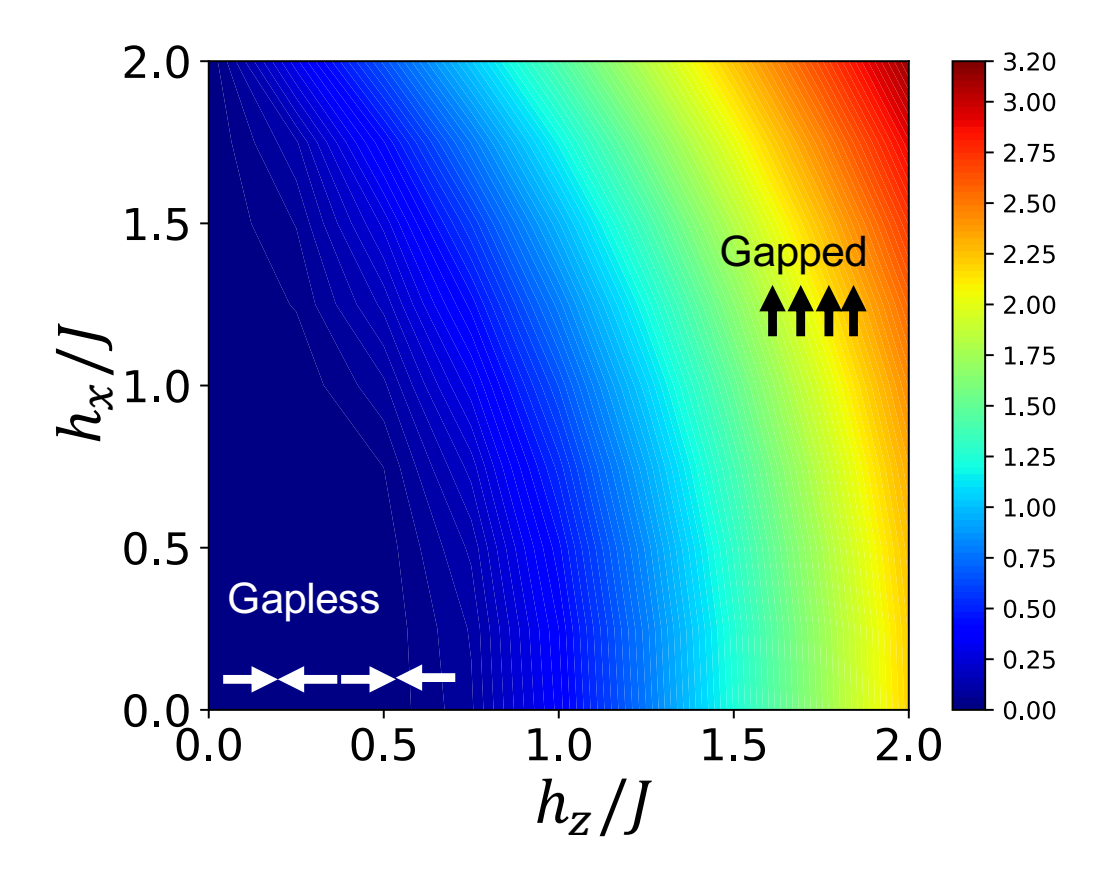


Figure 3.4: Phase diagram for the antiferromagnetic open chain given in Fig. 3.3. Energy gap between the first excited state and the ground state is plotted. Colorbar unit is arbitrary. $J = 500 \mathrm{MHz}$.

depending on the initial choice of direction) 3 :

$$F(h,\delta) = |\langle \psi(h) | \psi(h+\delta) \rangle|. \tag{3.9}$$

Then, fidelity susceptibility for the given magnetic field is

$$\chi(h) = 2(1 - F(h, \delta))/\delta^{2}. \tag{3.10}$$

For the given value of h_x , we calculate $\chi(h_x)$ for many h_z . z-field which makes $\chi(h_x)$ maximum corresponds to the z-component of the phase transition point (h_x, h_z) . The fidelity susceptibility for $h_x/J = 0.56$ as a function of h_z is given in Fig. 3.6. For the clean

³Different than the the fidelity susceptibility analysis in Chapter 2, we consider the ground state here because we are interested in the quantum phase transition.

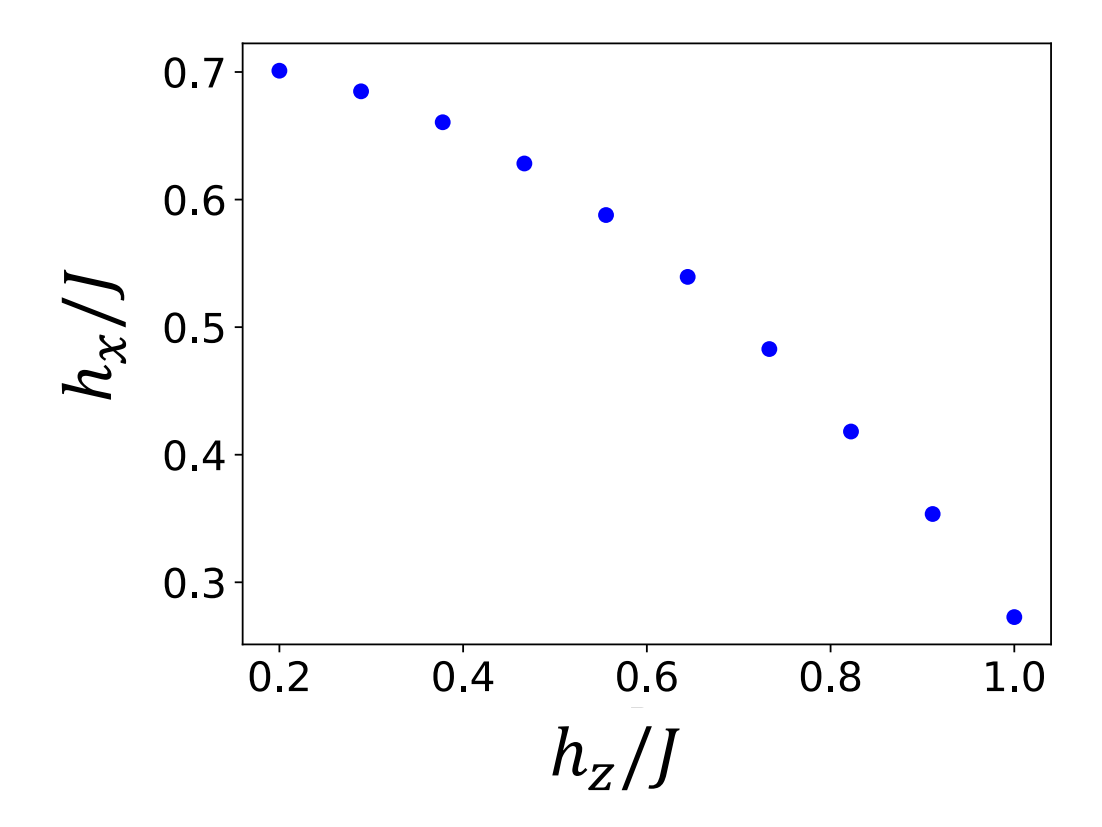


Figure 3.5: Phase diagram boundary estimated using fidelity susceptibility.

system, the phase transition point for $h_x = 0.56J$ is at $h_z \sim 0.6J$. Following this approach and varying both h_x and h_z , we get the phase boundary in Fig. 3.7.

In Fig. 3.6(a), we also provide three instances of disorder together with the clean system results. The disorder is on x-field only. For a given x-field on site l, $h_l^x = h^x + d_l$, where the disorder d_l is selected from random uniform distribution in [-0.1J, 0.1J]. We calculate h_z for each $\chi(h_l^x)$. The distribution of h_z for 10^4 instances of disorder is provided in Fig. 3.6(b). The narrowness of the width is a sign that the phase diagram is robust against disorder.⁴

⁴This point is under investigation.

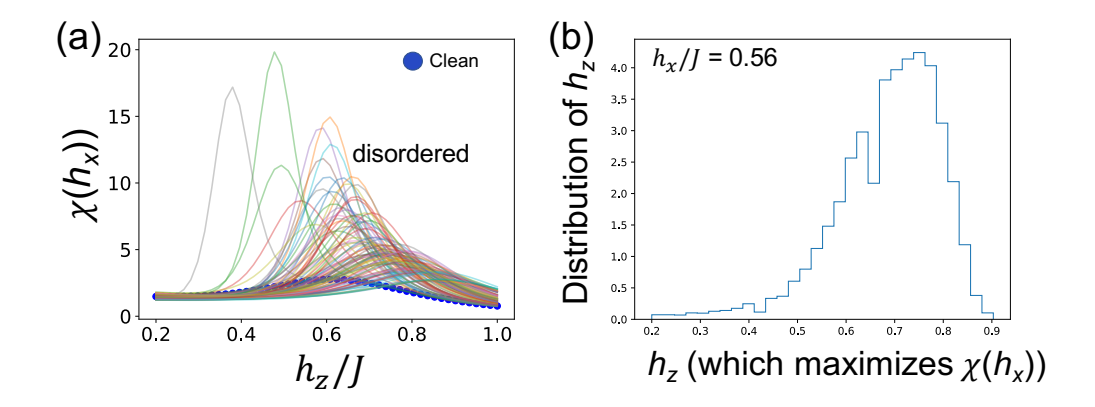


Figure 3.6: (a) Fidelity susceptibility $\chi(h_x = 0.56J)$ as a function of h_z for clean and disordered fluxonium chain. 100 instances of disordered $\chi(h_x = 0.56J)$ are plotted, the distribution with more realizations are shown in (b). x-field consists of uniform and disordered terms. J = 500 MHz. (b) Distribution of h_z maximizing $\chi(h_x = 0.56J)$ for a sample of 10^4 disordered x-field.

3.4 Edge states

We briefly discuss a step towards what can be done to identify edge states in the topological regime of the transverse field model in longitudinal field. Transverse field Ising model can be mapped onto the Kitaev model (1-d p-wave superconductor) [146]. Topology is not protected in the former but Ising simulations can be used to understand Majorana physics [65]. As explained above, short Ising chain simulations are already in the realm of fluxonium qubit systems.

The transverse field in the transverse Ising Hamiltonian corresponds to the site energy in the Kitaev Hamiltonian. If the magnetization is larger at a site it means that the particle is more probable to be in that site.⁵ The magnetization is defined as:

$$\langle \sigma_z^i \rangle = \langle \psi | \sigma_z^i | \psi \rangle, \tag{3.11}$$

where i is the site number from 0 to 7 (there are 8 spins in the chain) and ψ is a given energy eigenstate. In Fig. 3.7, we plot magnetization as a function of site for the three lowest-lying states for a system in the gapless antiferromagnetic phase ($h_x = h_z = 0.56J$). By "Ground

 $^{^{5}}$ In Chapter 2, we studied the total spin of the system in z direction. Here, we study the magnetization as a function of site.

State 1, 2", we emphasize that the ground state is degenerate when $h_x = h_z = 0$. When the fields are switched on, the ground state is not degenerate anymore and there is a gap between the two lowest-lying states but the phase transition occurs when the fields reach high enough values. We can see that for this system in the gapless phase, magnetization is largest at the edges. An edge state is a state localized at one of the edges only, not localized at both edges. Magnetization is useful to check where a given state is likely to belong to but it is inconclusive to find exactly where the wave function is localized. We also study correlation functions to identify the localization properties of the states.

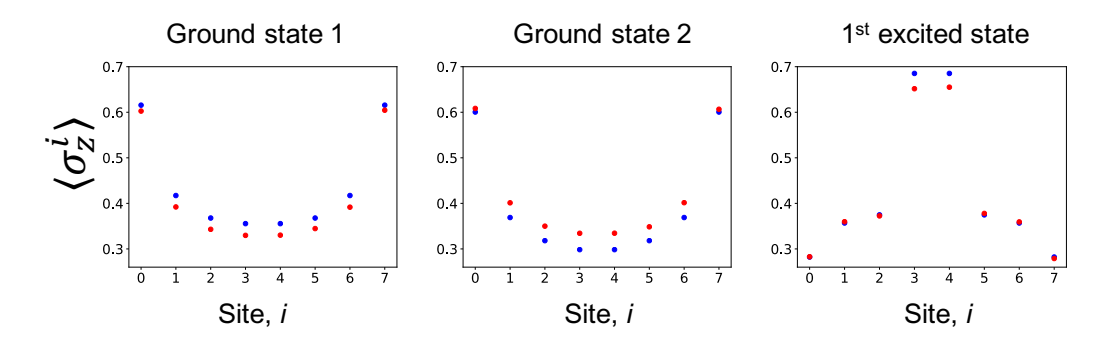


Figure 3.7: Magnetization as a function of site for a gapless point in Fig. 3.4. $h_x = h_z = 0.56J$. x-field has disorder. Results for clean (blue) and disordered (red) chains are provided.

3.5 Propagating Excitations

We finally discuss another experimentally accessible idea using magnetization to quantify the difference between responses of qubits to a spin flip. We consider the open fluxonium chain of 8 qubits as in Fig. 3.3 with ferromagnetic transverse field Ising Hamiltonian:

$$H = -J \sum_{l=1}^{L-1} \sigma_x^{(l)} \sigma_x^{(l+1)} + \sum_{l=1}^{L} h_l^z \sigma_z^{(l)}.$$
 (3.12)

When $\{h^z\}=0$, the ground state of this Hamiltonian is the equal superposition of $|\uparrow\uparrow\uparrow\uparrow\uparrow...\rangle$ and $|\downarrow\downarrow\downarrow\downarrow...\rangle$: $|\psi_{gs}\rangle_{\pm}=\frac{(|\uparrow\uparrow\uparrow\uparrow...\rangle\pm|\downarrow\downarrow\downarrow\downarrow...\rangle)}{\sqrt{2}}$, where $|\uparrow\rangle=|0\rangle$ and $|\downarrow\rangle=|1\rangle$. We consider an initial state $|\downarrow\uparrow\uparrow\uparrow\uparrow...\rangle$ close to one of the terms which ground state is written in superposition of. The first spin is flipped from $|\uparrow\rangle$ to $|\downarrow\rangle$. The aim of the experiment is to study the

relaxation properties of the first spin and identify the responses of other qubits to this spin flip. One can use antennas for each qubit to measure the magnetization as a function of time.

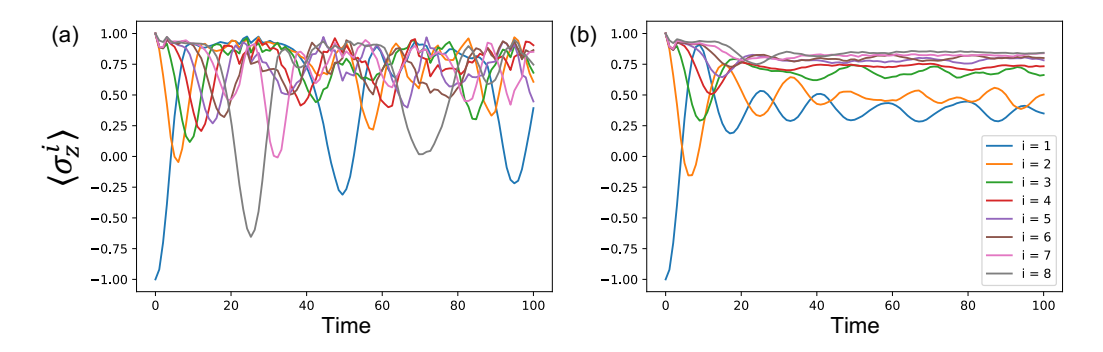


Figure 3.8: Magnetization as a function of time for (a) clean, (b) disordered systems. i is the qubit number. First qubit with i = 1 is flipped initially. Both timing and amplitudes could be used to quantify the differences between qubit responses. Time unit is 1/J.

In Fig. 3.8, we plot z-field magnetization given in Eq.(3.11) as a function of time for clean and disordered systems. For the disordered system, z-field h_z has disorder and satisfies $h_l^z = h^z + d_l$, where the uniform field $h_z/J = 2.5$ and the disorder d is selected from the random uniform distribution [-J, J]. For the clean system, $d_l = 0$.

Response of each qubit differs in timing of the revivals and oscillation amplitudes. We give the results up to Time = 100 but it is possible to identify the differences even within short time (such as between Time = 0 and 20). For the clean system, the qubits close to the first qubit has stronger dispersion and larger oscillation amplitudes in the initial stage of the drive. After Time = 20, the first qubit and the ones in the other edge of the chain has larger amplitudes than the others due to wave scattering from the edge. When the disorder is turned on, the first qubit relaxes quickly and has short periods for the remaining oscillations after the initial oscillation. The wave does not propagate through the whole system. Only closer qubits have large oscillations but the magnetizations of distant qubits change only slightly up to a degree for which they are distinguishable. The disorder in this setup can be used to dampen the oscillations and to help us clearly distinguish between qubit behaviors.

3.6 Conclusions

We discussed the Ising simulations that can be performed using fluxonium qubits. With its long coherence time at and away from sweet spot, strong coupling exceeding the qubit transition energy and anharmonicity, fluxonium qubits are promising quantum information systems to study strongly interacting clean and disordered systems. Using fidelity susceptibility, we studied the phase transitions in transverse Ising chain in a longitudinal field in the parameter regime of fluxonium qubits. It is possible to explore different regimes by properly tuning the fluxonium chain. We showed that by magnetization measurements one can take a step towards identifying the edge states and one can identify characteristics of propagating excitations.

Chapter 4

Steering random spin systems to speed up the quantum adiabatic algorithm

4.1 Introduction

There is a furious race underway to construct the first practical quantum computer. To complement this, there is a large research effort to broaden the class of problems that can be attacked by these machines. A very promising direction is optimization problems. One of the leading candidate methods for solving such problems on a quantum computer is the quantum adiabatic algorithm (QAA) [20], in which the ground state of a simple quantum system is slowly transformed into the solution of the optimization problem. There have been extensive studies of the QAA on classical computers [22] and open-system quantum annealing devices intended to solve similar problems have been constructed [147, 148, 149]. The QAA exploits the adiabatic theorem and uses the fact that the ground state of appropriate quantum Hamiltonians correspond to difficult classical optimization problems, for which the standard classical search algorithms are inefficient due to the complicated landscape for the cost function [150, 41]. The difficulty in demonstrating the QAA is the presence

of small energy gaps that can lead to generalized Landau-Zener-Stueckelberg-Majorana (LZSM) tunneling [151, 152, 153, 154]. Once the tunneling occurs, the system leaves the instantaneous ground state, probably for good, and the algorithm breaks down.

In spin models, we may look more closely at the degrees of freedom that produce the dangerous avoided crossings. The classic LZSM problem can be thought of as a single spin-1/2 particle in a time-dependent magnetic field that reverses the spin direction. This is the local single-particle case. In the other limit, we may imagine a crossing of two levels whose energies are very close, but whose spatial configurations differ by the rearrangement of many spins, perhaps well-separated in space. This is the non-local case. Both contribute to unwanted tunneling.

In this chapter, we propose a modification of the QAA that largely eliminates local LZSM tunneling. This modification requires accurate control of individual qubits that was demonstrated recently in various systems, including trapped ions [155], Rydberg atoms [156] and superconducting qubits [157]. In the conventional annealing protocol, the system is prepared in a strong field along the x-direction without interaction, then the field is slowly changed to the final field and the interaction is turned on. During this process, a time-dependent gauge term causes transitions between the instantaneous eigenstates of the Hamiltonian. This term is proportional to the Berry curvature [158, 159, 160, 161, 162] and its effect was recently investigated in superconducting devices with a single qubit [163] and interacting qubits [164]. We demonstrate that with the proper compensation of this topological term, qubits acquire protection against excitation processes, increasing the probability for the system to remain in the ground state even for short annealing times. This approach may also point the way toward more general improvements of quantum adiabatic algorithms.

4.2 Method

The Hamiltonian in our approach is defined on the time interval $0 \le t \le t_a$, where t_a is the annealing time and it has the form:

$$H_{qaa}(t/t_a) = f_i(t/t_a)H_i + f_f(t/t_a)H_f + H_s(t).$$
(4.1)

Here H_i and H_f are time-independent Hamiltonians that represent a simple problem and a difficult optimization problem, respectively. The scalar functions f_i and f_f satisfy the boundary conditions: $f_i(0) = f_f(1) = 1$ and $f_i(1) = f_f(0) = 0$. However, we adjust these functions rather than choosing the customary linear-in-time forms. H_s is the steering term and key to our approach. The idea of adding an additional term to the Hamiltonian is not new and has been used to convert a stoquastic Hamiltonian to a non-stoquastic Hamiltonian [48, 165], while modifications to the annealing schedule have been used to add quantum fluctuations [18]. It has also been used in the method of shortcuts to adiabaticity and quantum critical points [166, 167, 168, 169, 170, 171, 172, 173, 174]. Our method is to make a local approximation to the exact formula for the counterdiabatic driving Hamiltonian, defined in the following paragraph.

We construct H_s using a result from adiabatic population transfer theory and counterdiabatic driving [175, 45]. If a time-dependent Hamiltonian H_0 has instantaneous eigenstates $|n(t)\rangle$ such that $H_0(t)|n(t)\rangle = E_n(t)|n(t)\rangle$, then we can define the steering Hamiltonian as

$$H_1(t) = i\hbar \sum_{m=2}^{2^L} \frac{|m\rangle\langle m|\partial_t H_0|1\rangle\langle 1|}{E_1 - E_m} + \text{(h.c.)}.$$
 (4.2)

The modified Hamiltonian $H(t) = H_0(t) + H_1(t)$ drives the ground state $|1\rangle$ of H_0 without any transitions. If the initial state at t = 0 is the ground state of H_0 , then the solution of the time-dependent Schrödinger equation at t_a is the ground state of H_0 . We could take $H_0 = f_i(t/t_a)H_i + f_f(t/t_a)H_f$ and $H_s = H_1$, and this would yield the solution of the optimization problem with certainty, but unfortunately the computation of H_1 is not efficient. Instead, we propose a local approximation to H_1 . We note that for single spin-1/2

particle at site k with Hamiltonian $H_0^{(k)}(t) = B^{(k)}(t) \cdot \sigma^{(k)}/2$ the steering term is

$$H_{0,s}^{(k)}(t) = \frac{1}{2B^{(k)}(t)^2} \left[\boldsymbol{B^{(k)}}(t) \times \partial_t \boldsymbol{B^{(k)}}(t) \right] \cdot \boldsymbol{\sigma^{(k)}}$$
(4.3)

and we may correct for an arbitrary random magnetic field on an array of spins by summing over k.

To illustrate our method we choose the one-dimensional random-field Ising model (RFIM) on a ring of L spins:

$$H_f = \sum_{k=1}^{L} h_k \sigma_z^{(k)} + J \sum_{k=1}^{L} \sigma_z^{(k)} \sigma_z^{(k+1)}$$
(4.4)

with periodic boundary conditions understood. The h_k are chosen uniformly from the interval [-1,1]. The width of the disorder distribution sets the energy scale. The initial Hamiltonian is chosen as usual to be a uniform transverse magnetic field

$$H_i = h_0 \sum_{k=1}^{L} \sigma_x^{(k)}. \tag{4.5}$$

In the calculations below we take $h_0 = 10$.

The RFIM at J=0 has the simple solution $\langle \sigma_z^k \rangle = -h_k/|h_k|$, while the $J \to \infty$ limit is an antiferromagnet. At small J, $J << h_{av}$ (h_{av} , average random field, $\sim 1/2$ in this chapter), the ground state has just a few spins that deviate from the J=0 solution at sites k where $|h_k|$ happens to be small. The spin at site k feels a time-dependent effective field with a z-component given by the sum of h_k and $J[\langle \sigma_z^{(k-1)}(t) \rangle + \langle \sigma_z^{(k+1)}(t) \rangle]$, where $\langle \sigma_z^{(k\pm1)}(t) \rangle$ are the time-dependent expectation values of the z-components of the neighboring spins. When the magnitude of the total effective field (including the x-component) becomes small, the gap becomes small and the QAA can fail. This is the type of failure that our local approximation for H_1 should be able to fix. At larger J values, (J of order 1) there will be larger clusters of spins that deviate from the J=0 solution. This will create situations where there are small energy gaps separating states that differ by many spin flips. Our single-spin approximation for the steering term is then not expected to work, and more sophisticated approximations are required. We will later present a cluster method that is a step in this direction.

It is clear that the steering method is applicable in principle to any model that includes a random field. Our choice of the RFIM is motivated by the facts that it has a relatively small number of parameters, is simple to simulate numerically, and the statistical properties of the final Hamiltonian of Eq. (4.4) have been well studied. By the standards of the field, the one-dimensional RFIM is fairly simple but it has nevertheless served as a common testbed for the QAA.

Notice that H_i and H_f are both stoquastic [176] but the introduction of H_s makes the Hamiltonian non-stoquastic. This is somewhat similar to a previous study, [48], but our motivation for introducing the additional term is quite different.

We choose $f_i(t) = \cos^2(\pi \tau/2)$ and $f_f(t) = \sin^2(\pi \tau/2)$, where $\tau \equiv t/t_a$. The initial behavior of f_f and the final behavior of f_i are quadratic; this is chosen so that $H_s(t=0) = H_s(t=t_a) = 0$ and the derivatives provide slow start and stop. These choices, together with Eq. (4.3), give

$$H_s(\tau) = \sum_{k=1}^{L} \frac{-h_0 h_k \pi \sin(\pi \tau)}{4 t_a [h_0^2 \cos^4(\pi \tau/2) + h_k^2 \sin^4(\pi \tau/2)]} \sigma_y^{(k)}.$$
 (4.6)

Since t_a can be small, the size of the steering term can be large. Of course an arbitrarily large H_s is unphysical. Ultimately, the interesting parameter range for the QAA is when t_a is large. In this case the steering term is typically small compared to the other terms in the Hamiltonian.

4.3 Results

With these definitions we solve the time dependent Schrödinger equation for H_{qaa} numerically [85, 177]. For comparison purposes it is useful to solve the same instance of the problem with the above definition of H_s ("with steering") and setting $H_s = 0$ ("without steering"). We also define the success probability, i.e., the probability to be in the ground state at the end of the evolution, as $P_1 = |\langle 1|\psi(t=t_a)\rangle|^2$.

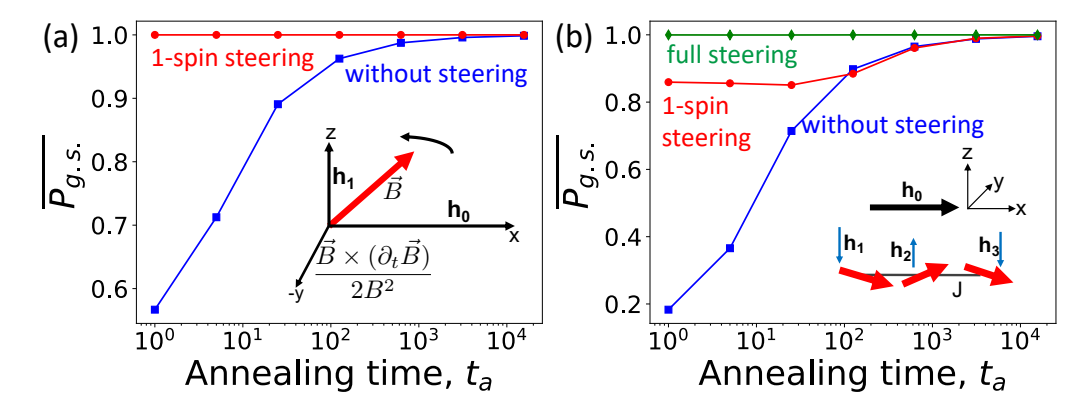


Figure 4.1: (Color online) Average ground-state probability as a function of the annealing time t_a . The h_k are chosen uniformly from the interval [-W, W], where W = 1. All energy variables are measured in units of W, and time variables are measured in units of \hbar/W throughout the chapter. (a) L = 1. In the inset, the red magnetic field vector rotates from x to z direction in the standard quantum annealing process. The steering field applied in the -y direction suppresses transitions to the excited states. (b) L = 3, J = 0.1. The green diamond curve is the result of the application of Eq. (4.2), the exact Berry formula. The inset shows the sketch of the open chain of 3 spins considered here.

Small Systems

In Fig. 4.1 we report results for the systems with L=1 and L=3 using Eq. (4.2). In Fig. 4.1(a), we show the fundamental effect of steering. The system finds the ground state independent of the annealing time to within our numerical accuracy for this case, which is to say 1 part in 10^9 . Fig. 4.1(b), we compare the 1-spin steering with the case of no steering applied and with the "full steering". Full steering is the exact application of Eq. (4.2). It is the basis of the cluster approach that we present in the later part of the chapter.

Comparison to Other Methods

Small systems are only of interest for illustration purposes. Practical applications require larger systems. Because of the need to average over disorder realizations, we are limited to $L \leq 12$. A sketch of the system we consider is shown in the inset of Fig. 4.2(a) for L = 10. In Fig. 4.2(a), we present how the average ground-state probability changes as a function of the annealing time for a weak interaction (J = 0.1). Especially for short annealing times, the probability of achieving the ground state and thereby successfully solving the

optimization problem is quite small without steering. It is greatly enhanced by steering for short and long annealing times. In Fig. 4.2(a) we also show as dashed lines the result of a "naive" classical algorithm in which we choose the solution of the non-interacting system: $\langle \sigma_z^k \rangle = -h_k/|h_k|$. This solution is obtained by choosing J=0 in the problem Hamiltonian H_f , Eq. (4.2), and applying the steering, Eq. (4.6). The steered QAA outperforms this algorithm in the range $t_a > 10^2$ for J=0.1.

When the interaction becomes stronger, the low-lying states have a more entangled character; they cannot be written, even approximately, as product states. Thus the local steering algorithm becomes ineffective. This is shown for a short annealing time $t_a = 1$ in Fig. 4.2(b), where the average ground-state probability is plotted as a function of J. We see a crossover at $J \sim 1$ from a regime in which steering is effective to a regime where it is not. It is interesting that the addition of H_s does not improve the QAA for $J \geq 2$, and can even degrade the performance. We attribute this to the fact that the system, for part of its evolution, is trying to find the ground state of a Hamiltonian $H_i + H_f + H_s$ that is somewhat further from the problem Hamiltonian compared to $H_i + H_f$. The "recovery" of the steered Hamiltonian at larger J is presumably due to the ground state being a locally perturbed antiferromagnetic state, close once more to a product state. For such a short annealing time, of course both the steered QAA and the standard QAA perform relatively poorly. This can be seen by plotting the results for the naive algorithm, shown by the dashed lines. Obviously, the results of this algorithm are independent of t_a . Its success is similar to that of the steered QAA for J < 1. For larger values of J, the naive algorithm performs poorly, as expected from the fact that it ignores interactions.

In Fig. 4.2(c) the annealing time is longer: $t_a = 100$. We see similar trends overall steering becomes ineffective at larger J. This plot does show clearly that there are definite differences between the standard QAA and the steered QAA at intermediate annealing times.

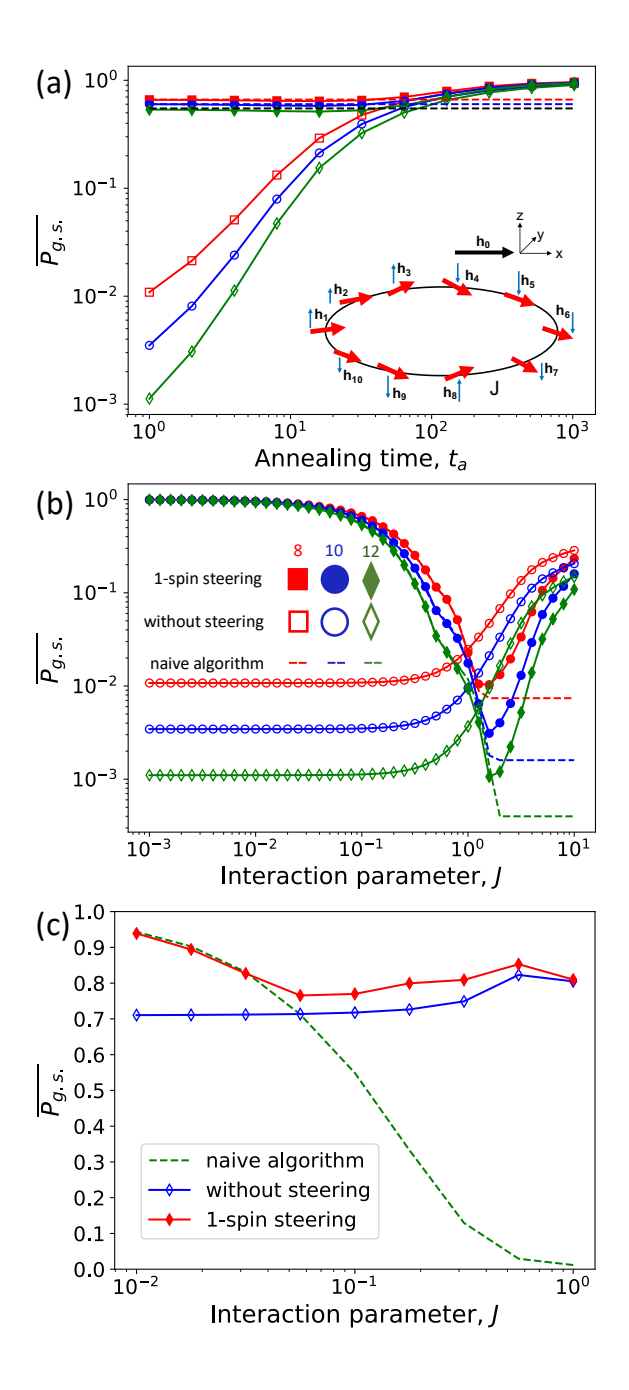


Figure 4.2: (Color online) (a) Average ground-state probability as a function of the annealing time t_a . L=8 (square), L=10 (circle), L=12 (diamond) compared for J=0.1. (b) Average ground-state probability as a function of the interaction parameter J for a short annealing time $t_a=1$. The red (upper), blue (middle) and green (lower) dashed lines show the naive algorithm results for L=8,10,12, respectively. (c) Average ground-state probability as a function of the interaction parameter J for a longer annealing time $t_a=100$.

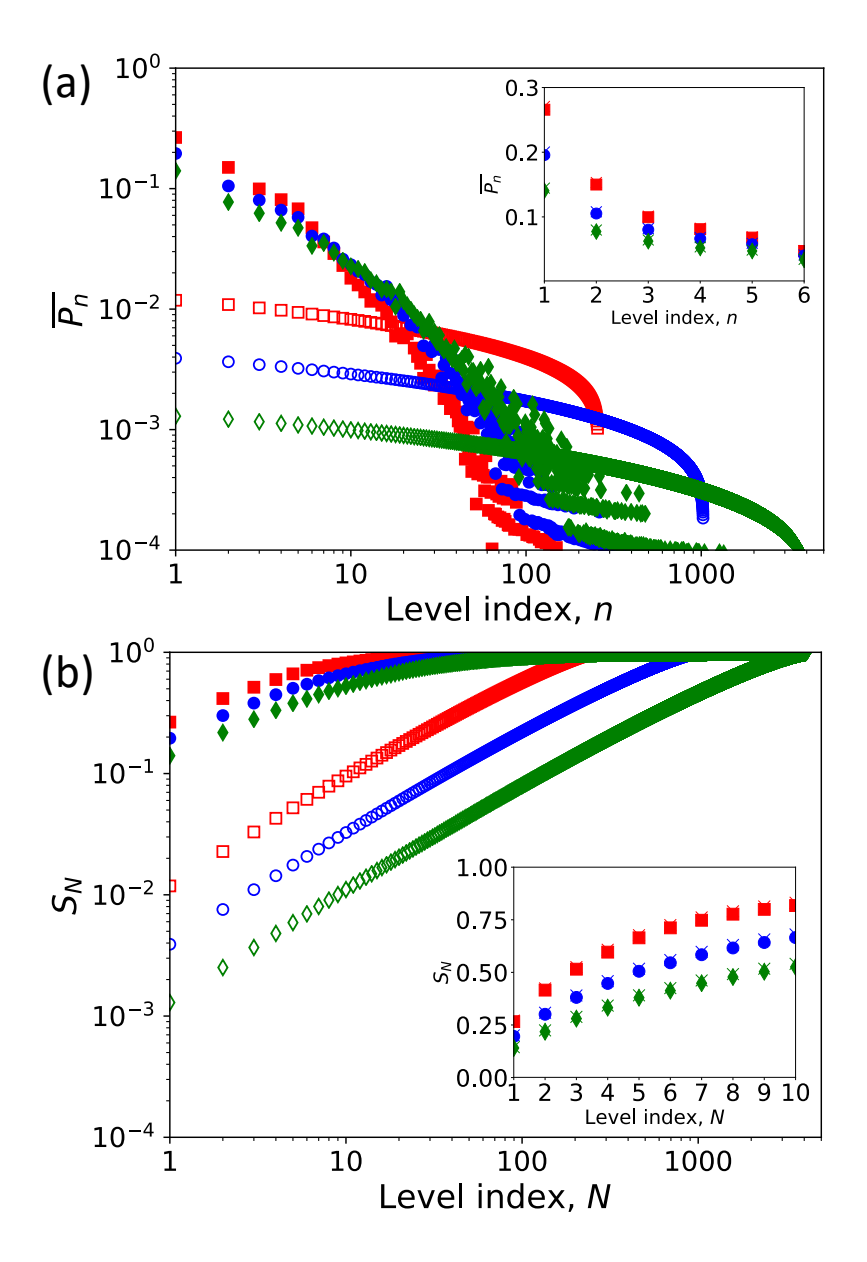


Figure 4.3: (Color online) Same markers are used in this figure as in Figs. 4.2(a) and (b) for the standard QAA and the steered QAA. For the naive algorithm, red (upper), blue (middle) and green (lower) "x" markers are used in the insets for L=8,10,12, respectively. In the insets, the naive algorithm is compared with the steered QAA. $t_a=1,\ J=0.3$. Several system sizes are shown. (a) The probability distribution over all final eigenstates $|n(t_a)\rangle$ as a function of the level index n, computed by comparing the results of the QAA to an exact calculation. $P_n=|\langle \psi(t_a)|n(t_a)\rangle|^2$. The effect of steering is to squeeze the width of the probability distribution by two orders of magnitude and in the direction of the ground state. (b) Cumulative probability distribution. $S_N=\sum_{n=1}^N \overline{P_n}$. With the steered algorithm, the chance to find one of the low-lying states is significantly enhanced.

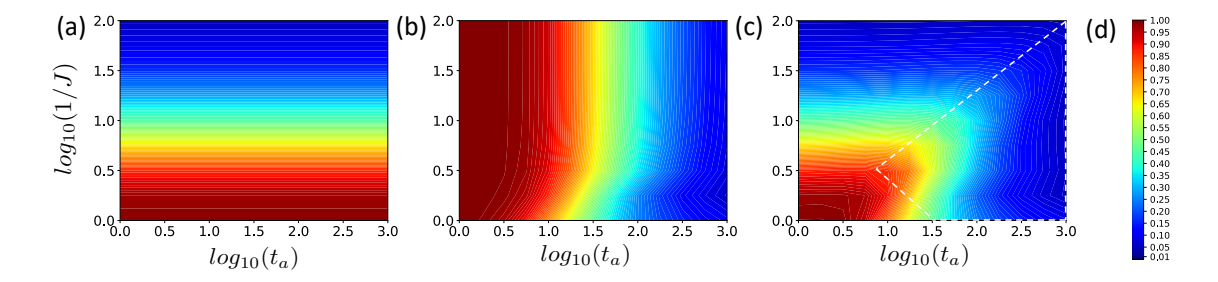


Figure 4.4: (Color online) Average infidelity as a function of 1/J and t_a . L=12. Plots for (a) the naive algorithm, (b) the standard QAA, and (c) the steered QAA. In the region covered by the white dashed lines, the steered QAA gives higher fidelity than the other two algorithms. (d) The colorbar shows the infidelity values.

Distribution over Low-lying States

Next, we consider how the introduction of a moderate interaction (J=0.3) modifies the final distribution of the probability over all states both with and without steering, using a short annealing time $t_a=1$. Recall that L is the number of spins and the total number of levels is 2^L , which is the size of the classical problem. In Fig. 4.3 we plot probabilities P_n of all states, defined as $P_n=|\langle \psi(t_a)|n(t_a)\rangle|^2$, and the cumulative probability, defined as $S_N=\sum\limits_{n=1}^N\overline{P_n}$. The states $|n(t_a)\rangle$ are eigenstates of H_f and they are arranged in order of increasing energy. $|\psi(t_a)\rangle$ is the final state computed in the QAA. This is done for several system sizes. Of course to obtain these data we must also solve the problem exactly for $|n(t_a)\rangle$, so this limits the size of systems we can treat. Again we average over 10^4 realizations of the disorder for each curve shown.

The effect of steering on the QAA is very dramatic. Roughly speaking, for all system sizes the width of the probability distribution is squeezed down towards the ground state by two orders of magnitude by steering the QAA. The chance of making a serious error and ending in a state with high index is greatly reduced. If we think of the system as diffusing from one instantaneous eigenstate to another during the course of a computation, it seems that the effect of steering is to reduce the diffusion rate regardless of whether the system is close to the ground state or not.

Certain final states or groups of final states appear to be favored, and the groups are

somewhat different for the steered and unsteered cases. We can speculate that these states represent local energy minima. The unsteered algorithm may in fact be superior in escaping local minima that come from extended eigenstates while the steered algorithm is more effective at avoiding local minima that come from more localized eigenstates.

On the other hand, for these values of t_a and J, the advantage of the steered QAA over the naive algorithm is marginal — the data points nearly overlap. In the next subsection we investigate when the results for these two algorithms separate.

Regime of Superiority of Steered QAA over Other Methods

Figs. 1, 2 and 3 demonstrate that steering can improve the QAA substantially for $J \leq 0.3$ and $t_A \leq 10$. However, our results so far leave open the possibility that a combination of the standard QAA and the naive algorithm could give a roughly comparable performance to the steered QAA. We now show that this is not the case. In Fig. 4.4 we present contour plots of the infidelity for the naive algorithm, the unsteered QAA and the steered QAA as a function of the two key parameters t_a and J. This allows us to locate the range in which the performance of the steered QAA is superior. This is the interior of the dashed white region in Fig. 4.4(c). Since this is a log-log plot, the range of parameters inside the region is quite large.

The key point is that steering is in fact effective when the spin interacts with its neighbors. It becomes entangled with neighboring spins and its state can no longer be represented by a pure state on the surface of the Bloch sphere, but one may still define an effective field. When the magnitude of the total effective field is small, a small gap in the excitation spectrum is likely. This is obviously the dangerous case. Our results show that steering is also effective in this situation. The steered QAA is superior to the unsteered QAA in all cases. The improvement is particularly dramatic when t_a is small, but even at moderate values the improvement is substantial.

Cluster Steering

One of the advantages of the steering method is that it is susceptible to systematic improvement. The results presented so far are only those that follow from a single-particle approximation to the steering Hamiltonian. In this subsection, we present our results for a more sophisticated approximation that we call cluster steering. This is defined as follows. The spin which has minimum random field (whose direction is therefore likely to be determined by the interaction) is identified. This spin and its two neighbors are considered as a cluster. The cluster steering term is found from Eq. (4.2). In this approach, while the cluster steering is being applied to the spin trio, 1-spin steering is applied to each spin in the rest of the chain. There are 12 spins in the chain and 10^4 realizations are performed. In Fig. 4.5, the two types of the steering are compared to the case of no steering. At small J, the curves with steering coincide and, at stronger J, all curves go up. The latter happens because in this regime the spectrum becomes more regular with level repulsion. However, the steering of weak clusters helps to maintain the system in the ground state even for intermediate strengths of interaction. With the cluster approach, the ground-state probability does not drop to smaller values sharply. When J is small, the ground-state probability curve is more flat compared to the curve of 1-spin steering.

4.4 Conclusion

We demonstrate significant improvements in the QAA for random-field spin systems with relatively weak interactions. This is done by adding a term to the Hamiltonian that suppresses transitions representing local spin re-orientations. When the interactions become stronger, the low-energy eigenstates become more extended and the technique in the approximation used here becomes ineffective. In other words, the method is good for insulating phases and not for metallic phases of disordered systems. However, the steering concept itself, as represented by the correction term in Eq. (4.3), is not at all limited to local modifications of the problem. We made a cluster expansion to construct a less local form of the

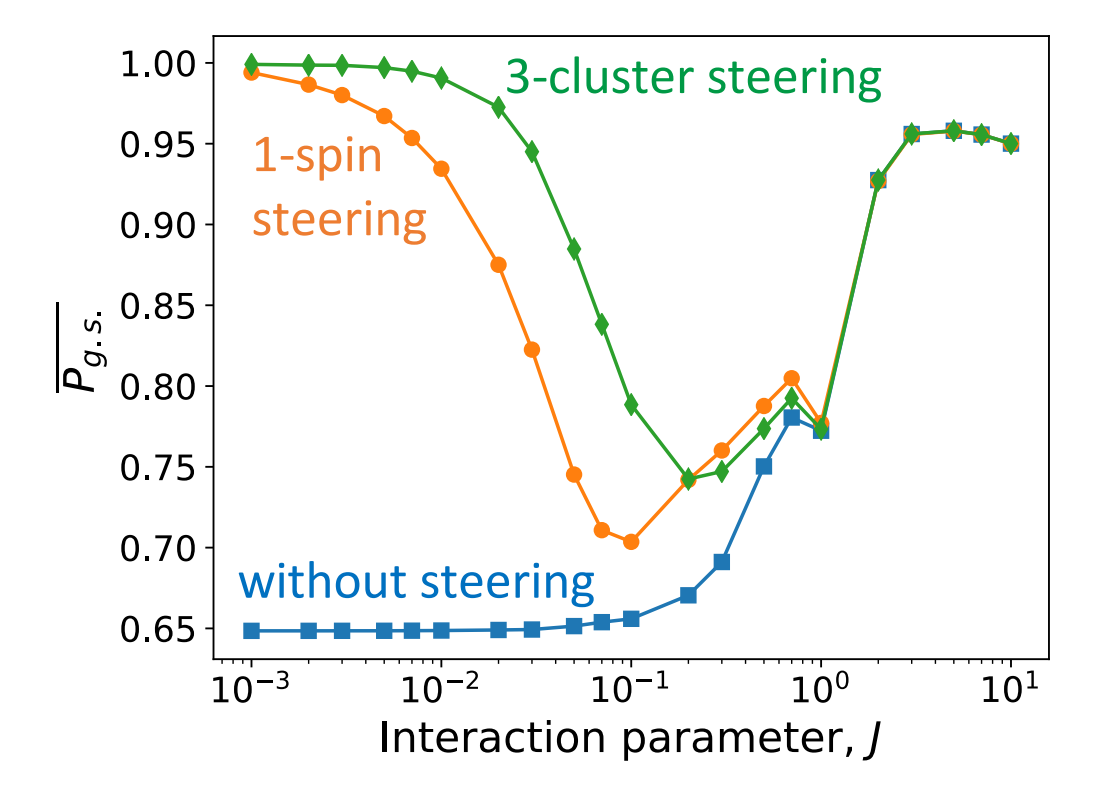


Figure 4.5: (Color online) Average ground-state probability as a function of the interaction parameter J for the QAA without steering, with 1-spin steering, and with cluster steering. Cluster steering improves the results for $J \leq 0.2$ $t_a = 128$, L = 12.

operator in Eq. (4.6). It should also be possible to work out ways of improving the steering so that it is effective in metallic phases as well.

We have not yet investigated systematically the crucial question of how the improvements in the algorithm scale with system size. The local nature of the improvements of the steering would suggest at least a constant speedup comparing to the standard annealing procedure. Of course in practical calculations even a constant speedup is very desirable, as long as the constant is big. For certain problems, we show that two orders of magnitude can be achieved.

The protocol is applied to a particular configuration of the final Hamiltonian, where both local fields and couplings between the spins are exactly determined by the corresponding classical optimization problem. To evaluate the performance of the algorithm for different problems with similar structure, we assume that the optimization problems represent an

ensemble of random Hamiltonians. The success is determined both by the quantum fidelity of the final state and by the fraction of successful solutions out of the ensemble. For t_a fixed at 1, we have the following comparisons for the standard and steered QAAs. Out of exponentially large system size 2^L with L=12, we find with probability above 99% that the system is in one of 21 low energy states when J=0.1. For J=0.3 and the same L, we find one of the 398 low energy states with probability above 99% for the QAA with 1-spin steering. For the unsteered algorithm, the corresponding values are too large — 3949 and 3929, respectively. For the QAA with 1-spin steering, the probability to find one of the lowest 1% of 2^L (with L=12) energy states is 99.7% when J=0.1. When J=0.3, the probability becomes 81%. For the unsteered algorithm, the corresponding probabilities are only 3% and 4%, respectively. Thus, by controlling 3L local fields, we are guaranteed to find one of the low energy states out of 2^L states.

We also compare the steered QAA to a naive classical algorithm that works only for weak interactions. Combining all our results shows that there is a substantial range of parameters for which the steered QAA outperforms both the standard QAA and the naive algorithm.

Part II

Multiterminal Josephson Junctions

Chapter 5

Studies of multiterminal junctions via scattering theory

5.1 3-terminal Josephson junctions with rectangular scattering region

We have seen in Chapter 3 that Josephson junctions can be used as nonlinear inductance in superconducting circuits. Now, we will turn our attention to novel platforms where the concept of conventional two-terminal junctions is generalized into general multiterminal junctions. We study quantum transport and superconducting properties of multiterminal JJ. New topological effects have been predicted theoretically [73, 178, 179, 180] and shown experimentally using multiterminal Josephson junctions (JJ) with epitaxial heterostructures [74, 75, 76]. These devices can access the physics and topology of higher dimensional phase space due to the extra parameters introduced by each added terminal. In N-terminal JJ, one current from a terminal can be eliminated due to current conservation, therefore phase-space is (N-1)-dimensional. In two-terminal junctions, the phase-space is only constituted by the phase difference between the terminals, therefore it is one-dimensional. Adding more terminals means adding more dimensions to the phase-space.

In this chapter, we study the effects of gate voltage and magnetic field on multi-terminal

Josephson junctions. The gate voltage can control interference effects via manipulating Fermi wavelength. We assume that chemical potential is uniform throughout the system.

In the following chapter, we will study junctions with nonuniform chemical potential by assuming the gate is applied only on the scattering region, which is a more realistic setup for hybridization [181]. In two-terminal junctions, one can introduce parameters other than phase difference to tune the junction to a certain regime. Magnetic field is one such parameter.

Three-terminal junctions with flux can carry the essence of multiterminal junctions which have more than two independent parameters. We study the effects of flux on the three-terminal junctions. Such a device can be used to understand the general quantum transport properties of multiterminal JJ. Flux, as well as each added terminals, can alter the trajectories of the particles and can create extra interference effects. Therefore, flux can also be considered as another independent parameter in addition to the independent phases of terminals. Energy levels and supercurrents of the device can be represented in two-dimensional phase-space and the critical current is the boundary of the two-dimensional critical current contour (CCC) formed by the currents from the two terminals whose phases are not fixed.

Magnetic field breaks time-reversal symmetry of the junctions. In two-terminal junctions, this effect is weak. In junctions with more than two terminals, it has been shown that the time-reversal symmetry can be broken even without magnetic field [182]. In this reference, the scattering region is made of material with strong spin-orbit coupling. In our study, we will not consider the spin-orbit coupling because it does not change the results qualitatively.² However, even without spin-orbit coupling but with magnetic field, it is possible to see pronounced time-reversal breaking effects of the magnetic field in junctions with more than two terminals.

We choose the scattering region as rectangular to make the lead attachments and scattering theory calculations easier. By this way, we also aim to to compare the results for the

¹We assume that gate is applied over all junction including leads.

²Symmetry class of the scattering matrices do not change.

junctions with the extra lead to the results of the conventional rectangular two-terminal junctions. We will study the junctions with arbitrary geometries in the following section.

Different geometries of JJs can be designed to study the effects of magnetic field on supercurrents. For two-terminal long wide SNS junctions, edge effects alter zeros of the critical currents [183].³ Hourglass-shaped junction is another example for junctions exhibiting geometric effects [184]. Supercurrents form vortices and vanish at large magnetic fields due to the narrow opening of a hourglass-shaped junction.

In two-terminal junctions, critical current oscillates as the absolute value of sinc function of normalized flux [185]. For multiterminal JJs, two trajectories starting from two of the leads and ending up in the third lead can interfere destructively, which results in suppression of the critical currents. Similar to the observations of Ref. [183] for two-terminal long junctions, we observe that critical current zeros are lifted in three-terminal junctions. The third junction can act as an another source of diffraction by providing extra edge effects.

We investigate how the third lead alters the critical current oscillations. In junctions with more than two terminals, it is appropriate to define the critical current as the maximal values of the contour of independent currents. In this chapter, the contour is two-dimensional for three-terminal junctions because they have two independent currents.

For junctions with more than three (N) terminals, we take the two-dimensional projections of the (N-1)-dimensional data by choosing appropriate current biases. We study the effects of gating both in the few-channel limit and in the junctions with many channels. Effective chemical potential of the junction can be varied by applying top voltage, which changes the Fermi wavelength of the junction. The junction can be considered as a network of pair of junctions. The extended/nonextended character of the Andreev bound state wave function determines the coupling between each two terminals in the junction. Depending on the coupling strength, CCCs have a certain shape and there can be transition from one shape to another by varying the chemical potential of the system. In the second section of this chapter, we study the effects of gating on the regime of the junction with more than

³Both length and width of the junctions are taken larger than the coherence length by the authors.

three terminals. We consider several geometries and compare the results.

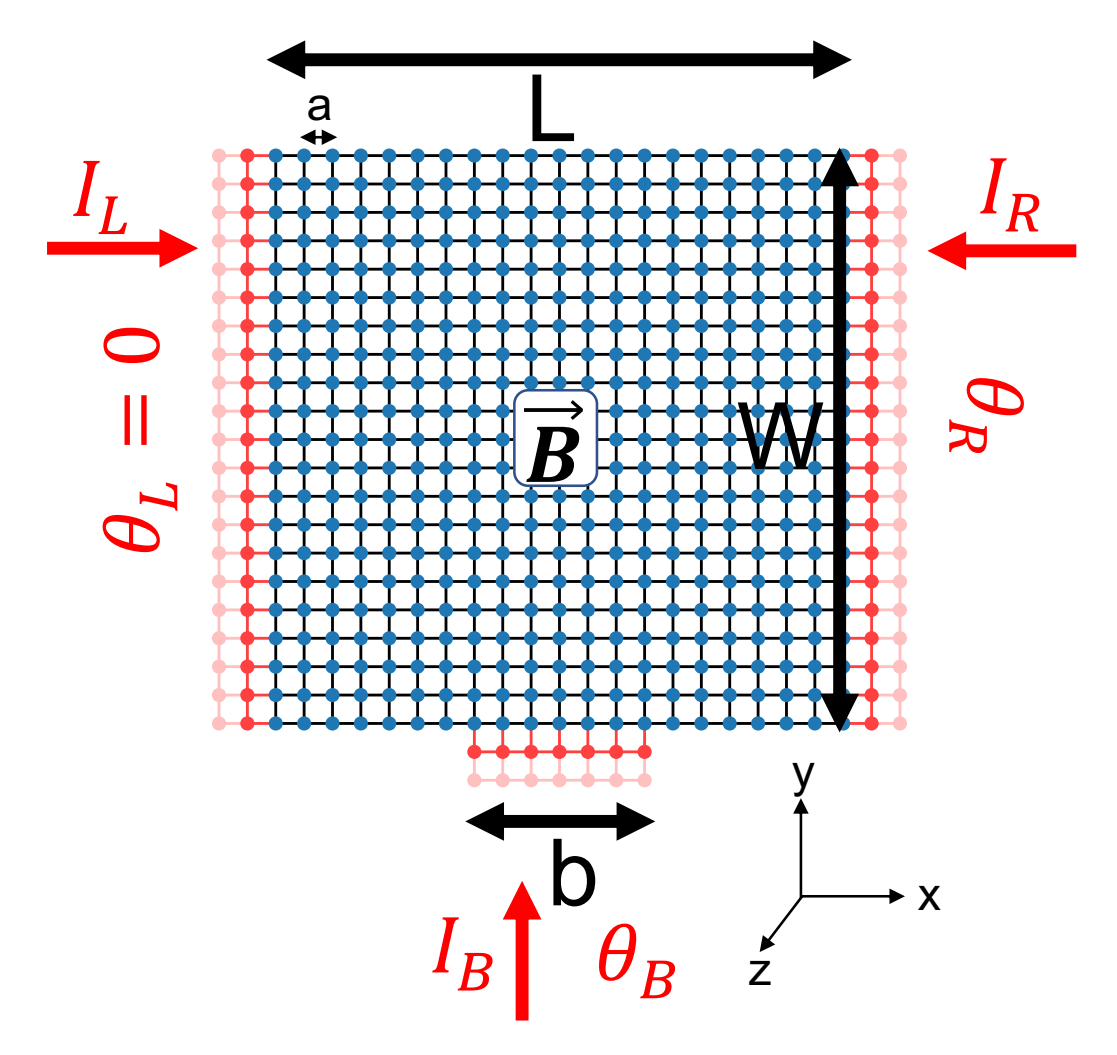


Figure 5.1: System sketch of a tight-binding lattice which has scattering region of 21-by-21 sites. Scattering sites are colored with blue and they are in between three superconducting leads, which are semi-infinitely long and colored with red. The superconducting leads are at the left, right and bottom of the scattering region. Lattice constant a=2nm throughout the chapter, L, W=20a for this sketch. L is the (horizontal) length and W is the (vertical) width of the junction. b is the width of the bottom lead and b=0 limit is the two-terminal junction. b is varied from 0 (two-terminal limit) to b. Magnetic field b is b with flux b is applied to the scattering region and it is perpendicular to the junction b plane. Each terminal has a superconducting phase: b is perpendicular to the junction b stand for left, right and bottom respectively. The lattices in this thesis are produced via Kwant.

Model

The junctions we consider have superconducting (s-wave) leads and normal metal scattering region. Normal metal is a two-dimensional electron gas (2DEG). Single-electron Hamiltonian H of the 2DEG is given by:

$$H = \frac{(\mathbf{p} - e\mathbf{A})^2}{2m} - \mu + V(\mathbf{r}),\tag{5.1}$$

where **p** is the momentum, e is the electron charge, m is the effective quasiparticle mass (we take $m = 0.03m_e$, where m_e is the electron mass), **A** is the vector potential, μ is the chemical potential. A perpendicular magnetic field (in $\pm \hat{z}$ direction) is applied to the scattering region with vector potential given in the Landau gauge $\mathbf{A} = (-By\hat{x}, 0)$.

Top gate voltage V controls the carrier density. Chemical potential is given by $\mu = \sqrt{2kn_e}$, where the electron density $n_e = 1.5 \times 10^{12}$ cm⁻². The parameters for 2DEG are based on quantum transport measurements in [186, 75].

Electron and hole excitations are described by the Bogoliubov-De Gennes equation:

$$\begin{pmatrix} H & \Delta(r) \\ \Delta^*(r) & -H \end{pmatrix} \begin{pmatrix} u \\ v \end{pmatrix} = E \begin{pmatrix} u \\ v \end{pmatrix}, \tag{5.2}$$

where u and v are the wave functions of the electron and hole respectively, E is the energy of the excitations relative to the chemical potential μ . $\Delta(r)$ is the superconducting pair potential and it is zero in the normal region. Since we consider s-wave superconductors in the terminals, $\Delta(r)$ is position-independent and its magnitude is constant. It has a finite value given by $\Delta(r) = \Delta e^{i\theta}$ in the superconductors, where θ is the phase angle of the given terminal and $\Delta = 0.18$ meV is the induced gap measured in multiterminal JJ experiments of Ref. [75]. This Δ value is close to the gap of Al film [187]. The phase of the left terminal θ_L is fixed at zero and the phases of the other two terminals are varied (see Fig. 5.1).

Our simulations are based on the tight-binding approximation of the continuum model given by Eq. (5.1). We introduced the following lattice Hamiltonian as in the Introduction chapter:

$$\sum_{\langle i,j\rangle} t_{ij} c_i^{\dagger} c_j - \mu \sum_i c_i^{\dagger} c_i. \tag{5.3}$$

To remind, t_{ij} is the hopping parameter and is inversely proportional to mass and the square of the lattice constant (horizontal or vertical distance between two consecutive sites). The hopping parameter is modified under magnetic field, as explained below. We will explain under what conditions the continuum model can be mapped onto the lattice model. A sketch of the tight-binding system is depicted in Fig. 5.1. We vary length and width of the terminals to study how the size of the three-terminal system affects supercurrents. In addition, chemical potential of the whole junction is varied around Fermi energy E_F and a perpendicular magnetic field is applied to the scattering region. The three superconducting phases for the leads are given by θ_L , θ_R and θ_B , where the subscripts L, R and B stand for left, right and bottom, respectively. Due to current conservation, one can choose one of the phases constant. We set θ_L as constant. By this way I_L is chosen as dependent current which can be found with the knowledge of I_R and I_B : $I_L = -I_R - I_B$. θ_R and θ_B are calculated with respect to θ_L , so θ_L can be chosen as zero. The phase-space of the threeterminal junction is two-dimensional and constituted by θ_R and θ_B . Length and width of the device are given by L and W, respectively. The width of the bottom terminal is shown by b. $b \to 0$ limit gives the two-terminal junction. We vary b up to L to study the effects of the third terminal width on the Andreev energies, critical currents and phase accumulation. The source code written using Kwant [81] provided by [184] calculates current for the twoterminal hourglass-shaped junction. We benefit from the code to study quantum transport properties of the multiterminal Josephson junctions.

We justify the parameter choices of the junction in Fig. 5.2. The hopping parameter t is given by

$$t = \frac{\hbar^2}{2ma^2}. ag{5.4}$$

t is inversely proportional to a^2 , so small choice of a makes t large. Tight-binding approximation gives accurate results for states that have energies less than t [188]. We choose the lattice constant $a=2\mathrm{nm}$ and effective mass m=0.03 m_e , so the hopping parameter becomes $t=318\mathrm{meV}$. Therefore, our tight-binding calculations are valid for energies less than 318meV. We vary the carrier concentration around $n_e=1.5\times10^{12}\mathrm{cm}^{-2}$, so Fermi

energy is around $E_F = (\hbar^2 2n_e \pi)/(2m) = 120 \text{meV}$. We keep it below t.

To compare the continuum model with the tight-binding model, the space-dependent term of the continuum Hamiltonian is given by⁴

$$\frac{\hbar^2(k_x^2 + k_y^2)}{2m},\tag{5.5}$$

and the same term for the tight-binding model is given by [78]:

$$2t(2 - \cos(k_x a) - \cos(k_y a)). (5.6)$$

Here, $k_x = k_y = \frac{2\pi}{\lambda_F}$. The lattice constant a = 2nm should satisfy $a << \lambda_F$ so that the tight-binding approximation gives close results to the continuum model.⁵

The continuum Hamiltonian (5.1) also includes a magnetic field term, given by the vector potential \mathbf{A} . In tight-binding model, t is modified and becomes different in x and y directions. It is transformed into its new forms t_x and t_y by the Peierls substitution [78, 81]:

$$t_{x,y} = t e^{-ie/\hbar \int \mathbf{A} \cdot d\mathbf{l}} . {(5.7)}$$

Since **A** is chosen in Landau gauge $\mathbf{A} = (-By\hat{x}, 0), t_y = t$ and

$$t_x = t e^{-ie\Phi/\hbar},\tag{5.8}$$

where Φ is the flux through the scattering region. The sinusoidal dependence of t_x to the flux is one reason of Fraunhofer patterns which we will study below.

To be able to make short junction approximation, one needs to make sure that the coherence length ξ is much bigger than system sizes L, W, b. $\xi = \hbar v_F/\Delta$. We take $\Delta = 0.18$ meV due to reason we specified above and $v_F = \frac{\hbar k}{m}$ $(k = \sqrt{2\pi n_e})$, so $\xi = 4.3$ µm. Maximum choice of L, W, b in this chapter is 600nm, which is below ξ .⁶ Other than being in short junction regime, our system is also in ballistic (mean free path >> system sizes)

⁴Single-particle Hamiltonian also depends on μ as in Eq.(5.1) but the difference between continuum model and tight-binding model does not depend on μ , which would be cancelled out.

⁵This is true as we will show below.

 $^{^6}$ Note that even though it is safe to say that the system is in short junction regime, there are some deviations from the short junction results (as we will point out below for Fraunhofer oscillations) since 600nm/ 4.3 µm is not negligible.

and clean regimes (mean free path $> \xi$). Mean free path is inversely proportional to the square of the disorder strength [189]. Here we consider zero disorder, so mean free path can be taken as infinite.

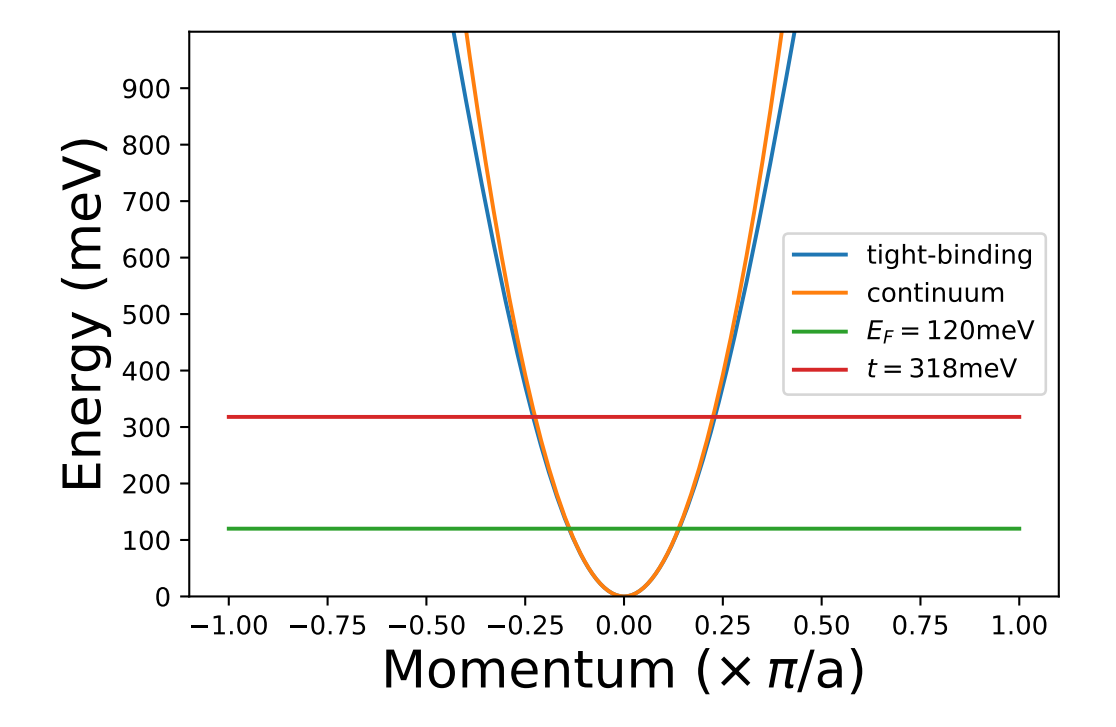


Figure 5.2: Energy as a function of momentum in the Brillouin zone. Tight-binding approximation and continuum results are compared. Tight-binding approximation gives very close results comparing to the continuum model when energy levels of the system are smaller than $t=\frac{\hbar^2}{2ma^2}$ (hopping parameter), where m is the effective mass and a is the lattice constant. We choose $a=2nm,\ m=0.03m_e$ and therefore t=318meV. We vary chemical potential, μ , around $E_F=120meV$ and below t.

Derivation of Andreev energy levels and supercurrent

As mentioned in the Introduction chapter, the supercurrent is produced via Andreev reflection. Incoming electron from a superconducting lead with energy less than superconducting pair potential Δ entering the scattering region reflects back as a hole after Andreev reflection from the opposite side of the scattering region (a boundary between the scattering region and another lead) and a Cooper pair of electrons is created in the superconducting lead. The reflected hole travels back in the same trajectory and reaches to the boundary where it first enters the scattering region. This time it reflects back as electron. The superposition of electron and hole forms purely evanescent Andreev bound state, which does not have any propagating modes outside the scattering region.⁷ In multiterminal junctions, the total acquired phase is a mixture of phases from different terminals. We use the scattering theory to find ABS energies and supercurrents in multiterminal Josephson junctions.

We follow Ref. [182] to write down the eigenvalue problem for the scattering matrix using the bound state condition. The eigenvalues correspond to Andreev energy levels. We calculate the supercurrent from the Andreev energy levels as explained in [184].

We give the sketch which summarizes the ABS condition in Fig. 5.3. $\Psi_{in} = (\Psi_{in}^e, \Psi_{in}^h)$ is the incoming electron-hole wave written in the basis of the incoming superconducting lead modes. Ψ_{in}^e and Ψ_{in}^h describe the incident electron and hole wave functions, respectively. After the wave scatters through the normal region, its wave function becomes $s_N \Psi_{in}$, where s_N is the scattering matrix for the normal scattering region:

$$s_N(E) = \begin{bmatrix} s(E) & 0\\ 0 & s^*(-E). \end{bmatrix}$$

$$\tag{5.9}$$

 s_N is a unitary matrix because its blocks are unitary due to current conservation. s (S-matrix) can be written as its reflection and transmission coefficients. The size of s gives the total number of channels in the junction. If the junction is short, s is energy-independent $s(E) \approx s(-E) \approx s(0) \equiv s$.

After normal scattering, the reflected wave from the NS boundary bounces back as $s_A s_N \Psi_{in}$. s_A represents Andreev reflection matrix and it is given as

$$s_A(E) = \alpha(E) \begin{bmatrix} 0 & r_A^* \\ r_A & 0 \end{bmatrix}, \tag{5.10}$$

where $\alpha = \sqrt{1 - E^2/\Delta^2} + iE/\Delta$ is found from boundary conditions for the waves at NS

⁷Energy of electron and hole tracing the closed trajectory inside the scattering region does not change during the Andreev or specular reflection [190].

boundary. For *n*-terminal junction, r_A is given as:

$$r_{A} = \begin{bmatrix} i1_{n_{0}} & 0 & 0 & 0 & 0\\ 0 & ie^{-i\phi_{1}}1_{n_{1}} & 0 & 0 & 0\\ 0 & 0 & ie^{-i\phi_{2}}1_{n_{2}} & 0 & 0\\ 0 & 0 & \dots & \dots & \dots\\ 0 & 0 & 0 & 0 & ie^{-i\phi_{n}}1_{n_{n}} \end{bmatrix},$$
 (5.11)

where n_i are the number of channels and ϕ_i are phases for each terminal. One of the phases can be fixed as $\phi_0 = 0$. Total number of channels $\sum_i n_i$ equals to the size of s.

After normal region scattering and Andreev reflection, the wave function becomes $\Psi_{out} = s_A(E) s_N(E) \Psi_{in}$. Andreev bound state condition is given $\Psi_{out} = \Psi_{in}$ [79]. Ψ_{out} is now the incoming electron-hole wave for another normal scattering and Andreev reflection. This cycle continues on and meanwhile supercurrent is produced after each Andreev reflection. We reach the following equation:

$$s_A(E) s_N(E) \Psi_{in} = \Psi_{in}. \tag{5.12}$$

This condition holds true assuming that magnetic field does not penetrate into the superconducting leads.

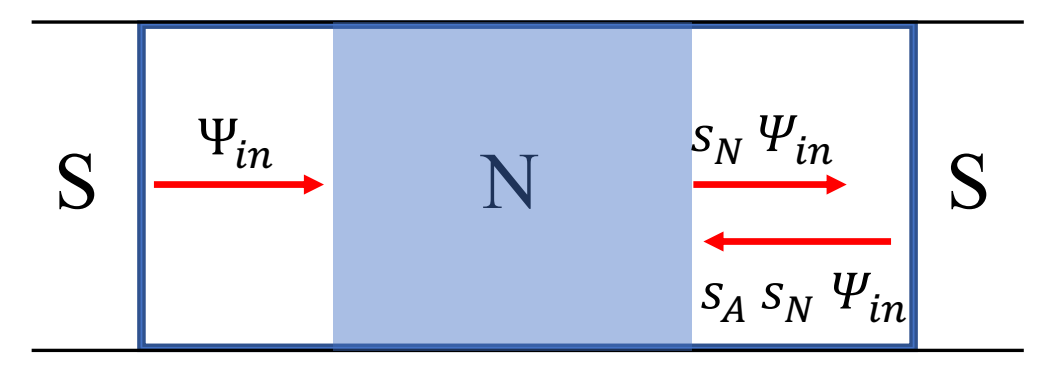


Figure 5.3: ABS condition: $\Psi_{in} = \Psi_{out} = s_A(E) s_N(E) \Psi_{in}$.

Using (5.12), the following eigenproblem for α is formed:

$$\begin{bmatrix} s^{\dagger} & 0 \\ 0 & s^T \end{bmatrix} \begin{bmatrix} 0 & r_A^* \\ r_A & 0 \end{bmatrix} \Psi_{in} = \alpha \Psi_{in}. \tag{5.13}$$

The eigenvalues with positive and real α correspond to the physical solutions. These are the levels with energies below the gap Δ . After finding α , one can map the solution to the Andreev levels E [182]. Due to electron-hole symmetry, energy levels are degenerate. E has the same positive and negative solutions. Positive ones give the Andreev levels we are looking for.

Supercurrents can be calculated by squaring Eq. 5.13 [184]:

$$A^{\dagger}A\Psi_{in}^{e} = \frac{E^2}{\Delta^2}\Psi_{in}^{e},\tag{5.14}$$

where $A \equiv \frac{1}{2}(r_A s - s^T r_A)$. To calculate the supercurrent in the lead with phase ϕ , one needs to take derivative of the energies with respect to ϕ :

$$\frac{dE}{d\phi} = \frac{\Delta^2}{2} \frac{1}{E} \left\langle \Psi_{in}^e \middle| \frac{d(A^{\dagger}A)}{d\phi} \middle| \Psi_{in}^e \right\rangle \tag{5.15}$$

Then, we get the supercurrent for zero temperature

$$I = -\frac{2e}{\hbar} \sum \frac{dE}{d\phi},\tag{5.16}$$

where E is the positive energies found from Eq. 5.13.

Fraunhofer oscillations in multiterminal junctions

When flux = 0, shape of the CCC does not change with the chemical potential μ but the CCC area changes. Chemical potential controls the number of channels in the system. Number of channels and therefore supercurrent in a terminal can be estimated by calculating how many Fermi wavelength λ_F can fit into the normal-superconductor boundary. Critical current and number of channels are proportional to $1/\lambda_F$. Chemical potential is given by:

$$\mu = \frac{\hbar^2 k_F^2}{2m},\tag{5.17}$$

where k_F is the Fermi wavevector. $k_F = 2\pi/\lambda_F$, so critical current is proportional to $\sqrt{\mu}$ (Fig. 5.4). Area of the CCC is proportional to the multiplication of critical currents I_R and I_B , which is $\propto \mu$. The result displayed in Fig. 5.5 verifies this statement. Fig. 5.4 and Fig. 5.5 can be considered as sanity checks of our code.

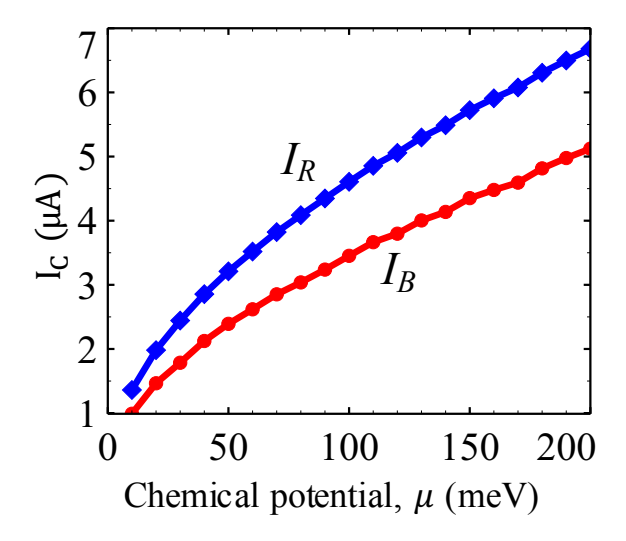


Figure 5.4: (Color online) Critical currents at the right lead (I_R) and the bottom lead (I_B) as a function of chemical potential (μ) . Flux = 0. L = W = b = 600nm. Currents have to be multiplied by 1/2 due to electron-hole symmetry. The factor is not considered in Eq. 5.14 while calculating energies. The factor has to be present for the other unnormalized ground state energies and currents of this chapter.

In a two-terminal junction with transmission T, Andreev bound state (ABS) energy of a single electron-hole trajectory is given by [77]:

$$E = \Delta\sqrt{1 - T\,\sin^2(\theta/2)},\tag{5.18}$$

where θ is the superconducting phase difference between junctions when flux is zero in the scattering region.⁸ When the flux is nonzero, there is extra path-dependent magnetic phase ξ and the phase difference is modified as $\theta' = \theta - \xi$, where ξ given by:

$$\xi = \frac{2e}{\hbar} \int_{S_1}^{S_2} \mathbf{A} \cdot d\mathbf{l}. \tag{5.19}$$

Each ABS trajectory acquires a phase depending on the geometry of the path and the superconducting phase difference between terminals.

To find the current, ABS energy (5.18) can be varied with respect to phase. We assume that the junction transmission is perfect, therefore T can be taken as 1. Using the fundamental relation $\delta I = (-2e/\hbar)dE/d\phi$ between bound state energy and supercurrent, one

 $^{^8}T$ corresponds to the transmission eigenvalue of S-matrix.

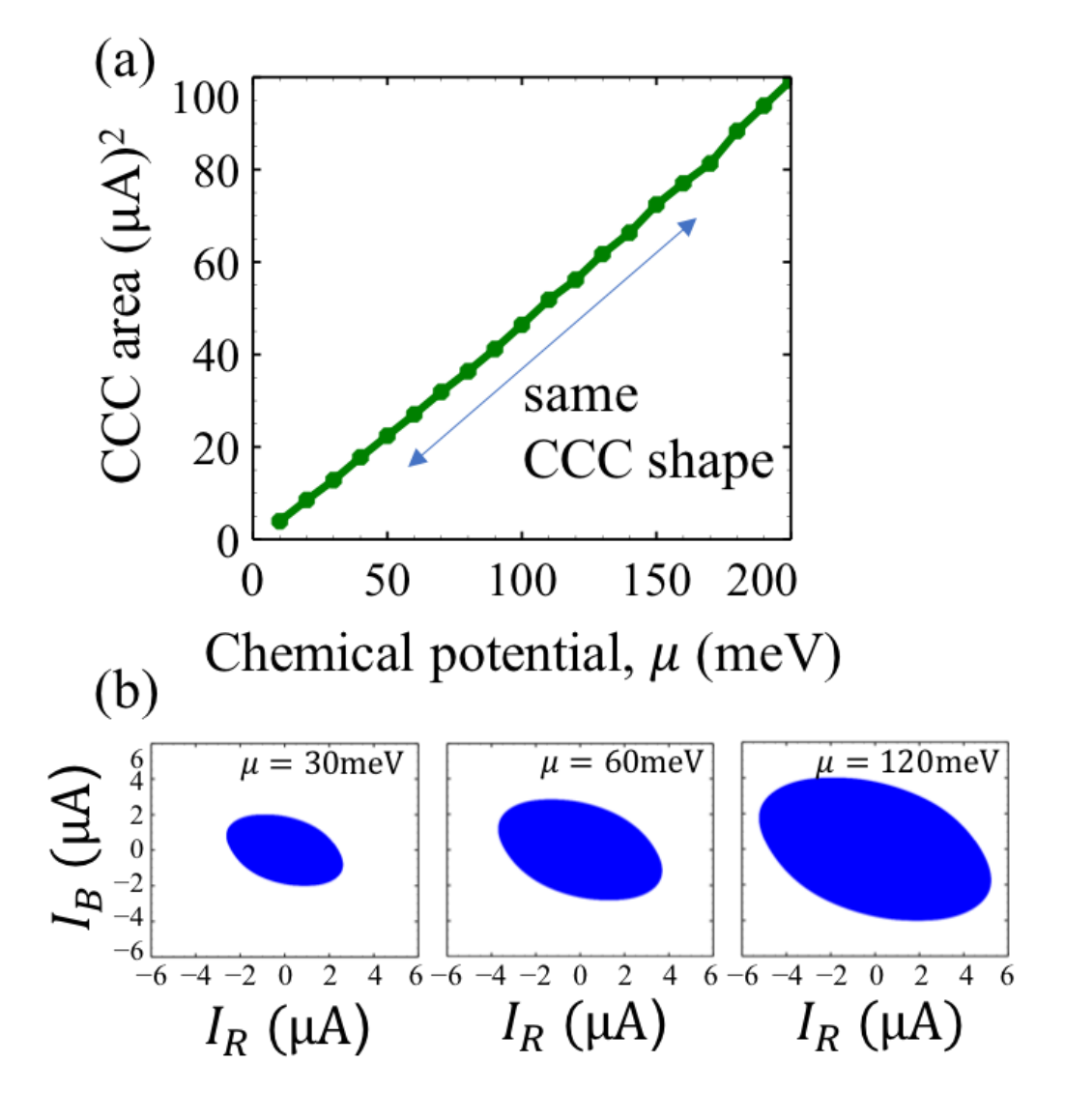


Figure 5.5: (Color online) (a) Area of CCC as a function of chemical potential (μ) . Flux = 0. L = W = b = 600nm. (b) Current scatter plots for $\mu = 30, 60, 120 \text{meV}$.

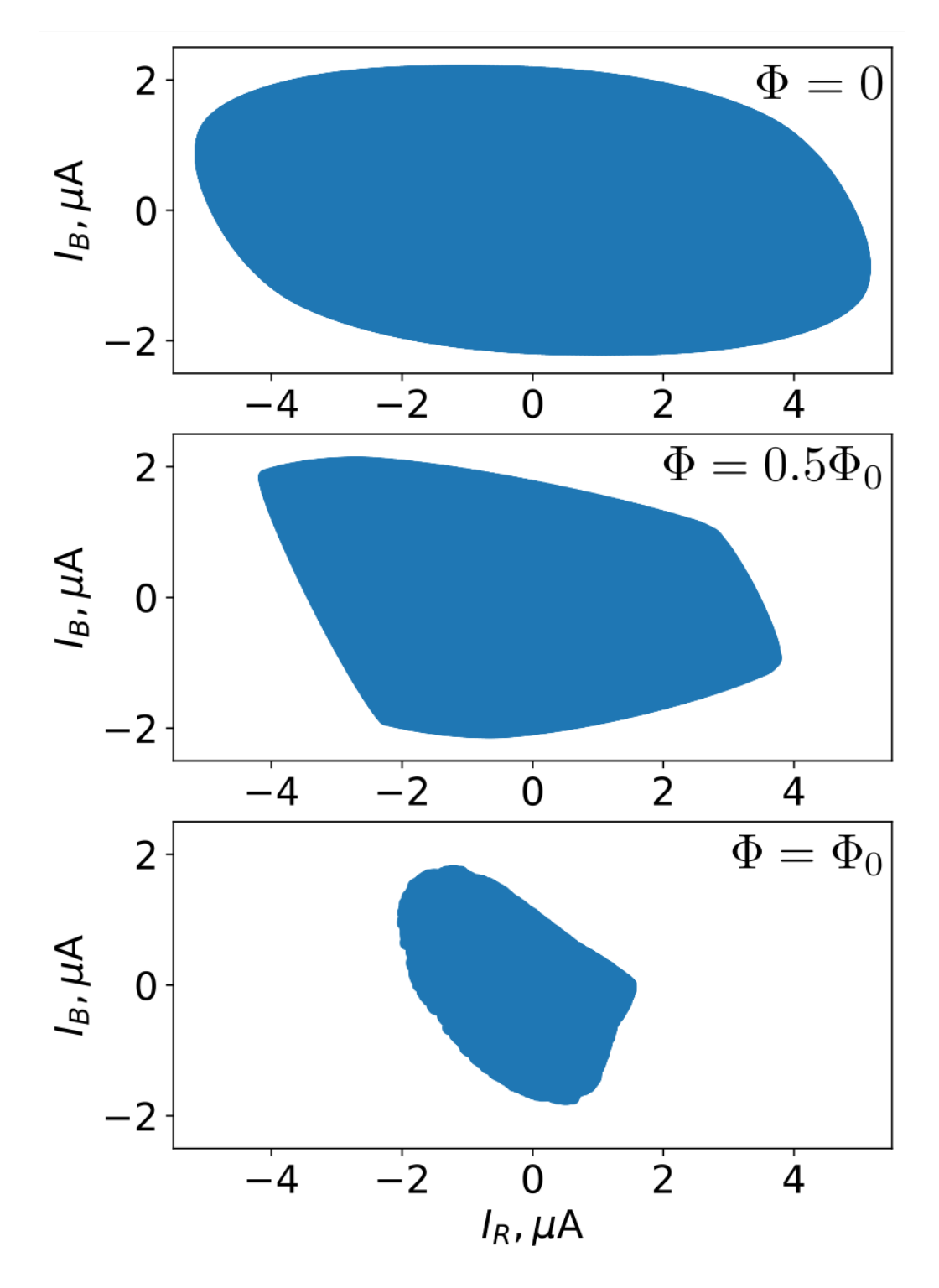


Figure 5.6: Critical current contour (CCC) scatter plots. Flux = 0, 0.5, 1 Φ_0 , where Φ_0 is the flux quantum. $\mu = 120 \text{meV}$, W = 600 nm, L = b = 300 nm.

can find the supercurrent due to a single trajectory as a function of phases:

$$\delta I = \frac{e\Delta}{\hbar} \sin(\delta(\theta) - \xi/2). \tag{5.20}$$

To find the total supercurrent, one needs to consider all positive energies E_p below the superconducting gap Δ : $I = \sum_{E_p} (-2e/\hbar) dE_p/d\phi$. In the presence of magnetic field, quantum interference between trajectories of two junctions creates Fraunhofer oscillations. The critical current is modulated according to the following formula when a perpendicular magnetic field is applied on the scattering region [185]:

$$I(\Phi) = I(0)|\sin(\pi\Phi/\Phi_0)/(\pi\Phi/\Phi_0)|, \tag{5.21}$$

where Φ is the magnetic flux in the scattering region and Φ_0 is the magnetic quantum flux. $\Phi = A.B$, where A = W.L is the area of the scattering region and B is the strength of perpendicular magnetic field applied to the scattering region. Eq. (5.21) is analogous to the single-slit diffraction in optics and is a result of sinusoidal current-phase relation given by Eq. (5.20) [191]. $I(\Phi) = 0$ when Φ is equal to the integer multiples of Φ_0 .

When the magnetic field is turned on, magnetic phase given by Eq.(5.19) mixes with the superconducting phases in the leads and deforms the ground state energy landscape given in Figs.5.8(d, e, f) for several flux values. As a result, amplitude of the ground state energy decreases (Fig. 5.7), additional maxima and minima develop, the minimum shifts from the origin (0,0) and the inversion symmetry $(\theta_R, \theta_B) \rightarrow (-\theta_R, -\theta_B)$ is absent in the energy landscape. These changes in energy landscape alters the behavior of the supercurrent under flux.

Each supercurrent I_R and I_B can be calculated as a function of superconducting phases θ_R and θ_B , which are varied between $-\pi$ and π . We make scatter plots of (I_R, I_B) . The two supercurrents are limited by the boundary of the scatter plots, which we call critical current contour (CCC) following the nomenclature of [75]. Fig. 5.6 shows the CCC for different flux values. For zero flux, the CCC is similar to a parallelogram, which means

⁹In two-terminal junctions with perfect transmission, the DC Josephson effect creates sinusoidal currentphase relation.

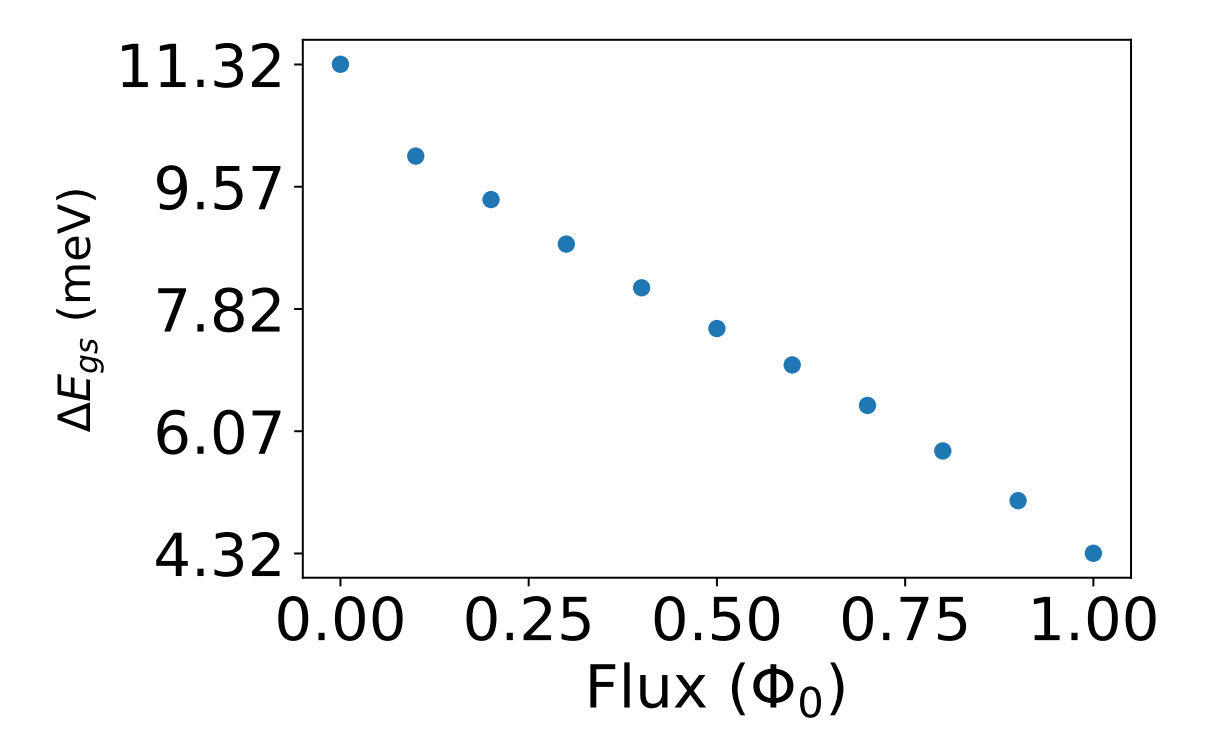


Figure 5.7: $\Delta E_{gs} = \max(E_{gs})$ - $\min(E_{gs})$ as a function of flux. Unit of flux is Φ_0 .

that the interactions between the terminals are not significant. The CCC area decreases and the shape of the CCC becomes peculiar with the increasing flux. This is a signature of a transition from an uncoupled network of JJ to a multiterminal JJ, where the terminals are coupled and strongly interacting. Moreover, time-reversal symmetry is broken due to magnetic field. If we chose our junction symmetric, then we would see that the CCC at zero flux would be symmetric with respect to the axes in addition to being inversion symmetric with respect to the origin. We will study symmetric four-terminal junctions in the next chapter. Here, the CCC is formed by the right and bottom currents. The right and bottom leads are not symmetric. We can understand this fact by simply switching right and bottom leads: There is another lead (left) across from the right lead but there is no lead across from bottom lead. This asymmetry of the system makes the parallelogram tilted.

To study the effect of magnetic field on critical points, we compare the CCC, ground state energy landscape and Hessian contours in Fig.5.8. The system parameters are W=L=b=60nm and $\mu=20\text{meV}$. These parameters make the computational cost lower

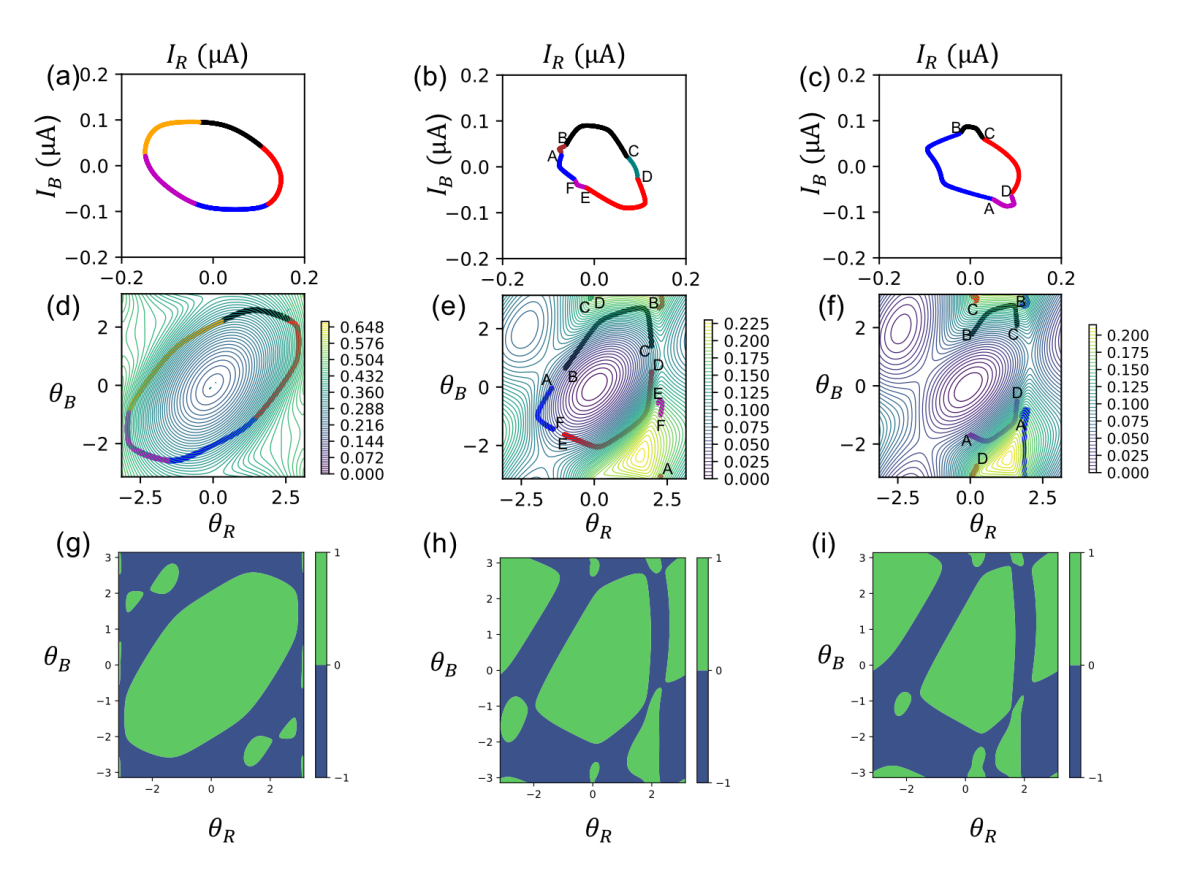


Figure 5.8: (a, b, c) CCC for flux 0, 1.2 Φ_0 and 1.5 Φ_0 , respectively. (d, e, f) GS energy contours for the flux values in the same order. Phases corresponding to the CCCs are given as differently colored clusters. Same colors and letters are used for CCCs. (g, h, i) Hessian of the energy as a function of phases. Boundary points satisfying Hessian close to zero are critical points which include CCC points. CCC is the maximal envelope to the boundary Hessian points. W = L = b = 60nm, $\mu = 20$ meV.

because number of channels are not high. Large number of channels create many phase clusters and current-current scatter plots have to be dense in order to identify the boundary appropriately.

The determinant of the Hessian matrix is used to identify the critical points of multivariate function. Our aim is to find the critical currents. We can identify the critical current by investigating the energy landscape using Hessian. Hessian matrix of the ground state energy is given as:

$$H = \begin{bmatrix} \partial^2 E_{gs} / \partial \theta_R^2 & \partial^2 E_{gs} / \partial \theta_R \partial \theta_B \\ \partial^2 E_{gs} / \partial \theta_B \partial \theta_R & \partial^2 E_{gs} / \partial \theta_B^2 \end{bmatrix}, \tag{5.22}$$

Given that $I = 2e/\hbar \partial_{\theta_i} E_{gs}$ for a lead with phase θ_i , we can write the Hessian matrix as a function of first derivatives of the supercurrents:

$$H = (\hbar/(2e))^2 \begin{bmatrix} \partial I_R/\partial \theta_R & \partial I_R/\partial \theta_B \\ \partial I_B/\partial \theta_R & \partial I_B/\partial \theta_B \end{bmatrix}, \tag{5.23}$$

Critical currents satisfy $\partial I_R/\partial\theta_R = \partial I_R/\partial\theta_B = \partial I_B/\partial\theta_R = \partial I_B/\partial\theta_B = 0$. This means that the determinant of the Hessian is zero for critical points. Therefore, CCC is the maximal envelope to the critical points. We use the word "critical" from the calculus definition. A critical point has derivative zero in all directions by definition. So, boundaries of scatter plots are actually critical points, which was considered in the experiment we get our motivation from [75]. Points for det(Hessian) = 0 is a larger set which includes the critical points. We directly calculate the critical points using the boundary of scatter points. In the near future, we will identify the stable regions inside the current-current scatter plots by stable point analysis for free energy, which will be useful to understand the nature of sharp points even more.

In Fig.5.8 (a, b, c), we plot CCCs.¹⁰ CCCs are the boundaries of the current-current scatter plots. By coloring clusters differently, we can check how the given shape in CCC manifests itself on energy landscapes given in Fig.5.8 (d, e, f). On energy landscapes, we provide the phases which correspond to the CCC points. When flux = 0 (a, d, e), the energy landscape is a single cluster without sharp corners. For flux = $1.2\Phi_0$ (b, e, h), sharp corners appear and they form separate clusters on energy landscape. We provide letters to be able to easily match which cluster is detached from where. For flux = $1.2\Phi_0$, there are several detached clusters on energy landscape but the big shape which is mostly formed by blue, black and red clusters around the minimum energy is still preserved. The reason is that the sharp little clusters are small for this flux value. When flux is increased and becomes $1.5\Phi_0$ (c, f, i), each sharp cluster gets larger and the shape formed by the phases on energy landscape has distinct clusters mostly away from the zero energy.¹¹ By forming

¹⁰To get the scatter plots, I used homogeneous sampling and also benefited from the Adaptive Python package [192] that uses machine learning sampling techniques. I also used alpha-shape techniques (such as Ref. [193] and MATLAB function *boundary* [194]) to get the boundaries of scatter plots (i.e. CCCs).

¹¹Normally, ground state energy is negative but here we set the minimum energy to zero.

sharp clusters with increasing flux, the area of CCC shrinks.

In Figs.5.8(g, h, i), we provide the Hessian contours. Green represents positive and blue represents negative values for the determinant of the Hessian. Comparing Hessian contours with the phase-energy contours in Figs.5.8(d, e, f), we can see that the CCC phases lie at the Hessian boundaries, where the determinant of the Hessian is zero. As we explained above, Hessian boundaries include the critical points.

If we plot all Hessian boundaries on the current-current scatter plots on Figs.5.8(a, b, c), we will see that the CCC is the maximal envelope of them. The sharp corners in CCC correspond to the different Hessian boundaries which are located in a separate region of the phase plane. To illustrate, let us consider the blue cluster shown by letters A-B in Figs.5.8(c) and (f). This part is detached from left side of the zero energy between magenta and black clusters and it is the boundary of a Hessian cluster as can be identified in Fig.5.8(i).

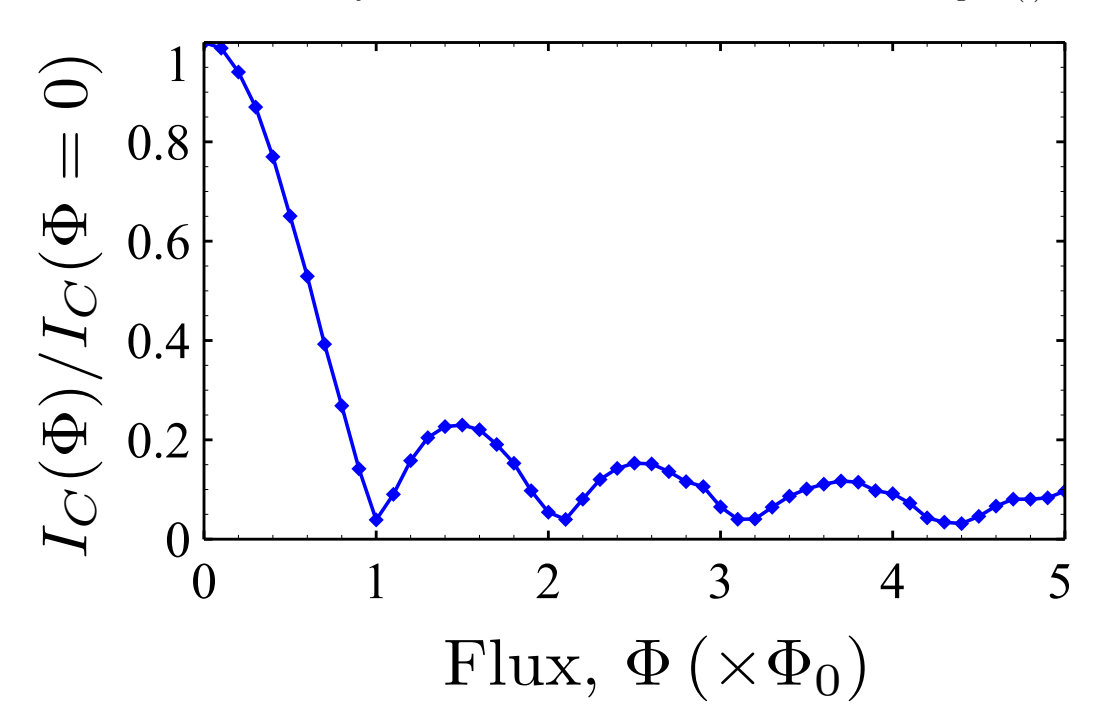


Figure 5.9: Normalized critical current as a function of flux for two-terminal junction (b = 0). $\mu = 120 meV \ W = 600 nm, \ L = 60 nm$.

Critical current has Fraunhofer-like oscillatory behavior in two-terminal JJs as given by Eq. (5.21). We provide critical current of a two terminal junction as a function of flux in

Fig. 5.9. The junction is short and wide (has aspect ratio W/L = 10) with W = 600nm and L = 60nm. The first minimum appears near Flux = Φ_0 . The minima are not zeroes as predicted by Eq. (5.21) because W/ξ (ξ is coherence length as calculated above) ratio is not negligible. Due to the same reason, the minima at larger flux values do not appear near integer multiples of Φ_0 and are lifted towards larger values.

For multiterminal JJs, separate critical currents (only I_R or only I_B for the three-terminal junction here) are not enough to understand the behavior of overall supercurrent flow in the junction. To understand the current correlations between terminals and their behavior under flux, one has to know the area (two-dimensional info for three-terminal junction) of CCC along with the critical currents, which are only the elliptical radii (one-dimensional info) of the CCC. We show that the CCC area of three-terminal junctions also exhibits oscillatory behavior similar to the critical current in two-terminal JJs. The oscillation amplitudes depend on the geometry of the junction, in particular the width of the third terminal.

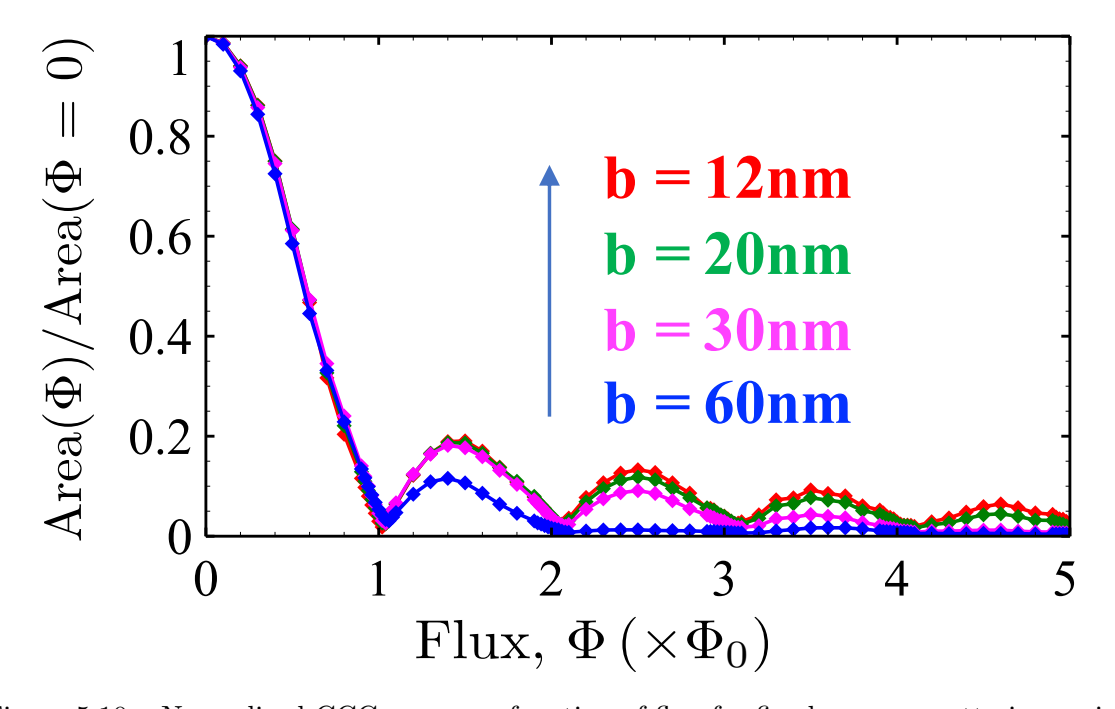


Figure 5.10: Normalized CCC area as a function of flux for fixed narrow scattering region (W = 600nm, L = 60nm) and various width b of the bottom lead. $\mu = 120meV$. The arrow shows the color order of amplitude height.

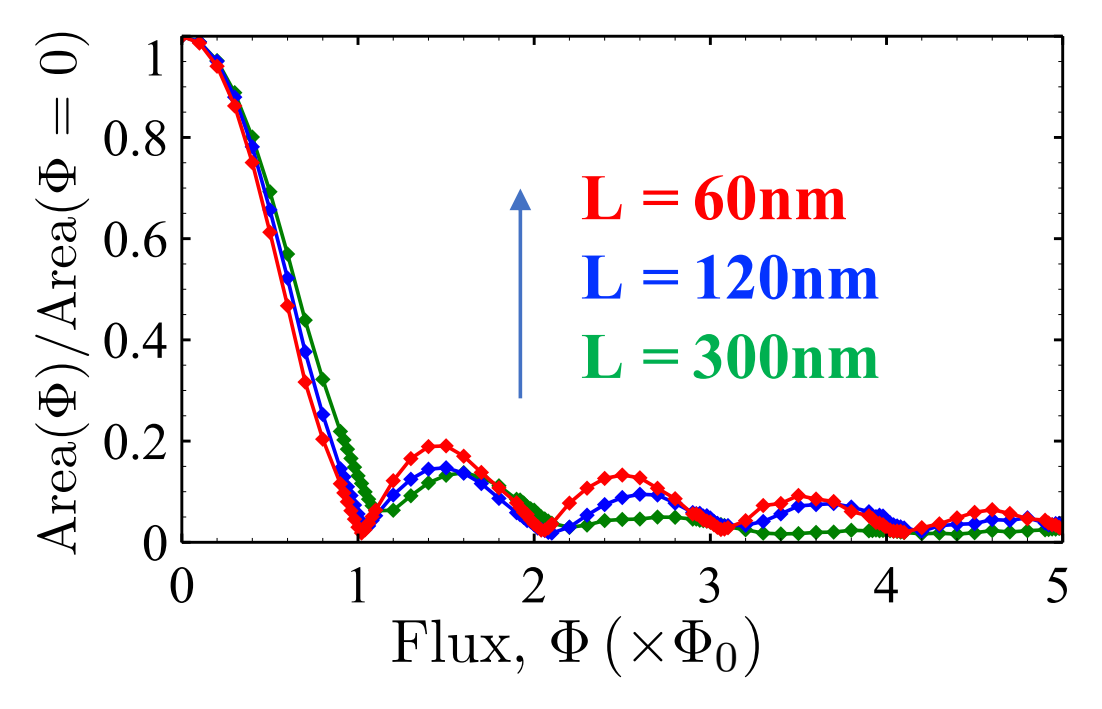


Figure 5.11: Normalized CCC area as a function of flux for fixed L/b = 5. W = 600nm, L = 60nm (red), 120nm (blue), 300nm (green). $\mu = 120meV$. The arrow shows the color order of amplitude height.

In Fig. 5.10, we plot the CCC area of junctions with narrow scattering region (L=60nm and W=600nm) as a function of flux. The width of the third terminal (bottom lead) b is changed from 12nm to full width b=L=60nm. Oscillations in short wires are still present in three-terminal junctions with nonzero minima at positive integer multiple of magnetic flux. However, the oscillations are suppressed as the width of the bottom lead increases ($b \to L$). The amplitudes of the oscillations for b=12nm are the largest. In Fig. 5.11, we compare this particular case (b=12nm, L=60nm) to the results of junctions with larger L, where L/b is fixed at 5. The oscillatory behavior almost completely disappears for L=300nm when flux gets larger than $3\Phi_0$.

5.2 Multiterminal Josephson junctions with more than three terminals

We studied short three-terminal junctions using the Beenakker approach in the tight-binding model in the previous section. The approach does not have geometry, terminal or number of channel restrictions as long as the short junction assumptions are valid. We now turn our attention to short junctions with more than three terminals. Our main aim is to understand the effects of gating and magnetic field on the multiterminal behavior of the 4-terminal X junction given in Fig. 5.15(a), which is motivated by the Manucharyan Group experiments [75]. We vary the chemical potential through the junction and the magnetic field on the scattering region to study the effects of gate voltage and magnetic field on the coupling between terminals. The locality/nonlocality of the couplings determines the shape of the CCC, which reveals the regime of the junction.

In addition to the gate voltage and magnetic field, the junction geometry is an important factor that determines the regime. By adjusting the geometry one can control the coupling between the terminals. Junctions having the same number of terminals but different geometries can show completely different behaviors. In Fig. 5.12, 4-terminal junction with rectangular scattering region is given. The scattering region is rectangular, similar to the three-terminal junction we studied in the previous section (Cf. Fig. 5.1). We attach the fourth terminal to the top of the scattering region. We choose the width W and L equal, so the scattering region is actually a square. This junction has three independent phases.

In junctions with three independent phases, the supercurrent scatter plots are three-dimensional. To simplify the data analysis, we consider the two-dimensional slice cuts to the three-dimensional data as in Fig. 5.13. Opposite terminals can be paired up [75]: The incoming current from one terminal can be made equal to the outgoing current from the opposite terminal. This means that the currents satisfy the plane equations $I_T + I_B = 0$ and $I_L + I_R = 0$. So, we first calculate the three-dimensional current and then take the

¹²The junction sizes in the experiments can be closer to the coherence length. To eliminate the errors due to breaking short junction approximation, one should follow the finite junction methods we use in the following chapter.

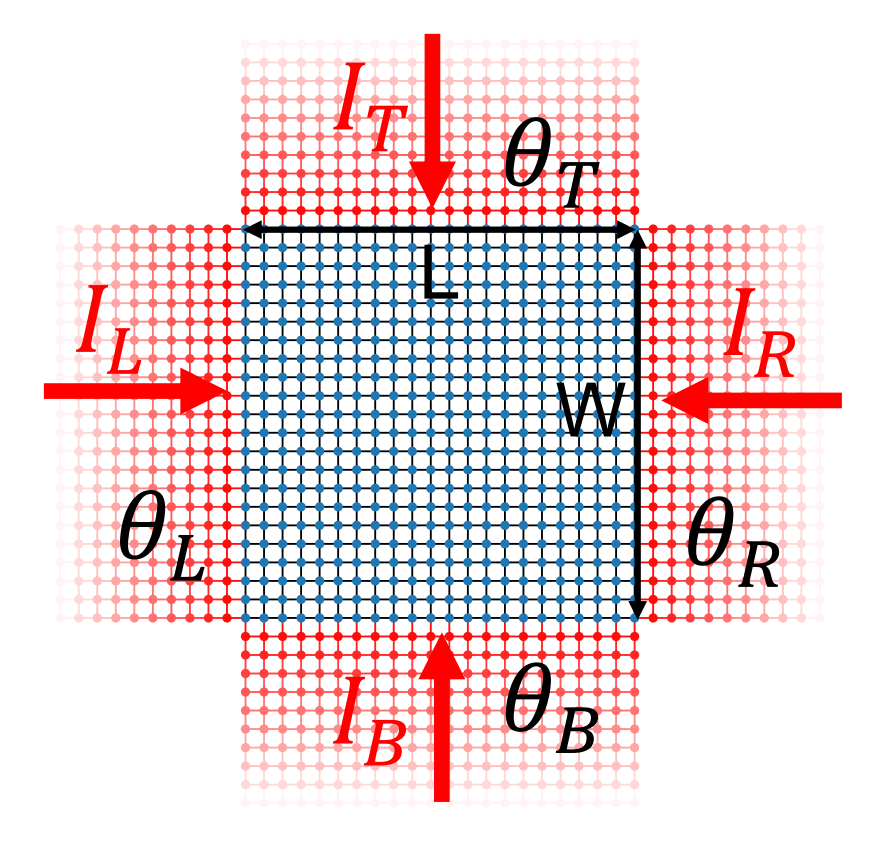


Figure 5.12: System sketch of 4-terminal Josephson junction with rectangular scattering region. The parameters are similar to the ones in Fig. 5.1. Here, the terminal widths have full widths. The top ("T") terminal has phase θ_T and the supercurrent coming from it is I_T .

points close to the planes.

In the absence of magnetic field, the data collection and analysis can get even simpler. The junction has time-reversal symmetry and the phases of opposite terminals can be chosen as negative of each other in symmetric junctions: $\theta_T + \theta_B = 0$ and $\theta_L + \theta_R = 0$. So, the three-dimensional data collection for four-terminal junctions becomes a two-dimensional endeavor and gets even easier when the flux is zero.

Turning back to the system in Fig. 5.12, the CCC for W=L=500nm for several chemical potential values is given in Fig. 5.14. CCC is rounded square for all μ because the geometry makes each pair of any two terminals have equal coupling. Therefore, the 4-terminal square model can be considered as a combination of six (4 choose 2) separate

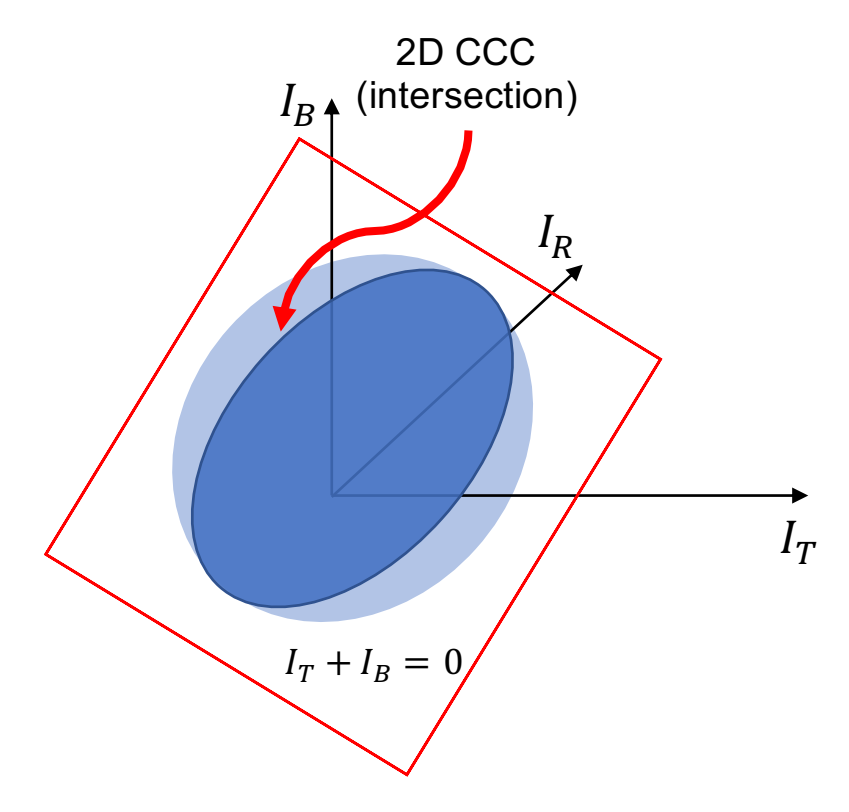


Figure 5.13: The region with pale blue is the three-dimensional supercurrent points for the leads with independent phases (T, R, B). Opposite terminals are paired up: $I_T + I_B = 0$ and $I_L + I_R = 0$. The boundary of the region formed by the intersection between the three-dimensional supercurrents and the plane $I_T + I_B = 0$ is the two-dimensional CCC.

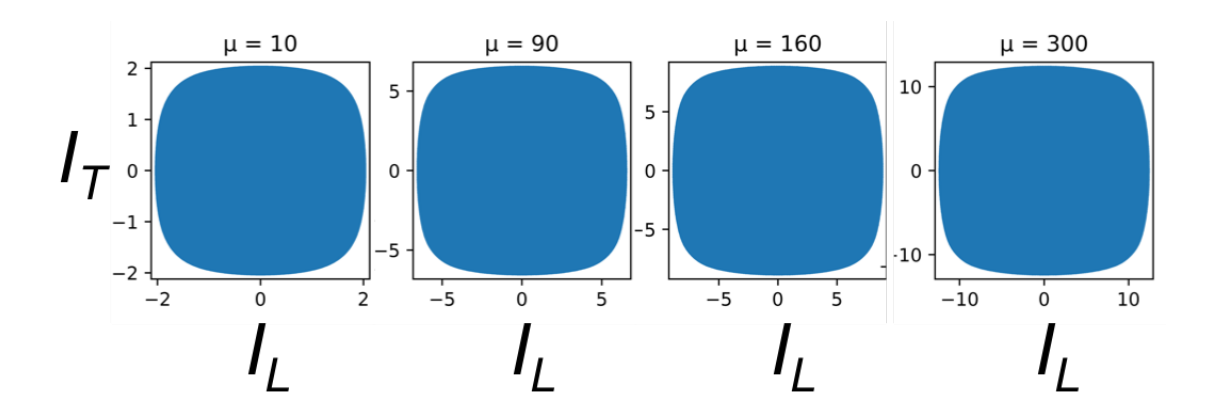


Figure 5.14: Scatter plots for the system in Fig. 5.12. μ unit is meV. L=W=500nm. Supercurrent unit is arbitrary.

Josephson junctions closely located to each other [195]. The area of the CCCs linearly increases with μ due to the reason described in Fig. 5.5.

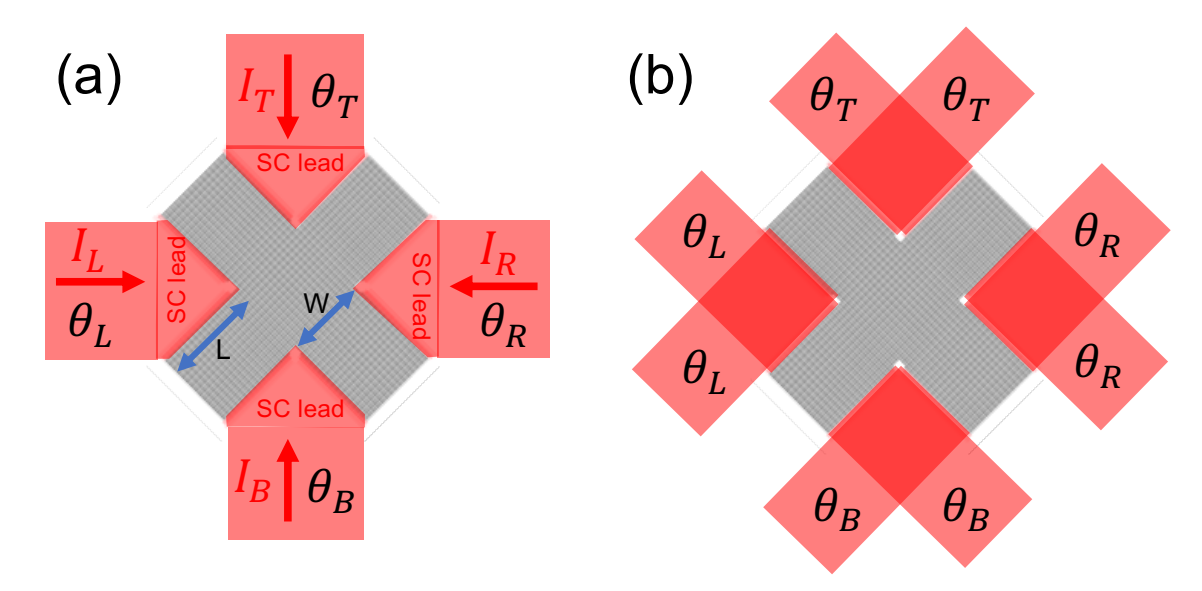


Figure 5.15: (a) X junction with arm length L and width W. (b) Approximate 8-terminal model for X junction.

If we change the geometry and create anisotropic coupling between terminals, we can observe different effects of gating. In Fig. 5.15(a), there is the target X junction we aim to simulate. Different than the leads attached to the rectangular scattering regions we used above, one has to use the rotated lattice for the leads to be attached to the X-shaped scattering region. In order to avoid such lattice type change, which generally does not occur naturally, we use the 8-terminal model in Fig. 5.15(b) as an approximate model to simulate the X junction.¹³ In the 8-terminal model, each lead consists of pair of 2 terminals with the same phase. Terminals are horizontally and vertically attached to the scattering region boundary. In the next chapter, we will study finite X geometries for which the same lattice type can be used both in the scattering region and the leads.

We show the CCCs for the 8-terminal X junction in Fig. 5.16. When μ gets small so that there are only few channels in the junction, there is a transition from rhombus to circle.¹⁴ When only adjoint terminals are coupled, the CCC is rhombus. Decreasing

¹³We thank Prof. Anton Akhmerov for his suggestions about Kwant usage [196].

¹⁴We will study junctions with nonuniform chemical potential in the next chapter. By fixing the chemical

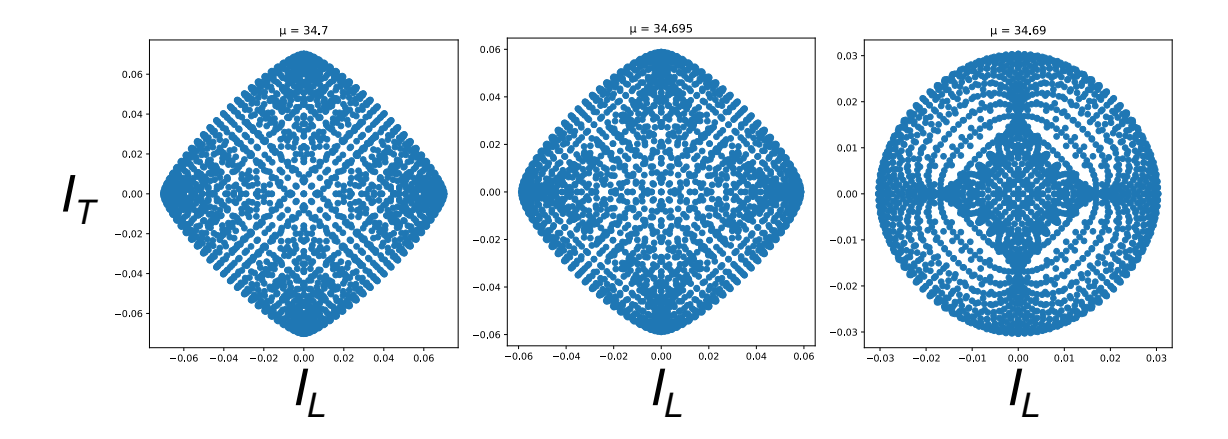


Figure 5.16: Scatter plots for the system in Fig. 5.15(b). $W=2\mathrm{nm},\,L=18\mathrm{nm},\,$ lattice constant $a=1\mathrm{nm}.$ Chemical potential is uniform in the junction. μ unit is meV. Supercurrent unit is arbitrary.

chemical potential increases the Fermi wavelength and the ABS wave functions become more extended in the scattering region, which makes the scattering process in the middle part of the scattering region having more dominance when the number of channels is small. The middle part connects opposite terminals and creates coupling less than the adjoint coupling. If coupling would be the same, then we would get rounded square as in 4-terminal square junction, Cf. Fig. 5.16.

5.3 Conclusions

We have presented the effects of top gate voltage and perpendicular magnetic field on multiterminal junctions. Ground state energy landscape is deformed in the presence of the magnetic field. The CCC clusters are identified on the energy-phase plane. With increasing magnetic flux, the sharp clusters appear and get detached from the central global minimum. Fraunhofer patterns persist in three-terminal Josephson junctions but they are suppressed.

We have also presented results about junctions having more than three terminals. Depending on the geometry of the junction, chemical potential modulation creates transition

potential in the leads and applying gate on the scattering region, one can fix the number of channels and can still control the Fermi wavelength in the scattering region. Shape transition gets more robust when number of channels is large and one can observe the effects of magnetic field more effectively.

in the shape of CCCs due to the coupling change between the terminals. CCC shapes of the four-terminal square junction do not depend on the chemical potential because the square scattering region couples each pair of terminals equally. However, in the X junction, the region of localization of ABS wave functions can alter the coupling between terminals. The wave functions localized in the middle makes the coupling between opposite sites stronger and the corresponding CCC becomes a circle. In the next chapter, we will continue studying the peculiar modulation of CCC with magnetic flux and gate voltage in finite junctions. We will study the X junction using more realistic finite models.

Chapter 6

Studies of finite multiterminal junctions

6.1 Introduction

In the previous chapter, we studied quantum transport in short junctions with semi-infinite leads using the scattering theory. The eigenstates of the Bloch Hamiltonian are the modes of the leads. The eigenvalues of the Bloch Hamiltonian categorizes the modes into incoming, outgoing and evanescent modes using the translational symmetry of the leads. The linear superposition of these modes give the wave function in the leads, the solution of which equals to the solution of the infinite¹ tail of the tight-binding system Hamiltonian. The other parts of the system Hamiltonian include the terms connecting the sites in the leads to the scattering region and the onsite and hopping terms of the scattering region. The unknowns are the wave function inside the scattering region and the S-matrix. By finding the wave function in the leads, one can truncate the system Hamiltonian into the scattering region and the sites in the leads which are directly connected to the scattering region. The unknowns can be calculated by solving the time-independent Schrodinger equation in the scattering region and using the boundary condition connecting the scattering region to the

¹The tail is infinite because the leads are semi-infinite. In this context, "semi-infinite" is used to signify that the leads have an end point, which is the scattering region boundary.

leads.

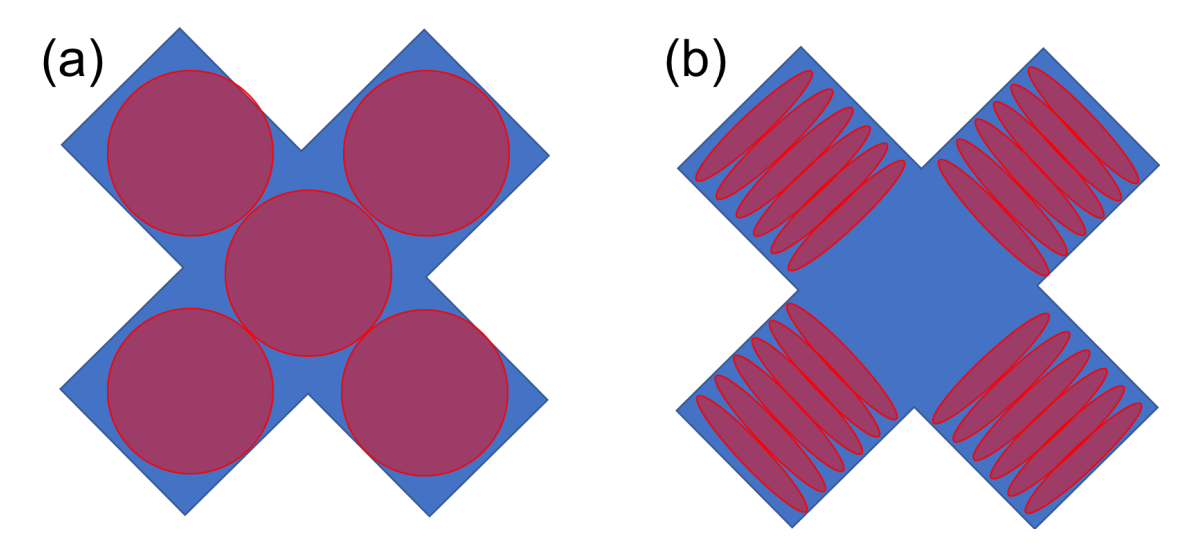


Figure 6.1: ABS wave function localization in the scattering region. (a) Extended ABS wave functions can be localized with equal probability in the arms and middle region if the system geometry is finely tuned. The coupling between the opposite junctions create rounded CCCs. (b) When the Fermi wavelength is small, the arms are more dominant because the area of the arms are larger than the middle region (because L > W). So, CCC becomes a rhombus due to lack of connection of opposite junctions. The figure in (b) is given for a system where the middle region localizations are neglected.

Kwant uses this approach as explained in Ref. [81] and its tools are especially useful for systems with translationally invariant semi-infinite leads. Bound state problem in infinite and mostly-translationally invariant systems have been studied in [197, 198]. On the other end, one can also be interested in studying systems which do not have geometries allowing simple attachments of semi-infinite leads. Such systems can produce intriguing new phenomena which may not be understood via approximate models. In the last chapter, we compared the CCCs for the junctions with the square and X-shaped scattering regions. We used the infinite 8-terminal model as an approximation to the X junction. We take the chemical potential small in order to make the number of channels small. In this limit, the scattering process occurs mostly in the middle of the leads. This model is not very useful anymore when the number of channels is large. Even though the pair of leads have the same phases, there is no direct connection between the separate leads – they are only connected

to the scattering region. The edge of the disconnected leads produce protrusions in CCCs when the number of channels is large, so the effects of the disconnection on the scattering process cannot be ignored.

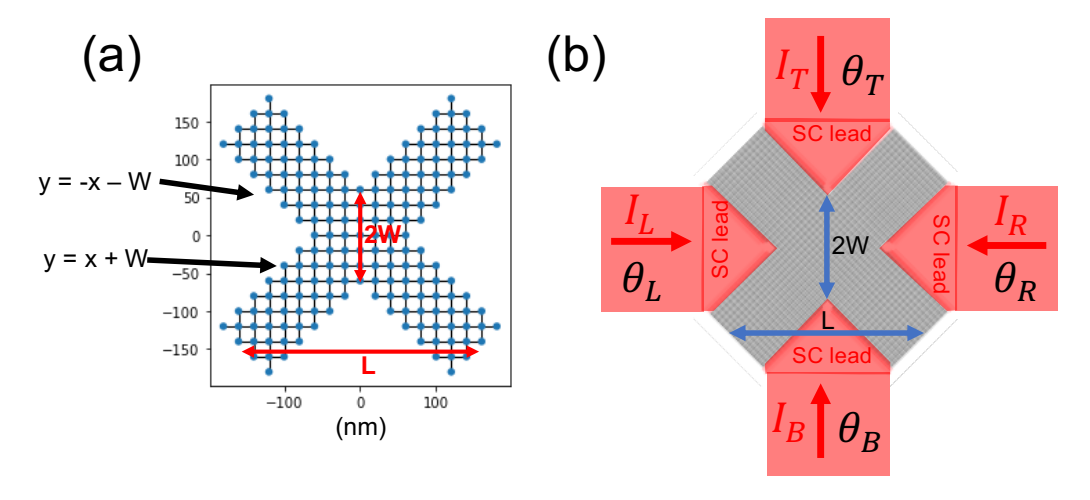


Figure 6.2: (a) Scattering region, (b) X finite system.

Another source of error is the size of the junctions. Short junction approach provides efficient methods of quantum transport calculations. One can separate the process of solving wave functions of the leads and the scattering region. Finding the coefficients of the Smatrix and the scattering region wave function can be achieved by just solving the system Hamiltonian truncated into the subblocks directly related to the scattering region – no need to take the leads into account after calculating the lead modes. Short junction method, albeit being efficient, is not useful in general. Scattering regions in experimental setups [75, 76, 91] are generally not as small as theoretical models.

To be able to study more realistic theoretical models and eliminate the problems that can arise due to the length of the junctions and system geometry approximations, we form finite systems with leads longer than the coherence length. We divide the finite system into superconducting and normal regions and assign phases to each lead. The scattering region and the system plot for the finite X junction are given in Fig. 6.2. The scattering region in Fig. 6.2(a) is the same as the one in previous section but with different L, W definitions.²

²The difference here is simply because of the definitions of the lines (see Fig. 6.2(a)) used to define the

6.2Finite System Simulations

The tight-binding Hamiltonian of the finite system is given as:

iltonian of the finite system is given as:
$$H = \begin{bmatrix} H_L & V_L & & & \\ V_L^\dagger & \ddots & & & \\ & & \ddots & & \\ & & & L & V_L & \\ & & & V_L^\dagger & H_L & V_{LS} \\ & & & & V_{LS}^\dagger & H_S \end{bmatrix}, \qquad (6.1)$$
 ering region Hamiltonian, H_L is the onsite Hamiltonian, V_L is the

where H_S is the scattering region Hamiltonian, H_L is the onsite Hamiltonian, V_L is the hopping term that connects leads to each other and V_{LS} is the hopping term that connects leads to the scattering region. Eq.(6.1) is the truncated version of the Hamiltonian in Eq. (4) of Ref. [81]. Truncation is legitimate because we take the leads much longer than the coherence length, typically between 1.2 to 20 times longer. If the chemical potential is very small, the coherence length becomes very small. So, we need to choose large lead lengths (comparing to the coherence length) for junctions with small chemical potential in order to make the leads not shorter than the scattering region length. On the other hand, junctions with large chemical potentials have large number of channels and large system Hamiltonian matrix. The coherence length is generally larger than the scattering region sizes. The burden then is to diagonalize the large system Hamiltonian. Therefore, for such junctions, we choose the lead length around a few times longer than the scattering region sizes. A rule of thumb for the good choice of legitimate lead length is to test whether number of channels (number of positive subgap energies) change with the lead length or not. We choose the lead lengths accordingly and check the change in number of channels while varying the lead length.

The choice for the length of the leads is crucial because if it is too short, then lead modes will not be approximated as plane waves and there will be unwanted interference effects on

separation between the superconducting and normal regions. Since the leads are not rectangular anymore and they have a triangular part attached to the scattering region, it is more convenient to define the boundaries using the line equations provided in the figure.

our results. A way to check whether lead lenghts are selected long enough is to compare the results obtained from a two-terminal finite system results to the Ambegaokar-Baratoff relation. This is a well-known result for 2-terminal junctions and can provide an easy test. It can be summarized as the following. Critical current I_C is proportional to Δ in short junctions when temperature goes to zero [199]. If for a short junction, long (much longer than coherence length) finite leads are attached, then $I_C \propto \Delta$.

The Ambegaokar-Baratoff test provides a sanity check for our code in the limit of short junctions. However, the finite junction method is not limited to short junctions. A good side of the finite system method over the short junction method is that we can also work with long junctions with small chemical potential and coherence length using the former. Such systems have smaller Hamiltonian matrix and can still show the local/nonlocal transition we are searching for. Short junction method is in general practical but one has to work with large chemical potential in order to obtain long coherence length comparing to the system sizes. This produces large S-matrix and can cause long computation times for large systems. Here, we don't abide ourselves to the binding criteria of short junctions but we also study systems with large matrices of μ up to 40 meV.

In Fig. 6.3 we provide the two-terminal finite system (a), current (b) and critical current (c) as a function of phase plots for the SNS junction. We choose the chemical potential $\mu = 0.05$ meV and vary Δ between 0.04 and 0.2meV. Since Δ is varied, coherence length is also varied between 80 and 400 µm. The normal region length L is shorter than the coherence length but width W is longer than the maximum coherence length we consider. Long W and short coherence length with increasing Δ are the reasons why the junction slightly deviates from $I_C \propto \Delta$. We could select μ larger and make sure that W, L are much smaller than the coherence length and $L_{\rm Lead}$ is much larger than the coherence length but we wanted to provide an approximate quick test here.

If μ is too small, then the coherence length is small and Fermi wavelength is large. Sizes of the system should be small so that they are smaller than coherence length for short

 $^{^3}$ I have results for $\mu \sim 40$ meV, whose Hamiltonian is huge and has many number of channels. We will provide those results in our paper. It is currently in preparation.

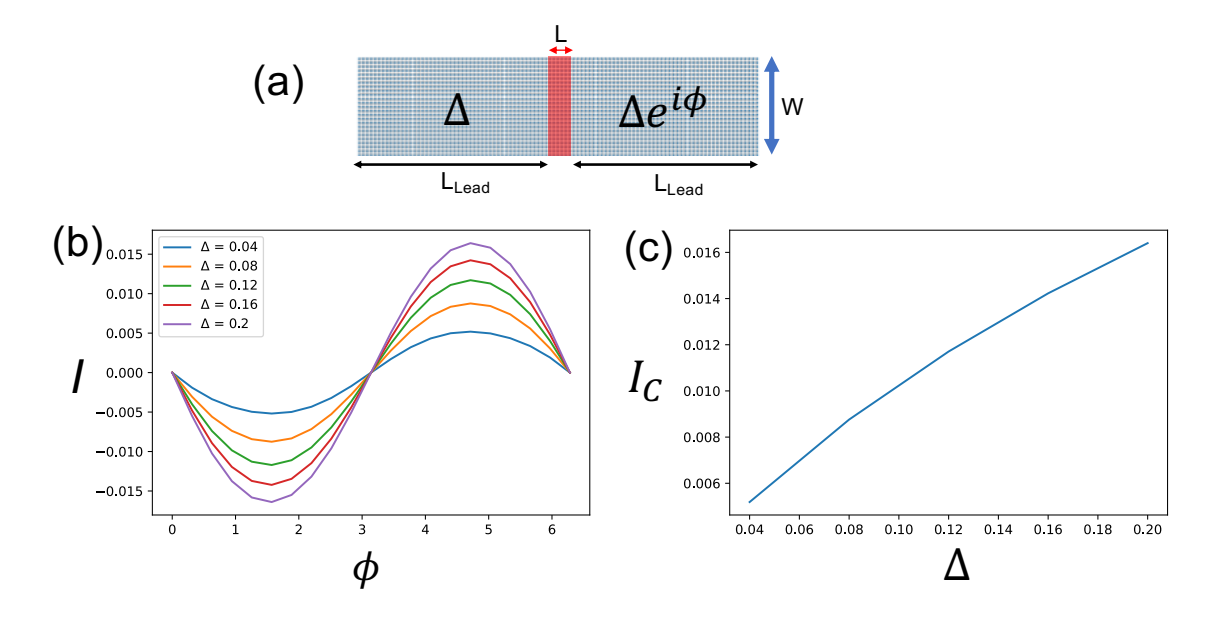


Figure 6.3: (a) 2-terminal finite system. Long wide junction with width W=500nm, L=40nm. $L_{\rm Lead}$ is chosen much longer than the coherence length. (b) Current I as a function of phase ϕ (between 0 and 2π). (c) Critical current as a function of Δ . Critical current is defined as the maximum positive or negative current. Supercurrent units are arbitrary in this chapter (Coefficient $\frac{2e}{\hbar}$ should be multiplied by the currents).

junction limit. However, number of channels then can be zero because W would be too large to fit Fermi wavelengths in it. That's why we choose a relatively large W for the example in Fig. 6.3. While varying chemical potential, coherence length changes. In our studies with junctions with more than two terminals, we take precaution against such parameter changes. We fixed this problem by selecting lead length as a multiple of coherence length (L_{Lead} is not fixed) whenever it is necessary.

The continuum Hamiltonian for the junction is given by:

$$H = \left[\frac{\hbar^2}{2m} \left(k_x^2 + k_y^2 - e\mathbf{A} \right) - \mu + V \right] \sigma_z + \Delta \cos(\theta) \sigma_x + \Delta \sin(\theta) \sigma_y, \tag{6.2}$$

where the gate voltage V can be uniform or nonuniform throughout the junction. In the nomenclature of this thesis, we sometimes call the effective chemical potential as $\mu - V$. $\Delta = 0$ in the normal region and nonzero (in the form of s-wave superconductivity) in the leads. A is the vector potential chosen in Landau gauge and it can be switched on in the scattering region, similar to the previous chapter. Superconducting phases are different at

the left (θ_L) , right (θ_R) , top (θ_T) , bottom (θ_B) of the scattering region.

Eq.(6.2) is similar to the Hamiltonian of the previous section. However, the former is represented by 2-by-2 Pauli matrices because it depends on Δ . The latter does not have Δ dependence because leads are normal. Δ is taken into account by the structure of the Beenakker formula [79]. To find the ABS energies below the gap, the leads were assumed to be normal in the previous section. If we assumed that the leads had Δ -dependence in the previous chapter, we would get the spectrum of quasiparticle excitations that propagate in the leads above the gap.

To find the ABS energies, we calculate the eigenvalues of the system Hamiltonian, Eq.(6.1), and take the positive energies below the gap Δ . We study bound states in finite systems following similar approaches described in the codes of the Refs. [182, 200]. We summarize the process as follows⁴:

- 1) Make the system. Write Hamiltonian in terms of momenta and position operators. Operators are multiplied with coefficients which are variable depending on the region: Leads depend on superconducting gap, the normal scattering region does not. Each region Hamiltonian includes terms specific to that region, such as chemical potential, gate voltage, superconducting phase and gap.
- 2) Discretize the Hamiltonians for each region. Position and momentum operators are discretized. Tight-binding Hamiltonian is obtained in the form of Eq.(6.1).
- 3) Utilize the sparsity of the Hamiltonian and use Multifrontal Massively Parallel Sparse Direct Solver [201] to find eigenvalues of Eq.(6.1). Calculate N minimum positive eigenvalues. If the max calculated eigenvalue is still minimum than the gap, N is increased in a while loop.
- 4) Take the sum of the subgap energies, calculate ground state energy E_{gs} . Derivatives with respect to phases (I = $\frac{2e}{\hbar} \partial_{\theta_i} E_{gs}$, where θ_i is the phase of a lead) give the current of each lead.

To emphasize again, one can consider μ - gate as the effective chemical potential. We

⁴The code will be available in my GitHub account: https://github.com/relugzosiraba.

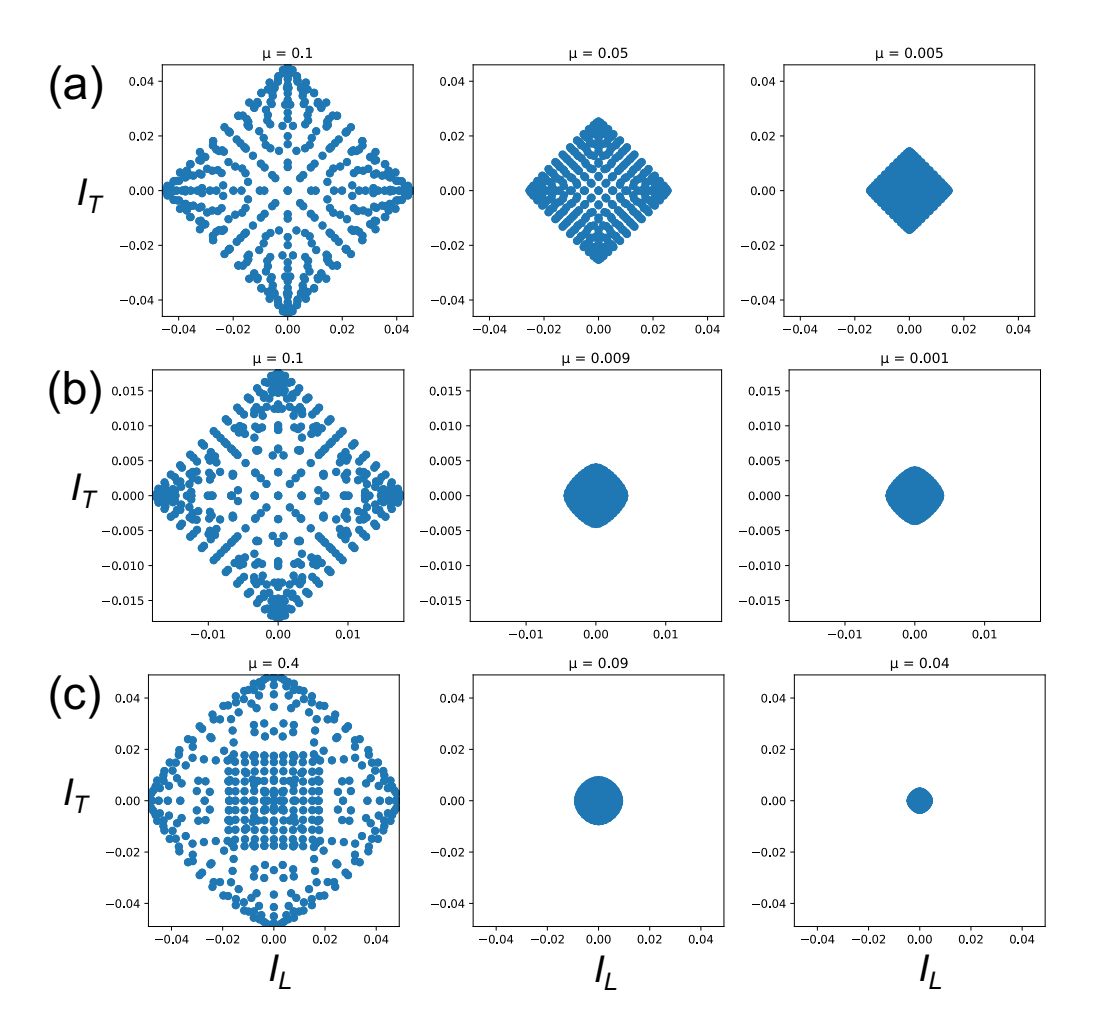


Figure 6.4: CCCs for $W=60 \mathrm{nm}$. (a) $L=720 \mathrm{nm}$ (b) 400 nm, (c) 300 nm. Flux is zero. Chemical potential is the same over all junction. Top gate voltage is zero. μ unit is meV throughout the chapter. Supercurrent unit is arbitrary throughout the chapter.

use the phrase "nonuniform μ " interchangeably even when μ is fixed and only gate is varied. The gate makes the scattering region's effective chemical potential smaller than the leads, which can produce nonlocal/local CCC shape transition.

Models with nonuniform μ is more realistic. Top gate hardly affects Al layer (leads), so μ should be fixed and gate is applied only on the scattering region. Even more realistic models include nonuniform gate on the scattering region and include several elements causing nonuniformness such as the following. The band bending due to ohmic contact between Al (of the leads) and InAs in the epitaxial heterostructure (see Fig.1 of Ref. [75] for the

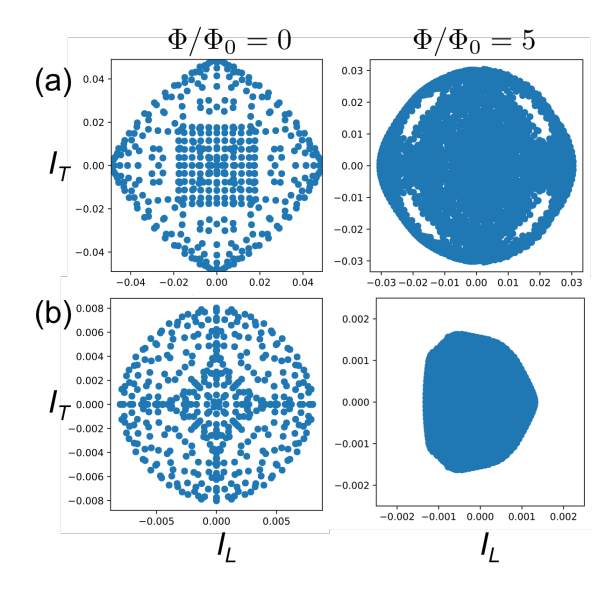


Figure 6.5: For $W=60\mathrm{nm}$ and $L=300\mathrm{nm}$ at zero flux, CCCs are rhombus and circle for $\mu=0.4\mathrm{meV}$ and $\mu=0.09\mathrm{meV}$, respectively (see Fig. 6.4). (a) When flux is varied, rhombus preserves its shape and current inversion symmetry, (b) whereas the circle shape transforms into a shape with broken current inversion symmetry. CCCs for zero flux are given in the left column for comparison.

system layers) should be taken into account [202]. What is more, electrostatic potential lines are banded in the edges of Al. One should also consider disorder due to impurities. The supercurrent vortices formed by magnetic flux are effected by impurity scattering.

As we started exploring in the previous section, in addition to the chemical potential, geometry is also crucial for the local/nonlocal CCC transition. For the right chemical potential and gate combination, by fine tuning of the aspect ratio (arm length)/(middle region width) = (L-W)/(2W), one can obtain the CCC transition. The extended/localized nature of the ABS wave function determines which part of the junction is more dominant, which is summarized in Fig. 6.1. Such dominance happens in the systems with proper choice of aspect ratio and the Fermi wavelength. The Fermi wavelength can be controlled using the chemical potential and gate voltage. When negative gate is applied while μ is being fixed or when gate is zero and μ is decreased throughout the junction, the Fermi wavelength gets large. When the gate is small or when it is zero and μ is large, the Fermi wavelength gets small.

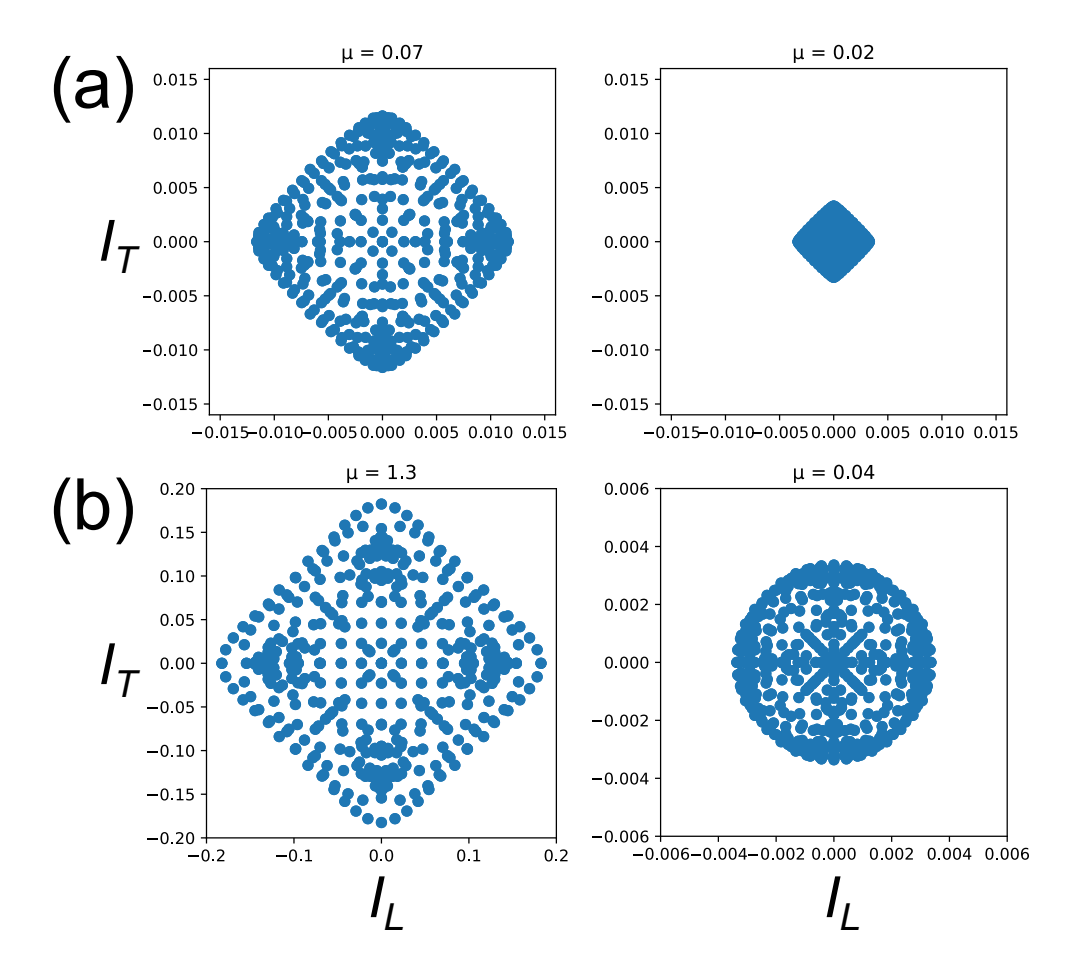


Figure 6.6: CCCs for L = 720nm. (a) W = 140nm, (b) W = 220nm. Flux is zero. Chemical potential is the same over all junction. Top gate voltage is zero.

For the local regime depicted in Fig. 6.1(b), there is no ABS wave function localized in the center. Indeed, such a system is experimentally obtainable thanks to impurity scattering. Even if there is no impurity, if both arms and the middle region are occupied at the same time by ABS with short wavelengths, arms would still be more dominant due to its larger area.

In Fig. 6.4, W = 60nm (width of the junction) fixed. L = 300, 400 or 720nm. We show results for μ up to 0.4meV, for which junctions have small number of channels.⁵ The CCC is rhombus for this chemical potential range when L is large (720nm). For the

⁵Note that when μ is extremely small, there are no channels or scattering anymore. We are away from that limit (which was considered in the previous chapter.)

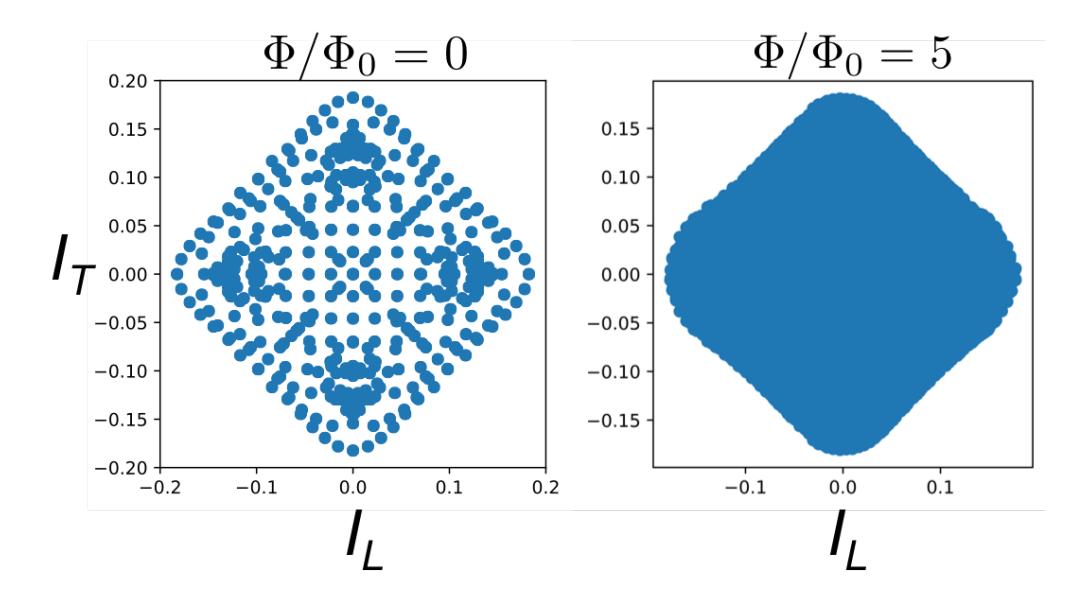


Figure 6.7: Flux is varied for the rhombus CCCs of W = 220nm, L = 720nm. Rhombic shape is preserved.

smaller L=400nm, the CCC gets circular when the chemical potential is decreased. There needs to be fine tuning to obtain the proper rhombus-circle transition. This happens when L=300nm. Note that we skipped the intermediate figures for which the system is in a transition mode from rhombus to circle. When μ is decreased to a value even less than $\mu=0.09$ meV, the area shrinks (as expected) and the CCC keeps its shape (circle), which is expected for a robust shape transition. For the approximate 8-terminal X infinite system we studied in the previous chapter, we obtained some transitions which do not follow the regular pattern. Circle could become rhombus again for μ which is smaller than the chemical potential for which the initial transition occurs. Note that the scales are not necessarily the same for CCC figures in this chapter. We note that CCC area increases (decreases) with increasing (decreasing) μ . In Fig. 6.5, we give how the flux on the scattering region modifies the CCC for given rhombus and circles of L=300nm. Area shrinks for both. Inversion symmetry with respect to the origin is preserved for the rhombus but it is broken for the circle, where the currents of opposite terminals are correlated via the middle region. So, the magnetic field effects occurring at the middle region breaks the inversion symmetry in

⁶Such figures are not presented in this thesis because their CCCs do not represent the regular patterns.

nonlocal junction (circle) but it does not break the one where the arms are more dominant (i.e. local junction with rhombus CCC).

Now, for the case when L = 720nm, we increase W and get the results as in Fig. 6.6. For W = 140nm, the CCC is rhombus for all μ . If W is increased enough, then the transition may occur again. We see that this happens at W = 220nm. The result for magnetic flux variation of the rhombus at $\mu = 1.3$ meV is given in Fig. 6.7. The shape is preserved and its area shrinks. The circular CCC flux variation is work-in-progress. We could observe the current inversion symmetry breaking only for some of the circular CCCs when magnetic field is switched on. With a more realistic modeling of the junction with more proper choices of nonuniform chemical potential and disorder, more shape transitions can be obtained as expected.

Finally, let's switch on the gate voltage. We present the results in Fig. 6.8. We fix $W=140\mathrm{nm}$. L, μ and gate is varied. As opposed to the case when gate = 0, transition occurs for larger μ when the negative gate is switched on. The negative gate increases the ABS wavelength inside the scattering region. If the number of channels is larger, the shape transition follows strict patterns and the CCC transition can be investigated properly without sudden reverse transitions. When there is no gate, the transition occurs while μ is being decreased, which is the number of channels \rightarrow 0 limit. In such junctions, the common pattern of transition is weakly followed and reverse transitions may occur because number of channels is small and therefore the system is prone to sudden fluctuations due to geometry change or change of other parameters. If the number of channels is large, the collective interference creates meaningful patterns. Note that we can observe the transition for μ being as small as 3meV. For the same $L=720\mathrm{nm}$, $W=140\mathrm{nm}$, chemical potential defines whether there will be transition or not (Cf. (a) and (c)). CCCs in Fig. 6.8(a) stay as rhombus for small μ . For $\mu=3\mathrm{meV}$, when $L=600\mathrm{nm}$, we observe rhombus to circle transition.

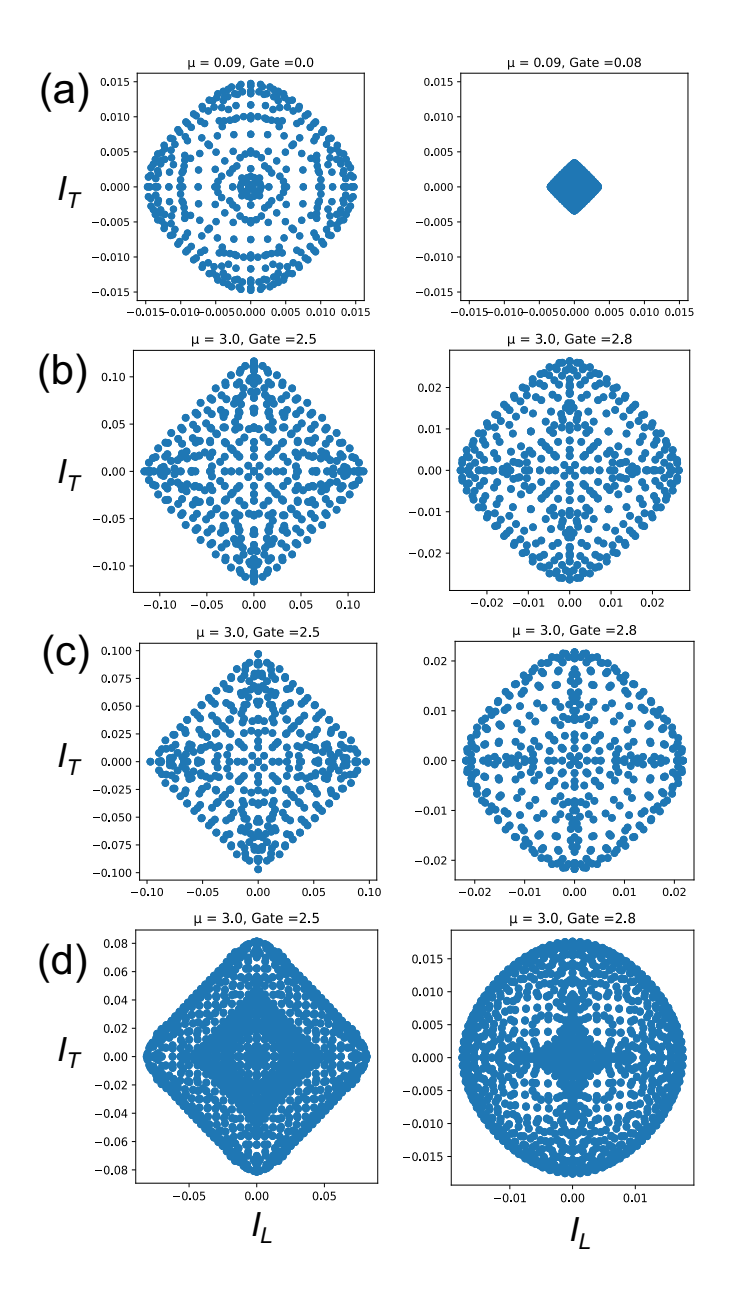


Figure 6.8: CCCs for W=140nm. L is varied. Top gate voltage is varied. (a) W=140nm, L=720nm for $\mu=0.09$ meV. CCC shape is preserved for small μ (= small number of channels). (b, c, d) Fix W=140nm, and $\mu=3$ meV. Vary L. (b) L=840nm, (c) L=720nm, (d) L=600nm. For larger L, the arms of the scattering region are more dominant. Therefore, CCCs are rhombus. As can be seen in (d), the shape gets circular when the gate voltage is increased for the right choice of L because the coupling between the opposite terminals gets stronger due to extended ABS wave functions inside the scattering region.

6.3 Conclusions and Outlook

Junctions with special geometries can exhibit effects which are not exhibited by the simple geometries. To simulate junctions with special geometries, finite junction methods are useful. The scattering region and the leads attached to it can be of the same type of lattice. The leads become finite but much longer than the coherence length. Eigenvalues of the system Hamiltonian are found exploiting the sparsity of it. We used finite junctions methods to simulate X model. Comparing to the 8-terminal approximate X model considered in the last section, we built a system with four terminals and exact geometry as desired. For wide junction with long arms, the local effect is dominant and CCC is rhombus and does not transform into other shapes. We observed robust local to nonlocal (rhombus to circle) transitions for certain aspect ratios of the junction while tuning chemical potential, gate voltage and magnetic field.

X junction is a special junction and a platform exhibiting many symmetries (such as (a)symmetric coupling system geometry, time-reversal, current inversion symmetries) at once. Magnetic field on the scattering region breaks the time-reversal symmetry and CCC may lose the inversion symmetry with respect to the origin depending on the regime (local or nonlocal) of the junction. If there is a nonlocal (due to coupling via the center of the scattering region) Josephson effect, magnetic field breaks current inversion symmetry. Magnetic field does not break current inversion symmetry if the arms are dominant. This difference allows us to distinguish between local and nonlocal regimes using the X junction. For the local regime, the arms are dominant and the inversion symmetry breaking effects are cancelled out due to the X junction geometric symmetry. This cancelling may not happen in geometrically asymmetric junctions, which will be checked in our future studies. Understanding further flux effects under disorder and different choices of nonuniform chemical potential is also a work-in-progress.

Fine tuning of parameters to obtain the shape transition can be burden especially for finite systems, where exact diagonalization computationally costs a lot for large systems (large μ and/or system). To overcome that, I will incorporate machine learning techniques

to identify CCC shapes with less human interference. An algorithm which focuses on finding the boundary (CCCs) of the scatter plots without spending much time in the interior is well-desired.

Part III

Concluding Remarks and Bibliography

Chapter 7

Conclusions and Outlook

We covered various topics in interacting quantum systems that are complementary to each other. Our studies include theoretical modeling and numerical simulations of disordered quantum spin chains, multiterminal Josephson junctions and superconducting circuits. My past experiences shape my future goals. Not all questions I have been studying during my PhD years are answered here. I will provide answers to those questions in the near future. My experience and background will help me extend the depth of my knowledge.

We studied the response of disordered systems to weak local periodic drive in Chapter 2. We considered a spin chain in which one of the spins is driven. We study the effects of the drive on the crossover between the many-body localization (MBL) and ergodic regime after one period. We characterized the response as the overlap between the states started from the initial states and evolved under the Heisenberg Hamiltonian with and without drive. The statistics of the response show different behaviors depending on the strength of the disorder. We further studied time dynamics of the system. The variance of the total spin in z-direction gives the measure of localization for a given state. The variance after one period can be considered as the diffusion coefficient and it is correlated to the fidelity susceptibility. We measured the speed of thermalization using spin accumulation for a given number of periods. The speed of thermalization is significantly different for the ergodic and MBL phases. In this study, we considered local harmonic drive with moderate

drive frequency. In the future, I will explore the prethermal regimes that occur for large drive frequencies. Prethermal systems can exhibit topological phases and time crystals.

In Chapter 2, we studied the collective response of the spin chain to the local drive by calculating the overlap of the driven and undriven states and variance of the total spin. I will also study how individual spins respond to the local drive in an open chain. Each spin responds to the local drive differently depending on the distance to the driven spin. We collaborate with experimental groups to check how our ideas can be realized, one of the collaboration topic is on fluxonium qubit systems. Fluxonium qubits are more preferable comparing to other superconducting qubits because they can have strong anharmonicity, long coherence time and they exhibit strong coupling properties. Due to these properties, these systems can simulate spin-1/2 chains effectively. We studied the phase diagram of the fluxonium chain by calculating the energy gap between the ground and first excited levels. We estimated the boundary between the antiferromagnetic and paramagnetic regimes by using fidelity susceptibility. As experimentally accessible methods, we tried using magnetization to probe edge states and studied response of qubits to a local spin flip.

1-d Ising chain can be mapped onto Kitaev chain (which can exhibit Majorana fermions) via Jordan-Wigner transformation. Using this mapping, we demonstrated that edge states can be probed using magnetization but this method is not enough to come to a conclusion about the exact site where the edge state is localized. We will study the localization properties of edge states as a test to identify whether they show similar properties to Majorana states.

In Chapter 4, we proposed the steered quantum adiabatic algorithm. The spin chain we considered is a common testbed for quantum computing: 1-d transverse Ising spin-1/2 chain with nearest neighbor interactions. The initial state is chosen as the ground state of the initial Hamiltonian, which is easy to prepare. Quantum adiabatic algorithm is used to find the ground state of an Ising spin-1/2 chain, which can be encoded as an optimization problem. Our aim was to keep the state as close as possible to the ground state during the course of the computation so that the final state is close to the ground

state of the final Hamiltonian. To do that, we proposed an intermediate steering term that eliminates avoided level crossings which cause leakage from ground state to the excited states via Landau-Zener transitions. We applied local steering terms (applied to each spin separately) and also combined these local terms with cluster terms, which are applied to clusters of spins.

The steering method is model-independent. It is also useful to efficiently solve ground states of systems with long-range interactions and spin glasses with all-to-all coupling. We started applying the steering method for spin-1 chain to exploit the Haldane gap, which increases the energy separation between ground state and excited states [203]. The Haldane gap appears in chains with integer spins but not for the spin-1/2 chain, such as the one we considered in Chapter 4. So, using spin-1 chains can be useful to tackle difficult optimization problems.

In Chapters 5 and 6, we study multiterminal Josephson junctions in tight-binding infinite and finite models. For infinite short junction; after lead modes are obtained, the system Hamiltonian can be truncated into an effective Hamiltonian which have sizes of scattering region and the closest lead degrees of freedom. For finite systems, one can truncate the infinite system (into a still large matrix) if long enough leads are chosen. The system Hamiltonian is diagonalized and one can then obtain subgap energies. Both approaches have its own benefits. Infinite junctions can generally provide quick solutions if the short junction assumptions are satisfied. On the other hand, finite junction method is not limited to short junctions and special geometries can be explored.

We define the critical current contour (CCC) for multiterminal junctions as the generalized notion of the critical current in two-terminal junctions. We demonstrated that the magnetic field deforms the energy-phase space and sharp corners appear in CCCs as a result. We concluded that additional terminals modify Fraunhofer patterns and suppress the oscillations.

We investigated the transition from conventional to multiterminal regime in the scope of the symmetry considerations of the geometrically symmetric X junction. By gate tuning, the junction regime can be determined. The regime of the junction can be understood via the shape of CCCs. In the conventional regime where only neighboring terminals are coupled, the CCC is rhombic. On the other hand, if there is coupling between opposite terminals, the CCC gets rounded.

We discussed effects of time-reversal symmetry breaking on the inversion symmetry breaking of CCCs. In the conventional regime where arms are dominant, the inversion symmetry is not broken in the presence of magnetic field. However, the magnetic field breaks the inversion symmetry of the junction in multiterminal regime where the center of the scattering region couples opposite terminals. Therefore, whether the junction is in the local or nonlocal regime can be identified by applying magnetic field. Note that we consider small magnetic flux regime here, where the effect of the flux manifests itself as the Fraunhofer patterns. If the flux is large, the supercurrents dies away and inversion symmetry is surely broken regardless of whether the junction is in the conventional or multiterminal regime.

In Fall 2019 at Los Alamos National Lab., I studied topological versions of multiterminal JJ which are based on Dirac materials with superconducting (S) leads and ferromagnetic (F) scattering region. 2-terminal SFS junctions can exhibit topological states [204]. I will finish my analysis of how adding more terminals change the topological behaviors.

I used the Python quantum transport package Kwant for my time-independent calculations of multiterminal JJ. I am planning to explore time-dependent quantum transport through multiterminal JJ. It is possible to study thermoelectric and other dissipative dynamics with the time-dependent version of Kwant, named t-Kwant, which is currently under development [205, 206].

Bibliography

- [1] M. A. Nielsen and I. Chuang, "Quantum computation and quantum information," 2002.
- [2] N. S. Yanofsky and M. A. Mannucci, Quantum computing for computer scientists. Cambridge University Press, 2008.
- [3] S. Aaronson, Quantum computing since Democritus. Cambridge University Press, 2013.
- [4] A. G. Bromley, "Charles Babbage's Analytical Engine, 1838," Annals of the History of Computing, vol. 4, no. 3, pp. 196–217, 1982.
- [5] J. Holt, When Einstein walked with Gödel: excursions to the edge of thought. Farrar, Straus and Giroux, 2018.
- [6] H. H. Goldstine and A. Goldstine, "The electronic numerical integrator and computer (eniac)," *IEEE Annals of the History of Computing*, vol. 18, no. 1, pp. 10–16, 1996.
- [7] M. Guarnieri, "The Unreasonable Accuracy of Moore's Law [Historical]," *IEEE Industrial Electronics Magazine*, vol. 10, no. 1, pp. 40–43, 2016.
- [8] R. P. Feynman, "There's plenty of room at the bottom," California Institute of Technology, Engineering and Science magazine, 1960.
- [9] Y. Manin, "Computable and uncomputable," Sovetskoye Radio, Moscow, vol. 128, 1980.
- [10] R. P. Feynman, "Simulating physics with computers," *International Journal of Theoretical Physics*, vol. 21, pp. 467–488, May 1982.
- [11] D. Deutsch, "Quantum Theory, the Church-Turing Principle and the Universal Quantum Computer," *Proceedings of the Royal Society of London A: Mathematical, Physical and Engineering Sciences*, vol. 400, pp. 97–117, July 1985.

- [12] D. Deutsch and R. Jozsa, "Rapid solution of problems by quantum computation," *Proceedings of the Royal Society of London. Series A: Mathematical and Physical Sciences*, vol. 439, no. 1907, pp. 553–558, 1992.
- [13] D. R. Simon, "On the power of quantum computation," SIAM journal on computing, vol. 26, no. 5, pp. 1474–1483, 1997.
- [14] P. W. Shor, "Polynomial-Time Algorithms for Prime Factorization and Discrete Logarithms on a Quantum Computer," *SIAM J. Comput.*, vol. 26, pp. 1484–1509, Oct. 1997.
- [15] L. K. Grover, "A Fast Quantum Mechanical Algorithm for Database Search," in *Proceedings of the Twenty-eighth Annual ACM Symposium on Theory of Computing*, STOC '96, pp. 212–219, ACM, May 1996.
- [16] B. Apolloni, C. Carvalho, and D. De Falco, "Quantum stochastic optimization," Stochastic Processes and their Applications, vol. 33, no. 2, pp. 233–244, 1989.
- [17] S. Kirkpatrick, C. D. Gelatt, and M. P. Vecchi, "Optimization by simulated annealing," *science*, vol. 220, no. 4598, pp. 671–680, 1983.
- [18] T. Kadowaki and H. Nishimori, "Quantum annealing in the transverse Ising model," *Physical Review E*, vol. 58, no. 5, p. 5355, 1998.
- [19] E. Farhi, J. Goldstone, S. Gutmann, and M. Sipser, "Quantum Computation by Adiabatic Evolution," p. 24, 2000.
- [20] E. Farhi, J. Goldstone, S. Gutmann, J. Lapan, A. Lundgren, and D. Preda, "A quantum adiabatic evolution algorithm applied to random instances of an NP-complete problem," *Science*, vol. 292, no. 5516, pp. 472–475, 2001.
- [21] D. Aharonov, W. Van Dam, J. Kempe, Z. Landau, S. Lloyd, and O. Regev, "Adiabatic quantum computation is equivalent to standard quantum computation," *SIAM review*, vol. 50, no. 4, pp. 755–787, 2008.
- [22] C. C. McGeoch, "Adiabatic quantum computation and quantum annealing: Theory and practice," Synthesis Lectures on Quantum Computing, vol. 5, no. 2, pp. 1–93, 2014.
- [23] C. Nayak, S. H. Simon, A. Stern, M. Freedman, and S. D. Sarma, "Non-abelian anyons and topological quantum computation," *Reviews of Modern Physics*, vol. 80, no. 3, p. 1083, 2008.

- [24] T. Albash and D. A. Lidar, "Adiabatic quantum computation," Reviews of Modern Physics, vol. 90, no. 1, p. 015002, 2018.
- [25] S. Resch and U. R. Karpuzcu, "Quantum computing: an overview across the system stack," arXiv preprint arXiv:1905.07240, 2019.
- [26] J. Preskill, "Quantum computing in the nisq era and beyond," *Quantum*, vol. 2, p. 79, 2018.
- [27] F. Arute, K. Arya, R. Babbush, D. Bacon, J. C. Bardin, R. Barends, R. Biswas, S. Boixo, F. G. S. L. Brandao, D. A. Buell, B. Burkett, Y. Chen, Z. Chen, B. Chiaro, R. Collins, W. Courtney, A. Dunsworth, E. Farhi, B. Foxen, A. Fowler, C. Gidney, M. Giustina, R. Graff, K. Guerin, S. Habegger, M. P. Harrigan, M. J. Hartmann, A. Ho, M. Hoffmann, T. Huang, T. S. Humble, S. V. Isakov, E. Jeffrey, Z. Jiang, D. Kafri, K. Kechedzhi, J. Kelly, P. V. Klimov, S. Knysh, A. Korotkov, F. Kostritsa, D. Landhuis, M. Lindmark, E. Lucero, D. Lyakh, S. Mandrà, J. R. McClean, M. McEwen, A. Megrant, X. Mi, K. Michielsen, M. Mohseni, J. Mutus, O. Naaman, M. Neeley, C. Neill, M. Y. Niu, E. Ostby, A. Petukhov, J. C. Platt, C. Quintana, E. G. Rieffel, P. Roushan, N. C. Rubin, D. Sank, K. J. Satzinger, V. Smelyanskiy, K. J. Sung, M. D. Trevithick, A. Vainsencher, B. Villalonga, T. White, Z. J. Yao, P. Yeh, A. Zalcman, H. Neven, and J. M. Martinis, "Quantum supremacy using a programmable superconducting processor," Nature, vol. 574, no. 7779, pp. 505-510, 2019.
- [28] E. Farhi, J. Goldstone, and S. Gutmann, "A quantum approximate optimization algorithm," arXiv preprint arXiv:1411.4028, 2014.
- [29] J. R. McClean, J. Romero, R. Babbush, and A. Aspuru-Guzik, "The theory of variational hybrid quantum-classical algorithms," *New Journal of Physics*, 2016.
- [30] Y. Alexeev, Quantum Computing Trends, August 2019 (Last accessed: June 2020). https://extremecomputingtraining.anl.gov/files/2019/08/ATPESC_2019_Dinner_Talk_9_8-8_Alexeev-QC_Trends.pdf.
- [31] A. Polkovnikov, K. Sengupta, A. Silva, and M. Vengalattore, "Colloquium: Nonequilibrium dynamics of closed interacting quantum systems," *Reviews of Modern Physics*, vol. 83, no. 3, p. 863, 2011.
- [32] I. Rotter and J. Bird, "A review of progress in the physics of open quantum systems: theory and experiment," *Reports on Progress in Physics*, vol. 78, no. 11, p. 114001, 2015.

- [33] I. M. Georgescu, S. Ashhab, and F. Nori, "Quantum simulation," *Reviews of Modern Physics*, vol. 86, no. 1, p. 153, 2014.
- [34] M. Schreiber, S. S. Hodgman, P. Bordia, H. P. Lüschen, M. H. Fischer, R. Vosk, E. Altman, U. Schneider, and I. Bloch, "Observation of many-body localization of interacting fermions in a quasirandom optical lattice," *Science*, vol. 349, no. 6250, pp. 842–845, 2015.
- [35] J. Smith, A. Lee, P. Richerme, B. Neyenhuis, P. W. Hess, P. Hauke, M. Heyl, D. A. Huse, and C. Monroe, "Many-body localization in a quantum simulator with programmable random disorder," *Nature Physics*, vol. 12, no. 10, p. 907, 2016.
- [36] H. Bernien, S. Schwartz, A. Keesling, H. Levine, A. Omran, H. Pichler, S. Choi, A. S. Zibrov, M. Endres, M. Greiner, et al., "Probing many-body dynamics on a 51-atom quantum simulator," Nature, vol. 551, no. 7682, p. 579, 2017.
- [37] P. Bordia, H. Lüschen, U. Schneider, M. Knap, and I. Bloch, "Periodically driving a many-body localized quantum system," *Nature Physics*, 2017.
- [38] C. Neill, P. Roushan, K. Kechedzhi, S. Boixo, S. V. Isakov, V. Smelyanskiy, A. Megrant, B. Chiaro, A. Dunsworth, K. Arya, et al., "A blueprint for demonstrating quantum supremacy with superconducting qubits," Science, vol. 360, no. 6385, pp. 195–199, 2018.
- [39] M. Kjaergaard, M. E. Schwartz, J. Braumüller, P. Krantz, J. I.-J. Wang, S. Gustavsson, and W. D. Oliver, "Superconducting qubits: Current state of play," *Annual Review of Condensed Matter Physics*, vol. 11, 2019.
- [40] S. Sachdev, Quantum Phase Transitions. Cambridge University Press, 2018.
- [41] A. Lucas, "Ising formulations of many NP problems," Frontiers in Physics, vol. 2, p. 5, 2014.
- [42] M. Born and V. Fock, "Beweis des adiabatensatzes," Zeitschrift für Physik, vol. 51, no. 3-4, pp. 165–180, 1928.
- [43] C. R. Laumann, R. Moessner, A. Scardicchio, and S. L. Sondhi, "Quantum annealing: The fastest route to quantum computation?," *The European Physical Journal Special Topics*, vol. 224, no. 1, pp. 75–88, 2015.
- [44] E. Torrontegui, S. Ibánez, S. Martínez-Garaot, M. Modugno, A. del Campo, D. Guéry-Odelin, A. Ruschhaupt, X. Chen, and J. G. Muga, "Shortcuts to adiabaticity," in

- Advances in atomic, molecular, and optical physics, vol. 62, pp. 117–169, Elsevier, 2013.
- [45] M. Berry, "Transitionless quantum driving," Journal of Physics A: Mathematical and Theoretical, vol. 42, no. 36, p. 365303, 2009.
- [46] E. Crosson, E. Farhi, C. Y.-Y. Lin, H.-H. Lin, and P. Shor, "Different strategies for optimization using the quantum adiabatic algorithm," arXiv preprint arXiv:1401.7320, 2014.
- [47] H. Nishimori and K. Takada, "Exponential enhancement of the efficiency of quantum annealing by non-stoquastic Hamiltonians," Frontiers in ICT, 2017.
- [48] L. Hormozi, E. W. Brown, G. Carleo, and M. Troyer, "Nonstoquastic Hamiltonians and quantum annealing of an Ising spin glass," *Physical Review B*, vol. 95, no. 18, p. 184416, 2017.
- [49] Y. Susa, J. F. Jadebeck, and H. Nishimori, "Relation between quantum fluctuations and the performance enhancement of quantum annealing in a nonstoquastic Hamiltonian," *Physical Review A*, 2017.
- [50] A. B. Özgüler, R. Joynt, and M. G. Vavilov, "Steering random spin systems to speed up the quantum adiabatic algorithm," *Phys. Rev. A*, vol. 98, p. 062311, Dec 2018.
- [51] T. Albash, "Role of nonstoquastic catalysts in quantum adiabatic optimization," *Physical Review A*, 2019.
- [52] G. A. Durkin, "Quantum speedup at zero temperature via coherent catalysis," *Physical Review A*, 2019.
- [53] E. Crosson, T. Albash, I. Hen, and A. Young, "De-signing hamiltonians for quantum adiabatic optimization," arXiv preprint arXiv:2004.07681, 2020.
- [54] I. Ozfidan, C. Deng, A. Smirnov, T. Lanting, R. Harris, L. Swenson, J. Whittaker, F. Altomare, M. Babcock, C. Baron, et al., "Demonstration of a nonstoquastic hamiltonian in coupled superconducting flux qubits," *Physical Review Applied*, vol. 13, no. 3, p. 034037, 2020.
- [55] P. Hauke, H. G. Katzgraber, W. Lechner, H. Nishimori, and W. D. Oliver, "Perspectives of quantum annealing: Methods and implementations," *Reports on Progress in Physics*, 2020.

- [56] K. Schönhammer, "Physics in one dimension: theoretical concepts for quantum many-body systems," *Journal of Physics: Condensed Matter*, vol. 25, p. 014001, dec 2012.
- [57] P. W. Anderson, "Absence of diffusion in certain random lattices," *Phys. Rev.*, vol. 109, pp. 1492–1505, 1958.
- [58] R. Nandkishore and D. A. Huse, "Many-body localization and thermalization in quantum statistical mechanics," *Annu. Rev. Condens. Matter Phys.*, vol. 6, no. 1, pp. 15–38, 2015.
- [59] J. Z. Imbrie, "On many-body localization for quantum spin chains," *Journal of Statistical Physics*, vol. 163, no. 5, pp. 998–1048, 2016.
- [60] S. Choi, N. Y. Yao, S. Gopalakrishnan, and M. D. Lukin, "Quantum control of many-body localized states," arXiv preprint arXiv:1508.06992, 2015.
- [61] N. Y. Yao, C. R. Laumann, and A. Vishwanath, "Many-body localization protected quantum state transfer," arXiv preprint arXiv:1508.06995, 2015.
- [62] S.-J. Gu, "Fidelity approach to quantum phase transitions," *International Journal of Modern Physics B*, vol. 24, no. 23, pp. 4371–4458, 2010.
- [63] L. B. Nguyen, Y.-H. Lin, A. Somoroff, R. Mencia, N. Grabon, and V. E. Manucharyan, "High-coherence fluxonium qubit," *Physical Review X*, vol. 9, no. 4, p. 041041, 2019.
- [64] G. Catelani, "Fluxonium steps up to the plate," Physics, vol. 12, p. 131, 2019.
- [65] S. Backens, A. Shnirman, Y. Makhlin, Y. Gefen, J. E. Mooij, and G. Schön, "Emulating Majorana fermions and their braiding by Ising spin chains," *Physical Review B*, vol. 96, no. 19, p. 195402, 2017.
- [66] R. M. Lutchyn, J. D. Sau, and S. D. Sarma, "Majorana fermions and a topological phase transition in semiconductor-superconductor heterostructures," *Physical review letters*, vol. 105, no. 7, p. 077001, 2010.
- [67] J.-S. Xu, K. Sun, Y.-J. Han, C.-F. Li, J. K. Pachos, and G.-C. Guo, "Simulating the exchange of majorana zero modes with a photonic system," *Nature communications*, vol. 7, no. 1, pp. 1–8, 2016.
- [68] J.-S. Xu, K. Sun, J. K. Pachos, Y.-J. Han, C.-F. Li, and G.-C. Guo, "Experimental simulation of majorana-based quantum computation," arXiv preprint arXiv:1702.08407, 2017.

- [69] Y. Makhlin, G. Schön, and A. Shnirman, "Quantum-state engineering with josephson-junction devices," *Reviews of modern physics*, vol. 73, no. 2, p. 357, 2001.
- [70] A. A. Golubov, M. Y. Kupriyanov, and E. Il'Ichev, "The current-phase relation in josephson junctions," Reviews of modern physics, vol. 76, no. 2, p. 411, 2004.
- [71] A. I. Buzdin, "Proximity effects in superconductor-ferromagnet heterostructures," Reviews of modern physics, vol. 77, no. 3, p. 935, 2005.
- [72] I. Lyuksyutov and V. Pokrovsky, "Ferromagnet-superconductor hybrids," *Advances in Physics*, vol. 54, no. 1, pp. 67–136, 2005.
- [73] R.-P. Riwar, M. Houzet, J. S. Meyer, and Y. V. Nazarov, "Multi-terminal josephson junctions as topological matter," *Nature communications*, vol. 7, p. 11167, 2016.
- [74] A. Fornieri, A. M. Whiticar, F. Setiawan, E. Portolés, A. C. Drachmann, A. Keselman, S. Gronin, C. Thomas, T. Wang, R. Kallaher, et al., "Evidence of topological superconductivity in planar josephson junctions," Nature, vol. 569, no. 7754, p. 89, 2019.
- [75] N. Pankratova, H. Lee, R. Kuzmin, M. Vavilov, K. Wickramasinghe, W. Mayer, J. Yuan, J. Shabani, and V. E. Manucharyan, "The multi-terminal josephson effect," arXiv preprint arXiv:1812.06017, 2018.
- [76] G. V. Graziano, J. S. Lee, M. Pendharkar, C. J. Palmstrøm, and V. S. Pribiag, "Transport studies in a gate-tunable three-terminal josephson junction," *Phys. Rev. B*, vol. 101, p. 054510, Feb 2020.
- [77] Y. V. Nazarov and Y. M. Blanter, Quantum transport: introduction to nanoscience. Cambridge university press, 2009.
- [78] G. Metalidis, Electronic transport in mesoscopic systems. PhD thesis, 2007.
- [79] C. W. J. Beenakker, "Universal limit of critical-current fluctuations in mesoscopic josephson junctions," *Phys. Rev. Lett.*, vol. 67, pp. 3836–3839, Dec 1991.
- [80] A. Altland and M. Zirnbauer, "Field Theory of the Quantum Kicked Rotor.," *Phys. Rev. Lett.*, vol. 77, pp. 4536–4539, Nov. 1996.
- [81] C. W. Groth, M. Wimmer, A. R. Akhmerov, and X. Waintal, "Kwant: a software package for quantum transport," New Journal of Physics, vol. 16, no. 6, p. 063065, 2014.

- [82] P.-G. De Gennes, Superconductivity of metals and alloys. CRC Press, 2018.
- [83] R. Pordes, D. Petravick, B. Kramer, D. Olson, M. Livny, A. Roy, P. Avery, K. Blackburn, T. Wenaus, F. Würthwein, et al., "The open science grid," in *Journal of Physics: Conference Series*, vol. 78, p. 012057, IOP Publishing, 2007.
- [84] I. Sfiligoi, D. C. Bradley, B. Holzman, P. Mhashilkar, S. Padhi, and F. Wurthwein, "The pilot way to grid resources using glideinwms," in 2009 WRI World congress on computer science and information engineering, vol. 2, pp. 428–432, IEEE, 2009.
- [85] J. Johansson, P. Nation, and F. Nori, "Qutip: An open-source python framework for the dynamics of open quantum systems," *Computer Physics Communications*, vol. 183, no. 8, pp. 1760–1772, 2012.
- [86] J. R. Johansson, P. D. Nation, and F. Nori, "Qutip 2: A python framework for the dynamics of open quantum systems," *Computer Physics Communications*, vol. 184, no. 4, pp. 1234–1240, 2013.
- [87] M. Otten, Quantum in C (QuaC), Last accessed: June 2020. https://github.com/ 0tt3r/QuaC.
- [88] Y.-H. Lin, L. B. Nguyen, N. Grabon, J. San Miguel, N. Pankratova, and V. E. Manucharyan, "Demonstration of protection of a superconducting qubit from energy decay," *Physical review letters*, vol. 120, no. 15, p. 150503, 2018.
- [89] A. Kou, W. Smith, U. Vool, R. Brierley, H. Meier, L. Frunzio, S. Girvin, L. Glazman, and M. Devoret, "Fluxonium-based artificial molecule with a tunable magnetic moment," *Physical Review X*, vol. 7, no. 3, p. 031037, 2017.
- [90] "Effects of gate voltage and magnetic field on multi-terminal josephson junctions," In preparation.
- [91] "Anomalous critical current in multi-terminal josephson junctions," In preparation.
- [92] A. B. Özgüler, C. Xu, and M. G. Vavilov, "Response of a quantum disordered spin system to a local periodic drive," *Phys. Rev. B*, vol. 101, p. 024204, Jan 2020.
- [93] P. Coleman, Introduction to many-body physics. Cambridge University Press, 2015.
- [94] A. Pal and D. A. Huse, "Many-body localization phase transition," *Phys. Rev. B*, vol. 82, no. 17, p. 174411, 2010.

- [95] C. Monthus and T. Garel, "Many-body localization transition in a lattice model of interacting fermions: Statistics of renormalized hoppings in configuration space," *Phys. Rev. B*, vol. 81, p. 134202, Apr. 2010.
- [96] A. D. Luca and A. Scardicchio, "Ergodicity breaking in a model showing many-body localization," *EPL* (Europhysics Letters), vol. 101, no. 3, p. 37003, 2013.
- [97] M. Schiulaz, A. Silva, and M. Müller, "Dynamics in many-body localized quantum systems without disorder," *Phys. Rev. B*, vol. 91, p. 184202, May 2015.
- [98] Y. Bar Lev and D. R. Reichman, "Dynamics of many-body localization," Phys. Rev. B, vol. 89, p. 220201(R), Jun 2014.
- [99] D. A. Huse, R. Nandkishore, and V. Oganesyan, "Phenomenology of fully many-body-localized systems," *Phys. Rev. B*, vol. 90, p. 174202, Nov 2014.
- [100] D. A. Abanin and Z. Papić, "Recent progress in many-body localization," *Annalen der Physik*, vol. 529, no. 7, p. 1700169, 2017.
- [101] F. Alet and N. Laflorencie, "Many-body localization: an introduction and selected topics," *Comptes Rendus Physique*, vol. 19, no. 6, pp. 498–525, 2018.
- [102] J. H. Bardarson, F. Pollmann, and J. E. Moore, "Unbounded Growth of Entanglement in Models of Many-Body Localization," *Phys. Rev. Lett.*, vol. 109, p. 017202, July 2012.
- [103] M. Serbyn, Z. Papić, and D. A. Abanin, "Universal slow growth of entanglement in interacting strongly disordered systems," *Phys. Rev. Lett.*, vol. 110, p. 260601, June 2013.
- [104] V. Oganesyan and D. A. Huse, "Localization of interacting fermions at high temper-ature," *Phys. Rev. B*, vol. 75, p. 155111, Apr 2007.
- [105] C. Xu and M. G. Vavilov, "Response to a local quench of a system near the many-body localization transition," *Phys. Rev. B*, vol. 95, p. 085139, Feb 2017.
- [106] M. Serbyn, Z. Papić, and D. A. Abanin, "Local conservation laws and the structure of the many-body localized states," *Phys. Rev. Lett.*, vol. 111, p. 127201, Sep 2013.
- [107] I. H. Kim, A. Chandran, and D. A. Abanin, "Local integrals of motion and the logarithmic lightcone in many-body localized systems," *ArXiv e-prints*, Dec. 2014.

- [108] P. Ponte, Z. Papić, F. Huveneers, and D. A. Abanin, "Many-body localization in periodically driven systems," *Physical review letters*, vol. 114, no. 14, p. 140401, 2015.
- [109] A. Chandran, I. H. Kim, G. Vidal, and D. A. Abanin, "Constructing local integrals of motion in the many-body localized phase," *Phys. Rev. B*, vol. 91, p. 085425, Feb 2015.
- [110] V. Ros, M. Mueller, and A. Scardicchio, "Integrals of motion in the many-body localized phase," *Nuclear Physics B*, vol. 891, no. 0, pp. 420 465, 2015.
- [111] A. Nanduri, H. Kim, and D. A. Huse, "Entanglement spreading in a many-body localized system," *Phys. Rev. B*, vol. 90, p. 064201, Aug 2014.
- [112] M. Serbyn, A. A. Michailidis, D. A. Abanin, and Z. Papić, "Power-law entanglement spectrum in many-body localized phases," *Phys. Rev. Lett.*, vol. 117, p. 160601, Oct 2016.
- [113] O. de Alcantara Bonfim, B. Boechat, and J. Florencio, "Ground-state properties of the one-dimensional transverse Ising model in a longitudinal magnetic field," *Physical Review E*, vol. 99, no. 1, p. 012122, 2019.
- [114] H. Li, Y. Yang, P. Wang, and X. Wang, "Identifying the closeness of eigenstates in quantum many-body systems," *Chinese Physics B*, vol. 26, no. 8, p. 080502, 2017.
- [115] T. Hu, K. Xue, X. Li, Y. Zhang, and H. Ren, "Fidelity of the diagonal ensemble signals the many-body localization transition.," *Physical review. E*, vol. 94, no. 5-1, p. 052119, 2016.
- [116] T. Hu, K. Xue, X. Li, Y. Zhang, and H. Ren, "Excited-state fidelity as a signal for the many-body localization transition in a disordered Ising chain," *Scientific reports*, vol. 7, no. 1, p. 577, 2017.
- [117] C. Monthus, "Many-body-localization transition: sensitivity to twisted boundary conditions," *Journal of Physics A: Mathematical and Theoretical*, vol. 50, no. 9, p. 095002, 2017.
- [118] C. Xu, Topics in Quantum Dynamics of Solid State Qubits. PhD thesis, 2015.
- [119] V. Gritsev and A. Polkovnikov, "Dynamical quantum hall effect in the parameter space," *Proceedings of the National Academy of Sciences*, vol. 109, no. 17, pp. 6457–6462, 2012.

- [120] L. H. Pedersen, N. M. Møller, and K. Mølmer, "Fidelity of quantum operations," *Physics Letters A*, vol. 367, no. 1-2, pp. 47–51, 2007.
- [121] R. Vasseur, S. Parameswaran, and J. Moore, "Quantum revivals and many-body localization," *Physical Review B*, vol. 91, no. 14, p. 140202(R), 2015.
- [122] I. Frérot and T. Roscilde, "Quantum variance: A measure of quantum coherence and quantum correlations for many-body systems," *Physical Review B*, vol. 94, no. 7, p. 075121, 2016.
- [123] E. M. Fortes, I. García-Mata, R. A. Jalabert, and D. A. Wisniacki, "Gauging classical and quantum integrability through out-of-time-ordered correlators," *Phys. Rev. E*, vol. 100, p. 042201, Oct 2019.
- [124] D. J. Luitz, I. M. Khaymovich, and Y. B. Lev, "Multifractality and its role in anomalous transport in the disordered XXZ spin-chain," SciPost Phys. Core, vol. 2, p. 6, 2020.
- [125] A. Lazarides, A. Das, and R. Moessner, "Equilibrium states of generic quantum systems subject to periodic driving," *Physical Review E*, vol. 90, no. 1, p. 012110, 2014.
- [126] A. Lazarides, A. Das, and R. Moessner, "Fate of many-body localization under periodic driving," *Physical review letters*, vol. 115, no. 3, p. 030402, 2015.
- [127] D. V. Else, B. Bauer, and C. Nayak, "Prethermal phases of matter protected by time-translation symmetry," *Physical Review X*, vol. 7, no. 1, p. 011026, 2017.
- [128] N. Y. Yao and C. Nayak, "Time crystals in periodically driven systems," *Physics Today*, vol. 71, pp. 40—47, Sep 2018.
- [129] D. A. Abanin, W. De Roeck, W. W. Ho, and F. Huveneers, "Effective hamiltonians, prethermalization, and slow energy absorption in periodically driven many-body systems," *Physical Review B*, vol. 95, no. 1, p. 014112, 2017.
- [130] D. Abanin, W. De Roeck, W. W. Ho, and F. Huveneers, "A rigorous theory of many-body prethermalization for periodically driven and closed quantum systems," *Communications in Mathematical Physics*, vol. 354, no. 3, pp. 809–827, 2017.
- [131] C. W. von Keyserlingk and S. L. Sondhi, "Phase structure of one-dimensional interacting floquet systems. i. abelian symmetry-protected topological phases," *Physical Review B*, vol. 93, no. 24, p. 245145, 2016.

- [132] A. C. Potter, T. Morimoto, and A. Vishwanath, "Classification of interacting topological floquet phases in one dimension," *Physical Review X*, vol. 6, no. 4, p. 041001, 2016.
- [133] D. V. Else and C. Nayak, "Classification of topological phases in periodically driven interacting systems," *Physical Review B*, vol. 93, no. 20, p. 201103(R), 2016.
- [134] R. Roy and F. Harper, "Abelian floquet symmetry-protected topological phases in one dimension," *Physical Review B*, vol. 94, no. 12, p. 125105, 2016.
- [135] V. Khemani, A. Lazarides, R. Moessner, and S. L. Sondhi, "Phase structure of driven quantum systems," *Physical review letters*, vol. 116, no. 25, p. 250401, 2016.
- [136] C. W. von Keyserlingk, V. Khemani, and S. L. Sondhi, "Absolute stability and spatiotemporal long-range order in floquet systems," *Physical Review B*, vol. 94, no. 8, p. 085112, 2016.
- [137] D. V. Else, B. Bauer, and C. Nayak, "Floquet time crystals," Physical review letters, vol. 117, no. 9, p. 090402, 2016.
- [138] N. Y. Yao, A. C. Potter, I.-D. Potirniche, and A. Vishwanath, "Discrete time crystals: rigidity, criticality, and realizations," *Physical review letters*, vol. 118, no. 3, p. 030401, 2017.
- [139] J. Zhang, P. Hess, A. Kyprianidis, P. Becker, A. Lee, J. Smith, G. Pagano, I.-D. Potirniche, A. C. Potter, A. Vishwanath, et al., "Observation of a discrete time crystal," Nature, vol. 543, no. 7644, p. 217, 2017.
- [140] S. Choi, J. Choi, R. Landig, G. Kucsko, H. Zhou, J. Isoya, F. Jelezko, S. Onoda, H. Sumiya, V. Khemani, et al., "Observation of discrete time-crystalline order in a disordered dipolar many-body system," Nature, vol. 543, no. 7644, p. 221, 2017.
- [141] F. Machado, D. V. Else, G. D. Kahanamoku-Meyer, C. Nayak, and N. Y. Yao, "Long-range prethermal phases of nonequilibrium matter," *Phys. Rev. X*, vol. 10, p. 011043, Feb 2020.
- [142] J. Koch, V. Manucharyan, M. Devoret, and L. Glazman, "Charging effects in the inductively shunted josephson junction," *Physical review letters*, vol. 103, no. 21, p. 217004, 2009.
- [143] U. Vool and M. Devoret, "Introduction to quantum electromagnetic circuits," International Journal of Circuit Theory and Applications, vol. 45, no. 7, pp. 897–934, 2017.

- [144] K. Matveev, A. Larkin, and L. Glazman, "Persistent current in superconducting nanorings," *Physical review letters*, vol. 89, no. 9, p. 096802, 2002.
- [145] H. Meier, R. Brierley, A. Kou, S. Girvin, and L. I. Glazman, "Signatures of quantum phase transitions in the dynamic response of fluxonium qubit chains," *Physical Review B*, vol. 92, no. 6, p. 064516, 2015.
- [146] A. Y. Kitaev, "Unpaired majorana fermions in quantum wires," *Physics-Uspekhi*, vol. 44, no. 10S, p. 131, 2001.
- [147] M. W. Johnson, M. H. Amin, S. Gildert, T. Lanting, F. Hamze, N. Dickson, R. Harris, A. J. Berkley, J. Johansson, P. Bunyk, et al., "Quantum annealing with manufactured spins," *Nature*, vol. 473, no. 7346, p. 194, 2011.
- [148] S. Boixo, T. Albash, F. M. Spedalieri, N. Chancellor, and D. A. Lidar, "Experimental signature of programmable quantum annealing," *Nature communications*, vol. 4, p. 2067, 2013.
- [149] S. Boixo, T. F. Rønnow, S. V. Isakov, Z. Wang, D. Wecker, D. A. Lidar, J. M. Martinis, and M. Troyer, "Evidence for quantum annealing with more than one hundred qubits," *Nature Physics*, vol. 10, no. 3, p. 218, 2014.
- [150] S. Tanaka, R. Tamura, and B. K. Chakrabarti, Quantum spin glasses, annealing and computation. Cambridge University Press, 2017.
- [151] L. D. Landau, "A theory of energy transfer on collisions.," *Phys. Zeitschrift der Sow-jetunion*, vol. 1, p. 88, 1932.
- [152] C. Zener, "Non-Adiabatic Crossing of Energy Levels," Proc. R. Soc. A Math. Phys. Eng. Sci., vol. 137, pp. 696–702, sep 1932.
- [153] E. C. G. Stueckelberg, "Theorie der unelastischen Stösse zwischen Atomen," Helv. Phys. Acta, vol. 5, p. 369, 1933.
- [154] E. Majorana, "Atomi orientati in campo magnetico variabile," *Nuovo Cim.*, vol. 9, pp. 43–50, feb 1932.
- [155] G. Vittorini, D. Hucul, I. V. Inlek, C. Crocker, and C. Monroe, "Entanglement of distinguishable quantum memories," *Phys. Rev. A*, vol. 90, p. 040302, Oct 2014.
- [156] K. M. Maller, M. T. Lichtman, T. Xia, Y. Sun, M. J. Piotrowicz, A. W. Carr, L. Isenhower, and M. Saffman, "Rydberg-blockade controlled-not gate and entanglement in

- a two-dimensional array of neutral-atom qubits," *Phys. Rev. A*, vol. 92, p. 022336, Aug 2015.
- [157] J. M. Chow, J. M. Gambetta, L. Tornberg, J. Koch, L. S. Bishop, A. A. Houck, B. R. Johnson, L. Frunzio, S. M. Girvin, and R. J. Schoelkopf, "Randomized benchmarking and process tomography for gate errors in a solid-state qubit," *Phys. Rev. Lett.*, vol. 102, p. 090502, Mar 2009.
- [158] M. V. Berry, "Quantal phase factors accompanying adiabatic changes," Proceedings of the Royal Society of London. A. Mathematical and Physical Sciences, vol. 392, no. 1802, pp. 45–57, 1984.
- [159] J. E. Avron, M. Fraas, G. M. Graf, and P. Grech, "Landau-Zener Tunneling for Dephasing Lindblad Evolutions," *Commun. Math. Phys.*, vol. 305, pp. 633–639, may 2011.
- [160] J. E. Avron, M. Fraas, G. M. Graf, and O. Kenneth, "Quantum response of dephasing open systems," *New J. Phys.*, vol. 13, p. 053042, may 2011.
- [161] V. Gritsev and A. Polkovnikov, "Dynamical quantum Hall effect in the parameter space.," *Proc. Natl. Acad. Sci. U. S. A.*, vol. 109, pp. 6457–62, apr 2012.
- [162] C. Xu, A. Poudel, and M. G. Vavilov, "Nonadiabatic dynamics of a slowly driven dissipative two-level system," Phys. Rev. A, vol. 89, p. 052102, may 2014.
- [163] M. D. Schroer, M. H. Kolodrubetz, W. F. Kindel, M. Sandberg, J. Gao, M. R. Vissers, D. P. Pappas, A. Polkovnikov, and K. W. Lehnert, "Measuring a Topological Transition in an Artificial Spin- 1/2 System," *Phys. Rev. Lett.*, vol. 113, p. 050402, jul 2014.
- [164] P. Roushan, C. Neill, Y. Chen, M. Kolodrubetz, C. Quintana, N. Leung, M. Fang, R. Barends, B. Campbell, Z. Chen, B. Chiaro, A. Dunsworth, E. Jeffrey, J. Kelly, A. Megrant, J. Mutus, P. J. J. O'Malley, D. Sank, A. Vainsencher, J. Wenner, T. White, A. Polkovnikov, A. N. Cleland, and J. M. Martinis, "Observation of topological transitions in interacting quantum circuits," *Nature*, vol. 515, pp. 241–244, nov 2014.
- [165] W. Vinci and D. A. Lidar, "Non-stoquastic hamiltonians in quantum annealing via geometric phases," *npj Quantum Information*, vol. 3, no. 1, p. 38, 2017.
- [166] A. del Campo, M. M. Rams, and W. H. Zurek, "Assisted Finite-Rate Adiabatic Passage Across a Quantum Critical Point: Exact Solution for the Quantum Ising Model," Phys. Rev. Lett., vol. 109, p. 115703, Sep 2012.

- [167] K. Takahashi, "Transitionless quantum driving for spin systems," *Phys. Rev. E*, vol. 87, p. 062117, Jun 2013.
- [168] A. del Campo, "Shortcuts to adiabaticity by counterdiabatic driving," *Physical review letters*, vol. 111, no. 10, p. 100502, 2013.
- [169] H. Saberi, T. c. v. Opatrný, K. Mølmer, and A. del Campo, "Adiabatic tracking of quantum many-body dynamics," *Phys. Rev. A*, vol. 90, p. 060301, Dec 2014.
- [170] A. Del Campo and W. H. Zurek, "Universality of phase transition dynamics: Topological defects from symmetry breaking," *International Journal of Modern Physics A*, vol. 29, no. 08, p. 1430018, 2014.
- [171] A. del Campo and K. Sengupta, "Controlling quantum critical dynamics of isolated systems," The European Physical Journal Special Topics, vol. 224, no. 1, pp. 189–203, 2015.
- [172] M. M. Rams, M. Mohseni, and A. del Campo, "Inhomogeneous quasi-adiabatic driving of quantum critical dynamics in weakly disordered spin chains," New Journal of Physics, vol. 18, no. 12, p. 123034, 2016.
- [173] K. Takahashi, "Shortcuts to adiabaticity for quantum annealing," *Phys. Rev. A*, vol. 95, p. 012309, Jan 2017.
- [174] D. Sels and A. Polkovnikov, "Minimizing irreversible losses in quantum systems by local counterdiabatic driving," *Proceedings of the National Academy of Sciences*, vol. 114, no. 20, pp. E3909–E3916, 2017.
- [175] M. Demirplak and S. A. Rice, "Adiabatic population transfer with control fields," *The Journal of Physical Chemistry A*, vol. 107, no. 46, pp. 9937–9945, 2003.
- [176] S. Bravyi and M. Hastings, "On complexity of the quantum Ising model," *Communications in Mathematical Physics*, vol. 349, no. 1, pp. 1–45, 2017.
- [177] J. Johansson, P. Nation, and F. Nori, "Qutip 2: A python framework for the dynamics of open quantum systems," *Computer Physics Communications*, vol. 184, no. 4, pp. 1234 1240, 2013.
- [178] H.-Y. Xie and A. Levchenko, "Topological supercurrents interaction and fluctuations in the multiterminal josephson effect," *Phys. Rev. B*, vol. 99, p. 094519, Mar 2019.

- [179] H.-Y. Xie, M. G. Vavilov, and A. Levchenko, "Weyl nodes in andreev spectra of multiterminal josephson junctions: Chern numbers, conductances, and supercurrents," *Phys. Rev. B*, vol. 97, p. 035443, Jan 2018.
- [180] H.-Y. Xie, M. G. Vavilov, and A. Levchenko, "Topological andreev bands in three-terminal josephson junctions," *Phys. Rev. B*, vol. 96, p. 161406, Oct 2017.
- [181] A. E. G. Mikkelsen, P. Kotetes, P. Krogstrup, and K. Flensberg, "Hybridization at superconductor-semiconductor interfaces," *Phys. Rev. X*, vol. 8, p. 031040, Aug 2018.
- [182] B. Van Heck, S. Mi, and A. Akhmerov, "Single fermion manipulation via superconducting phase differences in multiterminal josephson junctions," *Physical Review B*, vol. 90, no. 15, p. 155450, 2014.
- [183] H. Meier, V. I. Fal'ko, and L. I. Glazman, "Edge effects in the magnetic interference pattern of a ballistic sns junction," *Physical Review B*, vol. 93, no. 18, p. 184506, 2016.
- [184] M. Irfan and A. R. Akhmerov, "Geometric focusing of supercurrent in hourglass-shaped ballistic josephson junctions," arXiv preprint arXiv:1810.04588, 2018.
- [185] J. M. Rowell, "Magnetic field dependence of the josephson tunnel current," *Phys. Rev. Lett.*, vol. 11, pp. 200–202, Sep 1963.
- [186] K. S. Wickramasinghe, W. Mayer, J. Yuan, T. Nguyen, L. Jiao, V. Manucharyan, and J. Shabani, "Transport properties of near surface inas two-dimensional heterostructures," Applied Physics Letters, vol. 113, no. 26, p. 262104, 2018.
- [187] W. Mayer, J. Yuan, K. S. Wickramasinghe, T. Nguyen, M. C. Dartiailh, and J. Shabani, "Superconducting proximity effect in epitaxial al-inas heterostructures," Applied Physics Letters, vol. 114, no. 10, p. 103104, 2019.
- [188] R. Skolasinski, Topology, Magnetism, and Spin-Orbit: A Band Structure Study of Semiconducting Nanodevices. PhD thesis, Delft University of Technology, 2018.
- [189] T. Ando, "Quantum point contacts in magnetic fields," *Physical Review B*, vol. 44, no. 15, p. 8017, 1991.
- [190] J. Sauls, "Andreev bound states and their signatures," *Philosophical Transactions* of the Royal Society A: Mathematical, Physical and Engineering Sciences, vol. 376, no. 2125, 2018.

- [191] J. Clarke and A. I. Braginski, *The SQUID handbook*, vol. 1. Wiley Online Library, 2004.
- [192] B. Nijholt, J. Weston, J. Hoofwijk, and A. Akhmerov, "Adaptive: parallel active learning of mathematical functions," 2019.
- [193] K. Dwyer, *Drawing Boundaries in Python*, May 2014 (Last accessed: August 2019). http://blog.thehumangeo.com/2014/05/12/drawing-boundaries-in-python/.
- [194] MATLAB, boundary, 2014 (Last accessed: July 2020). https://www.mathworks.com/help/matlab/ref/boundary.html.
- [195] M. Amin, A. Omelyanchouk, and A. Zagoskin, "Mesoscopic multiterminal josephson structures. i. effects of nonlocal weak coupling," *Low Temperature Physics*, vol. 27, no. 8, pp. 616–623, 2001.
- [196] Periods for kwant.TranslationalSymmetry, August 2019 (Last accessed: June 2020). https://www.mail-archive.com/kwant-discuss@kwant-project.org/msg01987.html.
- [197] M. Istas, C. Groth, A. Akhmerov, M. Wimmer, and X. Waintal, "A general algorithm for computing bound states in infinite tight-binding systems," *SciPost Physics*, vol. 4, no. 5, 2018.
- [198] M. Istas, Quantum scattering beyond quasi one-dimensionnal systems. PhD thesis, Université Grenoble Alpes, 2019.
- [199] V. Ambegaokar and A. Baratoff, "Tunneling between superconductors," *Physical Review Letters*, vol. 10, no. 11, p. 486, 1963.
- [200] T. Laeven, B. Nijholt, M. Wimmer, and A. R. Akhmerov, "Enhanced proximity effect in zigzag-shaped majorana josephson junctions," arXiv preprint arXiv:1903.06168, 2019.
- [201] P. R. Amestoy, I. S. Duff, and J.-Y. L'Excellent, "Mumps multifrontal massively parallel solver version 2.0," 1998.
- [202] A. E. Mikkelsen, P. Kotetes, P. Krogstrup, and K. Flensberg, "Hybridization at superconductor-semiconductor interfaces," *Physical Review X*, vol. 8, no. 3, p. 031040, 2018.

- [203] I. Affleck, "Quantum spin chains and the haldane gap," Journal of Physics: Condensed Matter, vol. 1, no. 19, p. 3047, 1989.
- [204] Y. Tanaka, T. Yokoyama, and N. Nagaosa, "Manipulation of the majorana fermion, andreev reflection, and josephson current on topological insulators," *Physical review letters*, vol. 103, no. 10, p. 107002, 2009.
- [205] A. K. Slimane, P. Reck, G. Fleury, Simulating time dependent thermoelectric transport with the t-Kwant software, November 2018 (Last accessed: July 2020). http://www.cpt.univ-mrs.fr/~crepieux/stock/thermotKwant_ Marseille_nov2018_v2_fleury.pdf.
- [206] B. Rossignol, T. Kloss, and X. Waintal, "Role of quasiparticles in an electric circuit with josephson junctions," *Physical review letters*, vol. 122, no. 20, p. 207702, 2019.